Structure and properties of

drug-loaded polymeric nanoparticles targeting β-amyloid

Von der Fakultät für Physik und Geowissenschaften

der Universität Leipzig

genehmigte

D I S S E R T A T I O N

zur Erlangung des akademischen Grades

Doctor rerum naturalium

Dr. rer. nat.

vorgelegt

von Diplom-Biochemiker Thomas Siegemund

geboren am 03. Oktober 1977 in Ilmenau

Gutachter

Professor Dr. Josef Käs, Universität Leipzig

Professor Dr. Mathias Winterhalter, Jacobs-Universität Bremen

Tag der Verleihung

18. April 2011

When my kids were young I played a game with them.

I'd give each of them a stick. One for each of 'em, and I'd tell them to break it.

They'd do that easy.

Then I'd tell them to make one bundle of all the sticks and try to break that.

A course they couldn't.

I used to say that was family, that bundle.

Alvin Straight

(The Straight Story)

Table of contents

1.   Introduction

The use of nanotechnology in the field of medicine emerged in the late 1970's when first publications described the application of nanoparticles as drug carrier systems. Groups around Jörg Kreuter[1][2][3] and Patrick Couvreur[4][5][6][7] laid the foundation for a rapidly growing field. In these first publications manufacturing, administration, tissue distribution, pharmacokinetics and toxicity of poly(alkylacryl) nanoparticles were investigated. With the turn of the millennium the number of publications[8] started to grow exponentially to a total of about 25,000 in 2009 (fig. 1). This reflects also the widened use in other fields like physics, biology, engineering, and robotics.
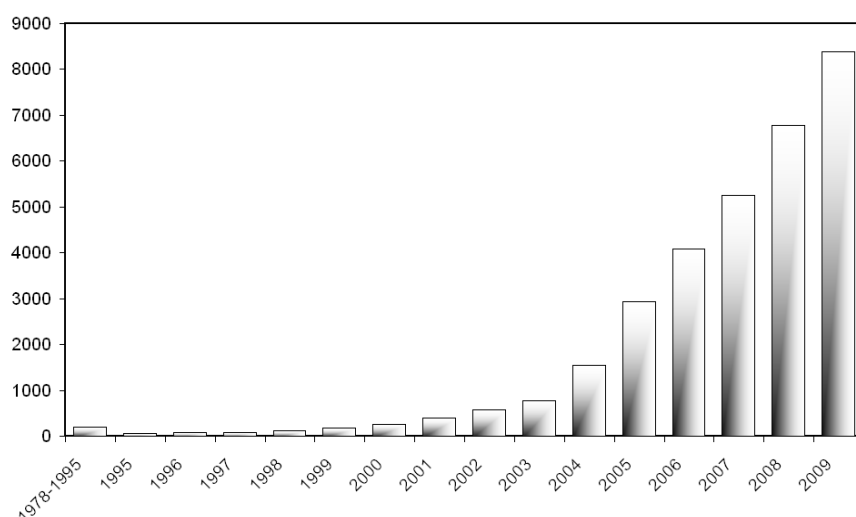
Figure 1: Number of publications (PubMed, search term "nanoparticle")[8]

One of the most prominent properties is the introduction of functionalized surfaces with large area-volume ratios. Hence, the variety of materials, compositions and structures of used nanomaterials increases considerably. What they all have in common is that nanoparticles are used to increase the designated action on a designated site with less effort and less adverse effects[9]. This applies for instance for use of nanoparticles as antitumor drug carriers, where the drug concentration and activity within a tumor are increased while the systemic concentration and, thus, adverse effects are reduced. An other example is the imaging and targeting of vascular smooth muscle cells in stents for detection and therapy of restenosis[10]. Furthermore, nanoparticles enable the use of poorly water soluble compounds which allows the development of a wide range of potent drugs.

1.1. Aim of this work

Polymeric nanoparticles are a promising tool for controlled and targeted drug administration and diagnostics. One of the most challenging goals is to overcome the blood-brain barrier facilitating the treatment of neurological disorders like Alzheimer's disease, Parkinson's disease or brain tumors. Within the last decade animal treatment studies showed superiority of nanoparticle bound drugs over traditional therapies, but also many studies failed.

Less is known about the mechanisms how these particles are distributed with the blood stream, how they penetrate the blood-brain barrier or how they are degraded within the targeted tissue. To enlighten these questions fluorescent polymeric core-shell nanoparticles are used in this work. The targeting of disease-based alterations of brain tissue will be proved by using the fluorescent model drug Thioflavin T in an transgenic mouse model displaying Alzheimer-like pathology. Therefore, the drug is encapsulated within a degradable nanoparticle shell, usually made of poly(butyl cyanoacrylate). The penetration of the blood-brain barrier would be proved by stable nanoparticle cores which remain at the nanoparticle degradation site.

In this work, animal experiments were intended to show the ability of nanoparticles to overcome the blood-brain barrier. Methods and materials should be described, which allow to follow the mechanisms of this process. Furthermore, the experiments were also focused on the elucidation of possible side effects. Besides the brain, other organs of treated animals were analyzed for nanoparticle uptake; the influence of polymeric nanomaterial on blood coagulation was studied.

The *in vivo* behavior of nanoparticles is determined by biochemical and physical properties of the used materials. Particle size may influence the uptake efficiency, surface alterations affect targeting and biocompatibility, whereas degradation determines the drug release. These properties have to be investigated using *in vitro* techniques like absorbance measurements, light or neutron scattering. In addition, the usefulness of physical and biochemical methods for the investigation of polymeric nanoparticle properties had to be tested. *In vitro* methods may be helpful for the better understanding of nanoparticle properties. Furthermore, these techniques may reduce the number of animal experiments which are needed for the development of these seminal drug carriers.

1.2.   Composition and chemical properties of nanoparticles

Nanoparticles might be composed of organic, inorganic or biological materials: methoxy poly(ethylene glycol) / poly(ε-caprolactone), poly(alkyl cyanoacrylate)[11][12], poly(lactic-co-glycolic acid)[13][14], cetyl alcohol/polysorbate[15], hydrogels[16], gold[17][18], magnetic iron oxide[19], solid lipid formulations[20][21], chitosan[22][23], gelatin[24] or albumin[25]. Dendrimers are branched polymeric particles where the drug is polymerized itself[26]. The presented work is focused on nanoparticles based on polymeric materials.

1.2.1. Polymeric nanoparticles

Polymeric nanoparticles are used as preferred carriers for nanomaterial drug delivery. Most of these particles are biodegradable, biocompatible and made of easy available compounds like gelatins[27], chitosan[28], polylactic acid or poly(lactic-co-glycolic acid) copolymer[29], poly(methyl methacrylate), poly(alkyl cyanoacrylate)[30] and poly(butyl cyanoacrylate)[31]. By adding copolymers it is possible to achieve specifically requested properties like surface charges[32] or introducing binding sites for ligands (fig. 2). Furthermore, these copolymers, the applied monomers as well as particle size determine the stability and the release of drugs during degradation. Polymeric nanoparticles exhibit a high potential for surface modifications by adsorption as well as chemical bonding of ligands. Surface modifications determine stability, body distribution, and degradation of nanoparticles[3].
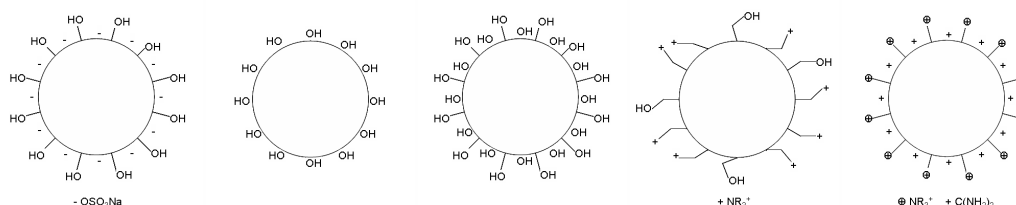
Figure 2: Different surface properties of nanoparticles[32]

There are different ways to assign substances like drugs or dyes to nanoparticles by adsorption, covalent binding or inclusion[33].

1.2.2. Synthesis of spherical polymeric nanoparticles

Polymeric nanoparticles are synthesized by emulsion polymerization[34][35][36][37]. Thereby, the monomer is emulsified in a solution of surfactant and water forming surfactant stabilized droplets of the immiscible monomer in water. An excess of the surfactant leads to micelle formation within the solution, small amounts of monomer diffuse through the water into the micelle. A water-soluble initiator reacts with monomers within micelles or single solved monomers which diffuse to micelles (radical polymerization). The polymerization stops if the monomer runs short or a second radical interferes with the reaction. Due to the reduced concentration of dissolved monomers, monomer molecules from the large droplets pass into the aqueous phase and into the micelles, the polymerization reaction starts over and over by remaining radicals until the amount of unbound monomers is used up. Nanoparticle cores of polystyrene are stabilized against coagulation by the surfactant as well as negatively charged terminal sulfate groups[38] and are routinely purified by ultracentrifugation and dialysis. The resulting dispersion is also called colloidal dispersion or colloid.

The anionic polymerization of alkyl-cyanoacrylates is catalyzed by low concentrations of hydroxide ions (fig. 6). Due to the self-ionization of water the reaction is performed at pH 2[40]. During the polymerization the resulting sparingly soluble poly(butyl cyanoacrylate) (PBCA) is preferentially bound on the surface of the polystyrene core by hydrophobic interactions. The elongation of the polymer backbone is stopped by protons. Particle size is determined by temperature, pH value, monomer concentration and added stabilizers[41]. PBCA is a uncharged polymer with tendency to coagulation, which can be avoided by the use of amphiphilic block copolymers like Poloxamer 188[42], composed of a hydrophobic chain of poly(propylene oxide) flanked by two hydrophilic chains of poly(ethylene oxide). The core-shell nanoparticles are purified by ultracentrifugation and dialysis.
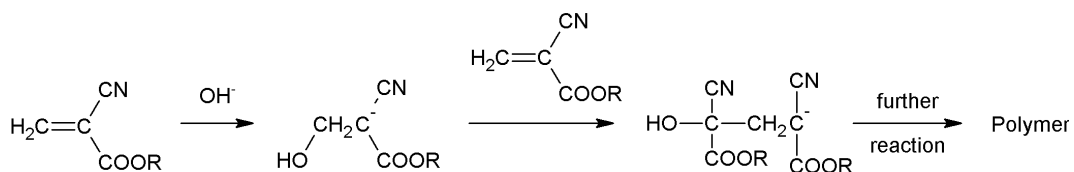
Figure 3: Radical polymerization for synthesis of poly(alkyl cyanoacrylates)[39]

After adding Thioflavin T or thioflavin S as model drugs to the reaction solution, these compounds were embedded within the polymeric spheres or absorbed to the surface. This principle was also shown for loperamide[43] or doxorubicin[44]. The dye rhodamine B was covalently bound to epoxypropylmethacrylate and added as a reactant to polymerization of styrene to achieve intense red fluorescent particle cores.

The synthesis of nanoparticles consisting of epoxypropylmethacrylate, methacrylic acid or hydroxyethylmethacrylate was carried out as a radical polymerization initiated by potassium peroxidisulfate.

1.2.3. Chemical degradation

Polystyrene is resistant against aliphatic alcohols and alkalies. Furthermore, it is slightly affected by strong as well as weak acids. Polystyrene is unstable against organic and/or non-polar solvents (aldehydes, esters, ethers, ketones, aliphatic and aromatic hydrocarbons) and oxidizing agents. Poly(alkyl cyanoacrylates) degrade slowly by a reversed KNOEVENAGEL reaction in the presence of distilled water; released substances are toxic formaldehyde and irritant cyanoacetic acid (fig.4). The reaction is catalyzed by hydroxide ions, the reaction rate depends on the pH of the solvent and the chain length of the side chain[39] as well as specific surface, particle size and polymer molecular weight[45]. While poly(methyl cyanoacrylate) releases large amounts, poly(butyl cyanoacrylate) delivers significantly less toxins. Furthermore, poly(octyl cyanoacrylate) nanoparticles, but not poly(octyl cyanoacrylate-co-butyl cyanoacrylate) nanoparticles show lower formaldehyde-mediated cytotoxicity then poly(butyl cyanoacrylate) nanoparticles[46]. On the other hand, some of the released formaldehyde may be neutralized by binding to the C-H-acidic end of the polymer chain[47].
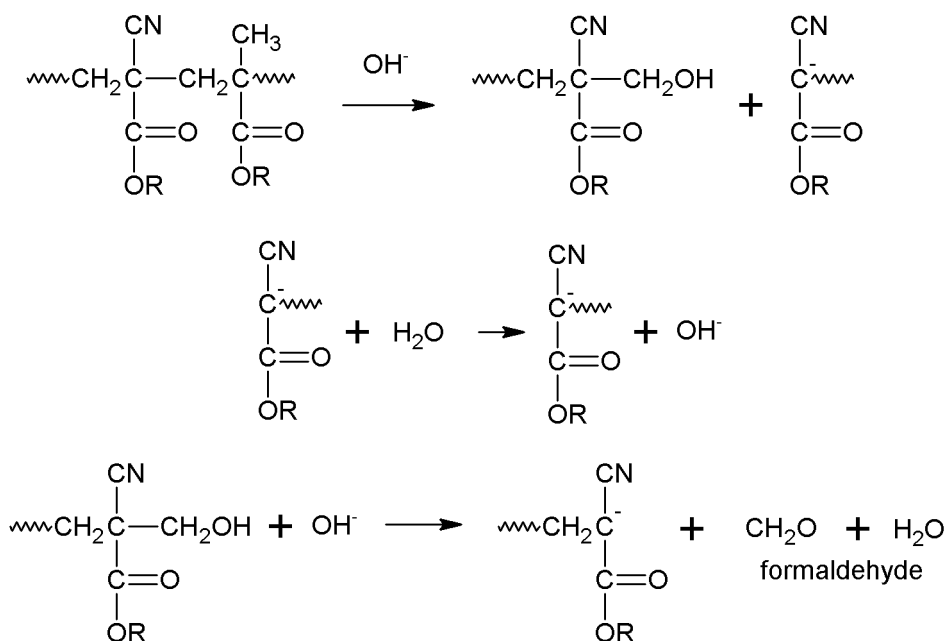
Figure 4: Hydroxide-catalyzed degradation of poly(alkyl cyanoacrylates)[39]

A second degradation reaction is the hydroxide-mediated ester hydrolysis of the side chain resulting in the release of n-butanol[48]. This reaction is strongly favored by esterase-mediated enzymatic degradation. Poly(alkyl cyanoacrylates) (PACA) are stable against organic and non-polar solvents as well as acids. The resistance to acids allows a oral application of PACA nanoparticles whereas in the basic environment of the intestine the nanoparticles are degraded resulting in the release of the drug.

Nanoparticles which consist of poly(methyl methacrylate) are stable against acids, basics, gasoline and oil, but sensitive against alcohols, acetone and benzene which form cracks.

1.3. Biochemical properties of nanoparticles

Nanoparticles, entering the blood stream, encounter a complex environment of plasma proteins and immune cells. Monocytes, platelets, leukocytes and dendritic cells may incorporate nanomaterials, as well as resident phagocytes, like Kupffer cells in liver, dendritic cells in lymph nodes and macrophages and B cells in spleen. This uptake occurs through different pathways and is accompanied by the adsorption

6

of plasma proteins (opsonization)[49]. These processes influence the distribution of the nanoparticles in the body as well as the release of the bound drugs and, hence, unwanted and unexpected adverse effects may occur (see chapter 1.4.5).

One of the commonly used surface modifications is coating or covalent linking of biologically inert poly(ethylene glycol) onto the nanoparticle surface[50][51] which leads to reduced protein binding[52], cell adhesion[53], immunogenicity and limited phagocytosis by the reticuloendothelial system[54]. Furthermore, it is easy to introduce biological markers to determine cell or organ specificity. For instance, for targeting of the blood-brain barrier of nanoparticles are coated with apolipoprotein E[55] which leads to receptor-mediated endocytosis[56] through the blood-brain barrier mimicking the uptake of low density lipoprotein[57].

1.3.1. Enzymatic degradation

Polystyrene nanoparticles are not biodegradable[58]. Similarly, particles consisting of poly(methyl methacrylate) are stable and remain undegraded for months after subcutaneous application[59].

PBCA nanoparticles are biodegradable due to the enzyme-catalyzed cleavage of the butyl side chain (fig. 5). This process is catalyzed by unspecific esterases and results in the release of a water soluble poly(cyano carbonic acid)[60]. The enzymatic degradation is also shown by tissue homogenates of various tissues[61] or liver microsomes[48]. The biodegradation of poly(butyl cyanoacrylate) nanoparticles depends on pH, ionic strength, temperature, surface modifications, particle and enzyme concentrations[61][62] and can be monitored using photometry (see chapter 1.5.2.1.). Furthermore, the reaction rate is controlled by the length of the alkyl side chain[63][64].
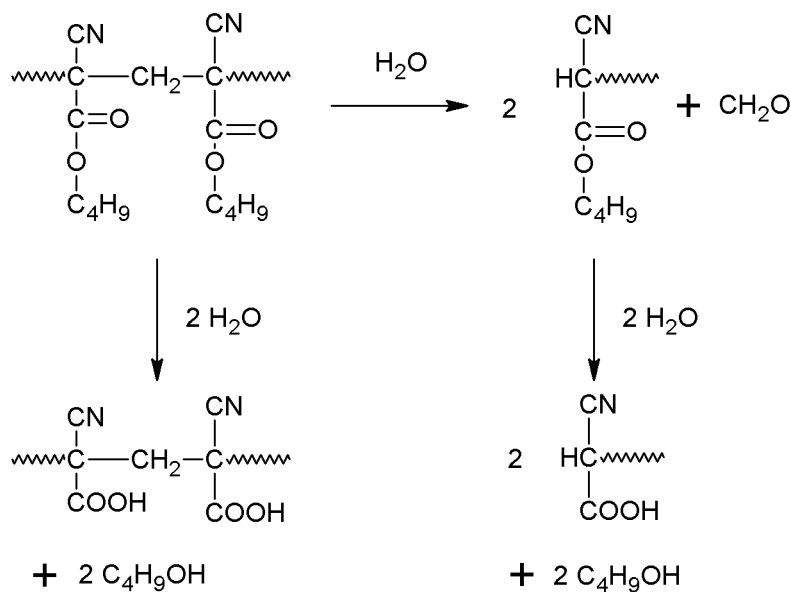
Figure 5: Degradation of poly(butyl cyanoacrylate)[48]

1.3.2. Release of drugs

The release of drugs primarily depends on the kind of interaction between nanoparticles and drugs. A substance adsorbed at the particle surface pass into the environment depending from its solubility. Due to the large contact area between particle and surrounding solvent a burst release of the drug occurs. This type of drug delivery may be helpful in topical application[65] or in case of unstable or hardly soluble drugs[11][66].

If the drug is embedded within the polymer without covalent binding, it is released by desorption during the degradation of the nanoparticle. Beside the aforementioned applications these nanoparticles can be used for the targeting of organs or tissues, for a considerable longer release durability in chronic diseases or vaccination[67].

In some cases the drug is bound covalently to the polymer. This may occur if the polymerization affects the drug or *vice versa*. Furthermore, it might be a method to improve the drug concentration in the particle. After application *in vivo* the drug is released by unspecific reactions, typically enzyme-catalyzed hydrolysis.

In the cases of embedded or covalently bound drugs, the kinetic of the drug release can be determined by nanoparticle composition[64].

1.4. The use of drug-loaded nanoparticles in medicine

At the beginning of year 2006 about 130 nano-based drugs and delivery systems had entered preclinical, clinical or commercial development[68]. To improve therapeutic options there is a need to deliver therapeutic agents in such a way that most drug molecules will selectively reach the desired targets at optimal drug concentrations and with minimal collateral damage[69]. Drug-loaded nanoparticles are promising tools to achieve increased target selectivity and, therefore, reduce side effects.

One of the major fields in nanomedicine is the delivery of chemotherapeutic agents to cancer cells[70][71]. These drugs are known for a wide variety of strong adverse effects and there is a need for further improvements. Affected cancer cells express disease-specific molecules like receptors, proteases and adhesion molecules[69]. These molecules are different from their unaffected counterparts and, therefore, a unique target. Nanoparticles expressing specific antibodies or adhesion molecules are able to bind such targets and release the embedded drug close to it. A wide variety of cancer types are another challenge for the development of therapeutic agents.

Table 1: Nanoparticle classes, materials and applications in the field of medicine[72]

Particle class	Materials	Applications
Natural materials or derivatives	Chitosan Dextrane Gelatine Alginates Liposomes Starch	Drug / gene delivery
Dendrimers	Branched polymers	Drug delivery
Fullerenes	Carbon based carriers	Photodynamics Drug delivery
Polymeric carriers	Polylactic acid Poly(cyano)acrylates Polyethylenimine Block copolymers Polycaprolactone	Drug / gene delivery
Ferrofluids	(Ultrasmall) superparamagnetic iron oxide nanoparticles	Imaging (Magnetic resonance imaging)
Quantum dots	Cd/Zn-selenides	Imaging In vitro diagnostics
Various	Silica-nanoparticles Mixtures of above	Gene delivery

An other promising field is the application of nanoparticles in gene therapy[73]. The use of free DNA is hindered by nuclease degradation, whereas DNA membrane

permeation for cellular uptake is excluded due to its size and negative charge. Fundamental problems associated with high effective viral vector systems open a field for non-viral carriers with lower efficacy but superior usability[74]. Attractive targets are epithelial surfaces of lung, gastrointestinal tract, blood vessels, muscles and skin[75]. In addition, tumor cells are possible targets[76].

Furthermore, nanoparticles enable oral[77], nasal[76] and topical application[78] as well as ocular drug delivery[79]. Due to their prolonged stability nanoparticles are a promising carrier for vaccines[80] or adjuvants[81].

Besides the therapeutic use, nanoparticles serve as tools for clinical diagnostics[82][83] and for basic research[84].

1.4.1. The blood-brain barrier

The first description of blood-brain barrier effects was given by Paul Ehrlich in 1885 who observed that after injection of water soluble acidic dyes all organs of the experimental animal were colored except the brain and the spinal cord. Since some dyes like Methylene blue[86][87] stain brain tissues he misinterpreted his findings as reduced affinity. One of Ehrlich's students, Edwin Goldmann, injected the dye directly into the spinal fluid of brain and found the brain dyed but not the rest of the body. In 1921 Lina Stern proposed the concept of the blood-brain barrier (then termed hemato-encephalic barrier) but it was not until the 1960's, when the newly introduced scanning electron microscope helped to proof this concept.

In the brain more then 100 billion capillaries form a very dense network with a total length of about 600 km and an estimated surface area of 12–20 m^2. The blood-brain barrier regulates brain uptake and release of substances[88].
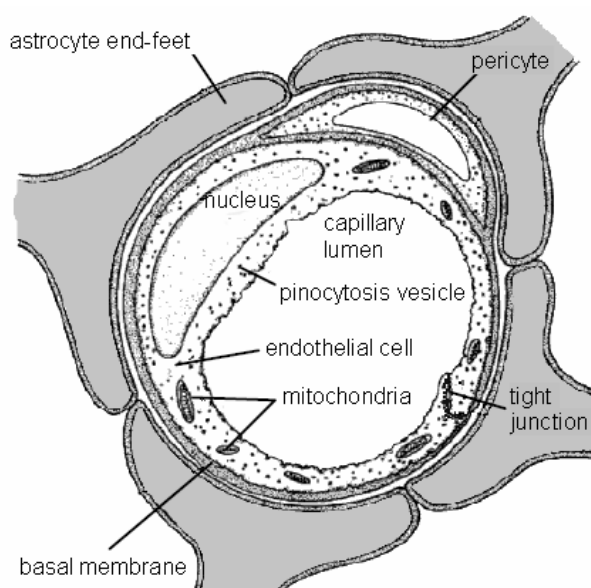
Figure 6: Cross section of the blood-brain barrier[85]

1.4.1.1. Endothelial cells

In contrast to peripheral blood vessels, endothelial cells of the central nervous system form a tight vessel wall which restricts diffusion of microscopic objects and larger hydrophilic molecules[85]. This barrier is closed by a dense network of tight junctions (fig. 6/7) which link neighboring endothelial cells and prevent passive influx of most substances except very small, lipophilic molecules[90]. The blood-brain barrier exhibits a high permeability for water[91], mediated through aquaporins[92]. Compared to peripheral endothelium pinocytosis, a process of unspecific uptake of solved substances, is significantly diminished in the blood-brain barrier[93]. On the other hand, facilitated diffusion, which allows concentration gradient driven specific transport for molecules like glucose, amino acids or short monocarboxylic acids, is a prominent uptake mechanism[94]. The brain, comprising only about 2% of the whole body tissue requires about 20% of the whole energy[95]. Therefore, the cells of the endothelium contain about 5 times more mitochondria then peripheral endothelial cells[96]. A significant part of the energy is used for active receptor-mediated uptake of molecules as well as receptor-mediated transcytosis. The former controls the influx of required molecules like hormones and the efflux of hormones or degradation products, some of them are stereoselective transporters[97]. Among the highly important efflux receptors is the group of multi-drug resistance proteins, enabling endothelial cells to remove potent threatening substances and so most drugs too[98].
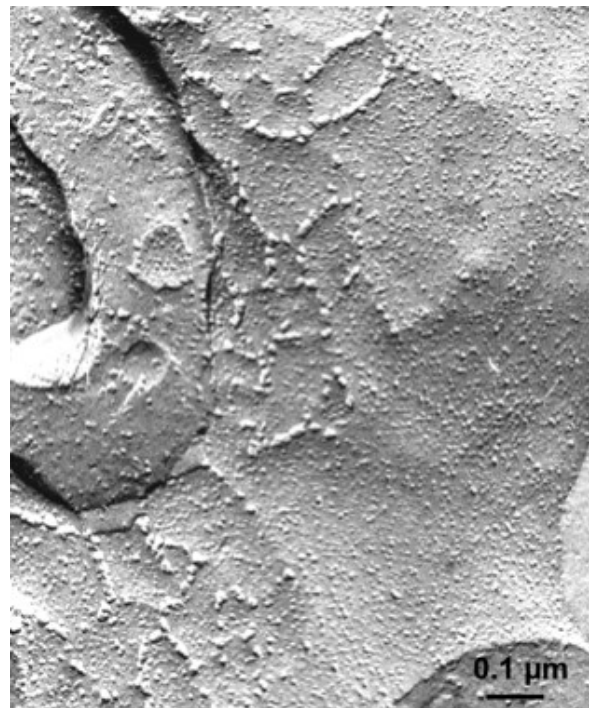
Figure 7: Tight junctions of the blood-brain barrier (Freeze fracture morphology from rat)[89]

Besides physical barriers, drug-metabolizing enzymes at the blood-endothelium interface provide an additional enzymatic barrier. These include the cytochrome P450 hemoproteins, several cytochrome P450-dependent monooxygenases, NADPH-cytochrome P450 reductases, UDP-glucuronosyltransferases, alkaline phosphatases, glutathione peroxidases, and epoxide hydrolases[99][100][101][102].

1.4.1.2. Basal lamina, astrocytes, pericytes

The basal lamina is an about 45 nm thin layer of extracellular matrix, surrounding epithelial cells. Their components are produced by the cells itself and are mainly of collagen type IV, heparan sulfate proteoglycans, laminin and other extracellular matrix proteins[93].

Figure 8: Basal lamina[103]

Astrocytes are frequently star-shaped macroglial cells. They play an important role in the development, maintenance and repair of brain tissue and signaling[104][105]. The endothelial cells of the blood-brain barrier are encircled by astrocyte end-feet. Contrary to the former opinion, they are not a part of the blood-brain barrier but it has been shown that astrocytes induce the formation of the tightened endothelial cell network[106][107].

About 20% from the outer endothelium of the cerebral capillaries are covered with pericytes which fulfill three functions within the blood-brain barrier: contractility, regulation of the endothelial cell activity and macrophage activity[108].

1.4.1.3. Crossing the blood-brain barrier

Crossing the blood-brain barrier is one of the most important topics in the development of drugs targeting the brain[109]. Nanoparticles, liposomes and other polymeric colloids are considered as effective carriers for drugs to be transported into the brain[110][111][112]. Positive results were achieved with doxorubicin-containing nanoparticles which diminished glioblastomas with higher efficiency than free drugs[113]. Such cancer therapies predominantly based on drug-loaded PBCA nanoparticles[9] which were shown to undergo enzymatic biodegradation both *in vitro*[63] and *in vivo*[114][115]. Core-shell nanoparticles provide further advances as they are composed of a hardly degradable PS core and a PBCA shell allowing a 'burst release' of encapsulated drugs[116]. Furthermore, nanoparticles coated with polysorbate 80 and apolipoprotein E displayed an improved brain targeting[117][12].

Mechanisms of nanoparticle uptake by the blood-brain barrier is not enlightened until today. The presumably most promising approach is based on the increased transport after surface modification with apolipoprotein E[118] or an ApoE dipeptide which was

found to bound with high affinity to the receptor[119]. ApoE is found in chylomicrons, large lipoprotein particles, and regulates the uptake into cells through specific recognition by low density lipoprotein (LDL) receptors[120]. LDL receptors have been detected in the brain[121][122] and even more prominent in the liver which is responsible for LDL catabolism. Nevertheless, until now there is no proof, that intact polymeric nanoparticles - also if coated with polysorbate 80 and apolipoprotein E - crossed an intact blood-brain barrier. It is suspected, that the particles or their (toxic) degradation products may cross the blood-brain barrier after its disruption[123][124]. One goal of this work was an approach to demonstrate the uptake of nanoparticles into the brain *in vivo* and directly (see chapter 1.5.7.). The study was performed using transgenic mice, which express mutated human amyloid β (Aβ). Degeneration products of this protein aggregate to insoluble amyloid plaques, a major hallmark of Alzheimer's disease. These aggregates are a promising target for drugs as well as a useful readout for successful blood-brain barrier penetration. Nanoparticles were administered intravenously, intracerebroventricularly and intrahippocampally to observe nanoparticle distribution within the body, targeting of the blood-brain barrier as well as of amyloid β.

1.4.2. Alzheimer's Disease

Alzheimer's disease (AD) is the most common neurodegenerative disorder of an aging society. Major symptoms are progressive memory impairment, disordered cognitive function, altered behavior, delusions, and loss of social appropriateness and a progressive decline in language function[125]. There are two different forms of the disease, the "juvenile" form with an onset before the age of 65 and a "senile" form, which occurs in patients above this age. The first one is often associated with defined genetic mutations whereas the latter seems to be multi-causal. Currently, the diagnosis of Alzheimer's disease can only made by *post mortem* examination of its major histopathological hallmarks which are are neurofibrillary tangles[126] and amyloid plaques[127]. Furthermore, Alzheimer's disease is associated with loss of synapses[128] and neurons[129] and cholinergic depletion[130] but there is still no unitary theory that can account for all the clinical and neuropathological features[131].

Moreover, it is not clear whether neurofibrillary tangles acting neuroprotective and/or pathogenic and whether amyloid plaques are cause or result of the disease.

Intracellular neurofibrillary tangles (NFT) are formed of insoluble hyperphosphorylated protein tau. The age-dependent tau hyperphosphorylation can be found in most individuals above an age of 60 and is strongly increased in patients with AD[132]. In early stages, the pathology emerges in the low limbic system, such as entorhinal cortex, hippocampus and the nucleus basalis of Meynert. Later on it expands to the high limbic system and finally tau pathology is affecting the neocortex[131].

In its less phosphorylated form tau stabilizes the microtubules of axonal cytoskeleton[133]. The loss of its normal function leads to a breakdown of the axonal transport which results in a loss of synaptic function of the affected neuron. The cause for the hyperphosphorylation of tau is still unknown, but a regulated imbalance of phosphorylation and dephosphorylation was observed in hibernating animals[134].

Amyloid plaques contain insoluble fibrils of amyloid β and accumulate in the extracellular space. Besides various Aβ peptides these very inhomogeneous aggregates contain different substances like apolipoprotein E (ApoE) or heparan sulfate proteoglycans. Aβ results from the cleavage of the amyloid precursor protein (APP) by the enzymes γ-secretase and β-secretase, also known as β-amyloid cleaving enzyme[135]. Mutated presenilin subunit of γ-secretase and APP mutations cause an abnormal production of amyloid β with a length of 42 or 43 amino acids ($A\beta_{42}$ or $A\beta_{43}$). These proteins tend to aggregation due to their high hydrophobicity[125], mutations in ApoE lead to a protein which can promote Aβ aggregation[136]. Furthermore, amyloid plaques vary in their predominant vascular or parenchymal localization.

The role of Aβ plaques in the progression of AD was contested within the last years. A clinical study with vaccination against Aβ showed no benefits for the treated patients despite a significant reduction of amyloid load in patients[137] in contrast to studies in animals[138][139]. Recently, it was shown that the inhibition of γ-secretase and, therefore, amyloid secretion, worsened the disease in a phase III study[140]. However, in this study a significant reduction of amyloid plaques was observed.

1.4.3. Thioflavin T and thioflavin S as model drugs for targeting of β-amyloid through the blood-brain barrier

Fibrillar Aβ is bound by several dyes such as thioflavins which allow histochemical detection of pathological aggregated Aβ. Thioflavin T (also Basic Yellow 1, IUPAC: 4-(3,6-dimethyl-1,3-benzothiazol-3-ium-2-yl)-N,N-dimethylaniline chloride) is obtained by the methylation of dehydrothiotoluidine with methanol in the presence of hydrochloric acid. In aqueous solution, thioflavin T exhibits only low fluorescence intensity (excitation 350 nm, emission 440 nm) and forms micelles above 4µM[141].

Thioflavin T binds to β-sheet structures of amyloid oligomers. Three different binding sites have been revealed, two within the grooves on β-sheet surface and one at the end of the β-sheet[142]. While binding to
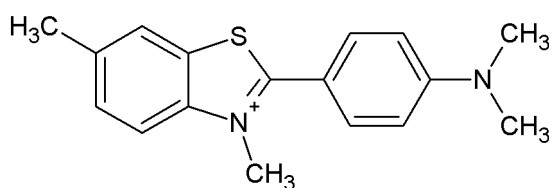
Figure 9: Chemical structure of Thioflavin T

aggregated β-amyloid, thioflavin T undergoes a significant red shift in its emission spectrum (excitation 440 nm, emission 490 nm). Additionally, the intensity increases several orders of magnitudes[141][143]. After intravenous injection thioflavin T shows weakly labeled vascular amyloid deposits but it is not able to pass the blood-brain barrier to label parenchymal amyloid[144]. Therefore, only if bound to a carrier, thioflavin T will be able to penetrate the blood-brain barrier and to target β-amyloid.

Thioflavin S is used as a dye to visualize β-amyloid containing plaques. It is a mixture of as many as six compounds that results from the methylation of dehydrothiotoluidine. Thioflavin S also binds to amyloid fibrils[145][146] and gives a spectral shift upon binding. Due to its high background fluorescence it appears not suitable for the quantification of fibril solutions.
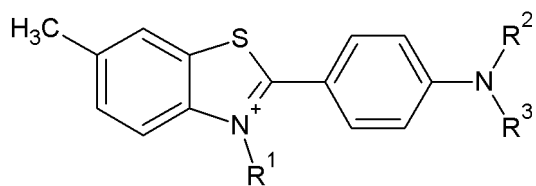
Figure 10: Thioflavin S $\left(R^{1-3} = H \,\text{or}\, CH_3 \right)$

The uncharged 4-(6-methyl-1,3-benzothiazol-3-ium-2-yl)-N,N-dimethylaniline (BTA-2) is a hardly water soluble derivative of thioflavin T. Due to its lipophilic properties BTA-2 is able to cross the blood-brain barrier and then targeting fibrillar β-amyloid[146].

1.4.4. Animal models

Until now there is no suitable general animal model for Alzheimer's disease. On the one hand, classical laboratory animals, like mice or rats, only express an amyloid precursor protein variant, which is degraded to exclusively non-aggregating β-amyloid peptides not forming any plaque[147]. On the other hand, there are several animal species which develop plaques in higher age, e.g. rhesus monkey, baboon, guanaco, reindeer or bison[148], but these animals are not suited for animal experiments also due to late onset of the phenotype. The most promising option is the use of transgenic animals; the expression of human amyloid precursor protein in species like mice allows to study amyloidogenesis in numerous animals within a defined time frame[149][150].

In the presented work two slightly different strains of animals were investigated. The APPswe/PS1(A246E)[151] double transgenic mice and the APPswe/PS1dE9[152] double transgenic mice express amyloid precursor protein as well as presenilin-1 variants which lead to an accelerated Aβ deposition in brain. These mice show typical signs of progressive memory impairment dependent on the amount of insoluble (aggregated) $A\beta_{42}$ within the hippocampus[153].

1.4.5. Biological response and adverse effects

The wide variety of materials and applications of nanoparticles correlates with a wide variety of possible adverse effects. Different compounds of the nanoparticles as well as their degradation products may be toxic or may accumulate within the body, organs or cells. These effects will be also influenced by the way of nanoparticle administration (see fig. 11)[154]. Nanoparticles display a large surface which allow interaction with blood or tissues. The most prominent protection systems, immune response and coagulation system, are influenced by xeno-materials and surfaces.
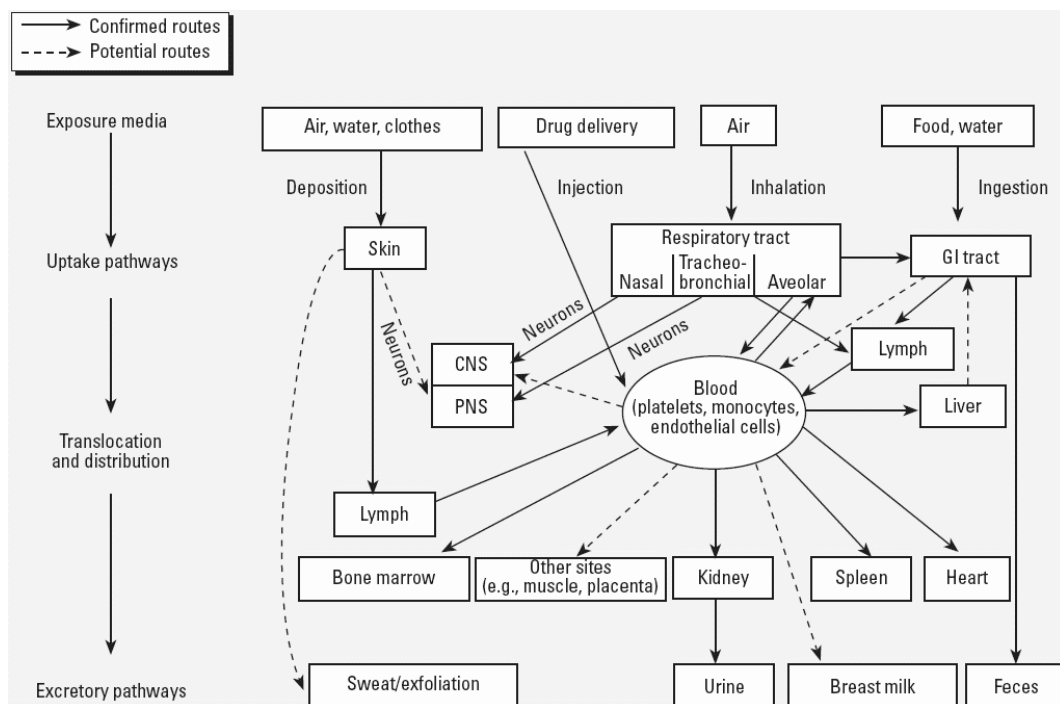
Figure 11: Uptake, distribution and excretion of nanoparticles[154] (CNS – central nervous system, PNS – peripheral nervous system, GI gastrointestinal)

1.4.5.1.   Toxicity

Several studies regarding nanoparticles and toxicity are focused on the action of unintentional nanomaterial uptake, mainly through the respiratory system. This includes air pollution from combustion products, fumes and particulate matter which are known to cause diseases of the respiratory tract including inflammation and cancer[154]. Such diseases might be initiated by the uncontrolled nanomaterial uptake in phagocytes which cause activation of the immune system and alterations of cells, proteins and genetic material induced by free radicals[155]. Furthermore, air pollution is an important reason for cardiovascular diseases[156]. The rapid increase of nanomaterial application may also lead to an enhanced percutaneous or peroral uptake. This leads to irritation, inflammation and alterations of the gastrointestinal tract and the skin.

On the other hand, nanoparticles are useful as carriers for toxic substances like chemotherapeutic agents in cancer therapy. The bound agent shows lower side effects and higher efficiency in therapy[70][25][44][157]. However, the the lower toxicity of the bound agent may cover toxicity which is introduced by using nanoparticles[72].

Furthermore, these studies were not designed to reveal side effects induced by nanoparticles. The toxicity of nanoparticles is induced by the particle itself but also by particle degradation products[158]. The degradation of PBCA nanoparticles used in this work releases n-butanol, which is known to alter cell membrane permeability[159], and the poly (cyanoacrylate) backbone, which binds cations and may penetrate membranes[30].

1.4.5.2. Binding of proteins

After *in vivo* application several proteins bind to polymeric nanoparticles by adsorption. Mainly albumin, fibrinogen, immunoglobulin G and apolipoproteins are bound to the particle surface; an overview is given in table 2. The binding of protein depends on their surface charge[160][161], hydrophobicity, size and shape[162]. Albumin and fibrinogen may bind earlier due to their high abundance in blood, whereas immunoglobulins and apolipoproteins may replace them due to their higher affinity[163]. All these proteins are important for distribution and clearance of nanoparticles *in vivo*[164][160].

1.4.5.3. Initiation of the adaptive immune response

Antigens are molecules that induce immune response and their contact with cells of the immune system initiates a defense reaction. This immune response leads to the production of specific antibodies directed against the antigen and the generation of regulatory T helper cells or cytotoxic T lymphocytes. Antigens are processed and presented in association with major histocompatibility complex (MHC) class I or II glycoproteins on the cell surface of antigen-presenting cells. This peptide:MHC-complex can be recognized by T lymphocytes and activates T cells. Polysaccharides, glycolipids, nucleic acids and synthetic antigens may activate B cells[165].

For its immunogenicity a substance requires a certain degree of heterogeneity. Polymers formed from a single repetitive monomer are unlikely to induce an immune response. This applies also for the use of poly(ethylene glycol) for the masking of nanoparticles, which opens a wide field for more heterogeneous particles[166][49][160].

On the other hand, this gives polymeric nanoparticles properties of a hapten carrier. Binding a molecule to the nanoparticle surface may induce immunogenicity against

this molecule[167] which can be helpful if the nanoparticle is used as an adjuvant in vaccination, but could also induce unwanted immunologic reactions.

Table 2: Protein binding of various nanoparticles

nanoparticles / material	adsorbed proteins	see
polystyrene with Poloxamer 184, 188, 407	albumin, fibrinogen, IgG, apolipoproteins, factor B, transferrin	[168]
polystyrene with rhodamine B	albumin, IgG, fibrinogen, apolipoproteins	[58]
poly(cyanoacrylate) nanoparticles	albumin, IgG, IgM, fibrinogen, apolipoproteins	[169]
poly(butyl cyanoacrylate) with tween 80	albumin, IgG, fibrinogen, IgM, apolipoproteins	[170]
poly(butyl cyanoacrylate) with dextran	albumin, IgG, fibrinogen, apolipoproteins, serotransferrins, transthyretins	[171]
poly(hexadecyl cyanoacrylate)	albumin, apolipoproteins, IgG, transferrin	[172] [173]
various polymers/copolymers	albumin, IgG, fibrinogen, apolipoproteins	[174]
various polymers/copolymers	albumin, IgG, fibrinogen, IgM, apolipoproteins	[175]
poly(ε-caprolactone)	IgG, apolipoproteins	[176]
poly(lactic acid) nanoparticles with PEG	albumin, fibrinogen, apolipoproteins, IgG	[177]
poly(D,L-lactic acid) nanoparticles	albumin, IgG, fibrinogen, IgM, apolipoproteins, antithrombin III	[178]
liposomes	albumin, fibrinogen, apolipoproteins, IgG, α-antitrypsin, α2-macroglobulin, IgM	[179]
solid lipid nanoparticles with tween 80	fibrinogen, IgG, IgM, transthyretin, apolipoproteins (including apoE)	[180]
solid lipid nanoparticles with Poloxamer 188	albumin, fibrinogen, IgG, IgM, transthyretin, apolipoproteins (excluding apoE)	[180]
solid lipid nanoparticles with Poloxamer or poloxamins	albumin, fibrinogen, apolipoproteins	[181]
single-walled carbon nanotubes	albumin	[182]
single- and double-walled carbon nanotubes	albumin, fibrinogen, apolipoproteins, complement factor C1q	[183]
iron oxide nanoparticles	albumin, IgG, IgM, fibrinogen, complement factor C3b	[184]

1.4.5.4.   Initiation of the innate immune system - Opsonization and phagocytosis

Opsonization is a process when xeno-materials are covered by molecules such as immunoglobulins and factors of the complement system (see table 2). Opsonized surfaces are recognized by phagocytic cells. There are two different ways how

phagocytic cells recognize and attach to their target: recognition of opsonins via specific receptors or non-specific adherence to surfaced absorbed plasma proteins[164]. By phagocytosis, which means uptake of the foreign materials by the cell, nanoparticles are removed from the bloodstream.

The phagocytosis of polymeric nanoparticles by resident or elicited macrophages induce oxidative burst and the release of toxic factors, which affect the viability of the macrophages[185]. If the polymeric nanoparticles are not biodegradable, they accumulate, mainly in Kupffer cells of the liver or macrophages in the spleen[186][187] [188]. Accumulation of foreign materials in the body will lead to side effects like chronic inflammation or especially in liver to cirrhosis. This process may be amplified by the use of apolipoprotein E as a tool to target the blood-brain barrier. The liver as main organ of the lipoprotein catabolism will take up a significant fraction of such nanoparticles[189].

1.4.5.5. Nanoparticles and blood coagulation

Blood coagulation is mediated by platelets and plasmatic coagulation system. Platelets are irregularly-shaped anuclear cells of 2-3 μm in diameter. *In vivo* platelets are activated by collagen, thrombin, ADP or negatively charged surfaces[190]. Activation is accompanied by a shape change and a release of α-granules (containing platelet factor 4, fibronectin, B-thromboglobulin, von Willebrand factor, fibrinogen, P-selectin and coagulation factors V and XIII) and dense granules (containing ADP or ATP, calcium, and serotonin). Furthermore, phosphatidylserine and phosphatidylethanolamine are provided on the platelet surface[191]. The released substances and surface components are reactants or catalysts in blood coagulation[192]. Moreover, platelets are able to aggregate, using fibrinogen or von Willebrand factor as connecting agents[191].

The plasmatic coagulation system consists of an extrinsic and an intrinsic pathway, which are organized in cascades. The extrinsic pathway is activated by tissue factor released from damaged tissue or activated cells[190]. The intrinsic pathway is activated via negatively charged surfaces by autoactivation of coagulation factor XII, the kinin-kallikrein system or the complement system[193].

Therefore, foreign and negatively charged surfaces, as presented by nanoparticles, induce or catalyze platelet activation as well as plasmatic coagulation[194][195][196][197].

In this work, a thrombin generation (TG) assay in platelet-rich plasma (PRP) is used to determine activation and activatability of blood coagulation. The newly developed assay monitors the time course of thrombin activity after a low activation of the extrinsic pathway[198][199][200]. Thrombin is the central enzyme of blood coagulation; it cleaves fibrinogen to fibrin (which forms the clot) and activates coagulation factors V, VIII, XI and XIII, the inhibitor protein C, platelets, fibrinolysis and is the one of the most potent activators of the immune system[190]. TG provides information about hypo- and hypercoagulability and the impact of drugs on the coagulation system[201] [202].

Furthermore, the activation of platelets by the nanoparticles is investigated by the determination of P-selectin (also CD62P) expression after incubation with the particle suspension. P-selectin is a cell adhesion molecule but only a small amount could be found on the surface of unstimulated platelets. After activation, P-selectin is released from α-granules and could be detected by specific, fluorescence-labeled antibodies using flow cytometry. Therefore, P-selectin can be considered as a direct marker of platelet activation. To discriminate platelets from other cells, Integrin α-IIb, a part of the constantly expressed platelet glycoprotein IIb/IIIa complex (CD41) is used as a second platelet-specific marker.

On the other hand, an alteration of the coagulation system by nano- or micromaterials may be used as therapeutic or diagnostic option in coagulation-related diseases[83]. Nanoparticles may be used for detection and treatment of arteriosclerosis[203][204] or to target activated platelets[205]. Furthermore, synthetic microparticles with a platelet-like surface can be used as a platelet replacement in patients with thrombocytopenia[206][207].

1.5. Physical properties of nanoparticles

To investigate properties and degradation of nanoparticles, their physical properties have to be considered. The interactions of photons or neutrons with the compounds of the particle or the particle itself provide data on composition, shape and size.

1.5.1. Determination of basic nanoparticle properties

1.5.1.1.   Size and number

With a given particle radius R, the particle volume $V_P = \frac{4\pi}{3} R^3$ and particle mass density ρ the molecular weight M_P is

$$M_P = V_P \rho_P N_A = \frac{4\pi}{3} R^3 \rho_P N_A .$$
(1)

The number N of particles of a weighted sample m equals

$$N = \frac{m}{\rho V_P} = \frac{3}{4} \frac{m}{\pi \rho R^3} .$$
(2)

The surface A_P of one particle is given by $A_P = 4\pi R^2$, whereas the total surface A_T of the weighted sample is

$$A_T = N A_P = 3 \frac{m}{\rho R}$$
(3)

1.5.1.2.   Surface charge

With a given surface charge Q_S with the unit $[Q_S] = C\, m^{-2}$ the number of charges per nanoparticle Q_P equals

$$Q_P = \frac{Q_S}{Q_e} A_T$$
(4)

with Q_e as the elementary charge.

1.5.2. Absorbance of light

Absorbance, also called optical density, quantifies processes that result from the interaction of an incident light beam and the matter the light is running through. One of these processes is absorption, where the energy of a photon is taken up by matter, typically by an electron, and converted to other forms of energy, for example, to heat. The ability of a molecule to absorb light of a certain wavelength depends on its electronic properties. Molecules exhibit a variety of different activation states, defined

by discrete energy differences and can only absorb photons with an energy that equals those differences. This behavior results in molecule-specific absorption bands. On the other hand, these bands are broadened by the uncertainty principle, thermal DOPPLER broadening and inhomogeneities of the sample. Delocalized π-electron systems exhibit a wide variety of possible activation states and, therefore, show increased absorption. The quantity of absorption depends on the concentration of the absorbing material, expressed in the LAMBERT-BEER law.

Furthermore, inelastic or elastic scattering may occur. The former leads to prolonged wavelength of the scattered photon because a part of the photon energy is absorbed by the molecule. Elastic scattering with unchanged photon wavelength is an ideal case, when no energy is transferred.

Whereas the absorption, as described above, depends on the kind of molecule, scattering, in particular elastic scattering depends primarily on the size of the scatterer. Thus, the investigation of the wavelength-dependent absorbance of nanoparticles provides information about their composition and size.

1.5.2.1. Light absorption by spherical nanoparticles and size determination

Based on the RAYLEIGH theory about scattering particles the differential cross section equals to[208]

$$\frac{d\sigma}{d\Omega} = \frac{\pi^2}{2\lambda^4} \alpha_M^2 \bar{\rho} V \left(1 + \cos^2 2\Theta\right) \tag{5}$$

with $\bar{\rho}$ as the number of scattering particles per volume, V the sample volume and α_M the polarizability volume of the scatterer given with unit $[\alpha_M] = m^3$. The scattering angle 2Θ determines the angle between the incident beam and the scattered beam, the differential cross section $\frac{d\sigma}{d\Omega}$ measures the number of photons per unit time which where scattered into the solid angle Ω divided by incoming flux of photons. The total scattering cross section results from

$$\sigma = \int \left(\frac{d\sigma}{d\Omega}\right) d\Omega = \frac{\pi^2}{2\lambda^4} \alpha_M^2 \bar{\rho} V \left(4\pi + \frac{4}{3}\pi\right) = \frac{8\pi^2}{3\lambda^4} \alpha_M^2 \bar{\rho} V \tag{6}$$

In diluted solutions the scattering cross section shows the same behavior like the absorption cross section regarding the reduction of transmittance. Resulting from the LAMBERT-BEER law the initial intensity of light I_0 is reduced after path length l to the remaining intensity $I(l)$ with $I(l) = I_0 e^{\frac{-\sigma l}{V}}$. It follows that

$$\ln\left(\frac{I_0}{I(l)}\right) = \frac{\sigma l}{V} \tag{7}$$

Introducing the turbidity τ with $\tau = \frac{\sigma}{V}$ and equation (7) in the definition of absorbance $A = \log\left(I_0 / I(l)\right)$ results in

$$A = \log e^{\tau l} = \tau l \log e \tag{8}$$

The turbidity can also be defined by using equation (6) with

$$\tau = \frac{8 \pi^2}{3 \lambda^4} \alpha_M^2 \bar{\rho} \tag{9}$$

wherein the volume dependent polarizability volume can be replaced by the dimensionless mean electronic polarizability $\tilde{\alpha}$ with $\alpha_M = \frac{4}{3} \pi R^3 \tilde{\alpha}$. It follows that

$$A = \frac{128}{27} \frac{\pi^5}{\lambda^4} R^6 \tilde{\alpha}^2 \bar{\rho} l \log e \tag{10}$$

The number of scattering particles per volume $\bar{\rho}$ results from the initial particle concentration c_0, the mass density ρ and the particle volume $V_P = \frac{4}{3} \pi R^3$ and equals $\bar{\rho} = \frac{c_0}{V \rho} = \frac{3}{4 \pi} \frac{c_0}{R_0^3 \rho}$ with R_0 as the initial nanoparticle radius. The absorbance of a solution of nanoparticles finally equals

$$A = \frac{32}{9} \pi^4 l \log e \frac{c_0}{R_0^3 \rho} \frac{R^6 \tilde{\alpha}^2}{\lambda^4} = k \frac{R^6}{R_0^3} \frac{\tilde{\alpha}^2}{\lambda^4} \tag{11}$$

From this equation it is apparent that measured absorbance of a nanoparticle solution depends from the forth power of the wavelength λ. Assuming constant polarizability it is possible to calculate particle radii from absorption data[61], with

$R = R_0$ the equation simplifies to $A = k \frac{\tilde{\alpha}^2}{\lambda^4} R_0^3$. Furthermore, it allows to observe nanoparticle degradation by the ratio R^6 / R_0^3

It is noteworthy to consider that these relations are valid for nanoparticles with a diameter smaller than the incident light wavelength. For objects with a size that equals or exceeds the wavelength, scattered waves interfere with each other, which leads to angle dependent amplification or attenuation. In this case LORENZ-MIE scattering theory[209] applies, which includes RAYLEIGH scattering as a special case for very small objects.

1.5.3. Fluorescence emission

After absorption of a photon a molecule achieves a higher energy state. If the molecule relaxes to its ground state the excess energy ends up in molecular rotation, vibrations, heat or the emission of an other photon with lower energy and, therefore, longer wavelength.

There are two different ways to achieve fluorescence emission from nanoparticles. Organic dyes, like fluorescein, rhodamine B or thioflavins exhibiting fluorescence due to delocalized electrons in a conjugated system (fig. 12). The excitation/emission spectra are determined by electronic effects of substituents, fluorescein emits green whereas rhodamine B red light. Furthermore, the spectra depend on the surrounding environment, seen, for example, in the red shift of thioflavin T after binding to β-amyloid[143].

The second way is the use of quantum dots, made from semiconductors like gallium/arsenic or cadmium/selenium. These compounds allow a significant higher quantum yield and stability compared to organic dyes[210], the emission spectrum is dependent on its size. On the other hand, quantum dots show a variety of toxic effects by the used heavy metals and possible oxidatives. Accumulation in the liver[211][212], cytotoxicity[211][213] and DNA damage were described[214].
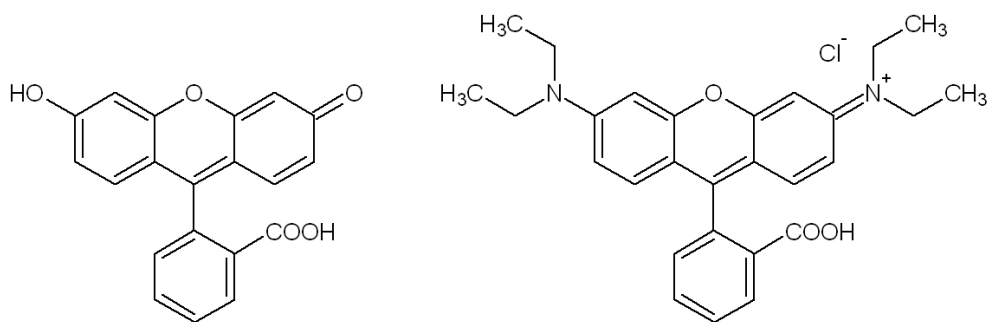
Figure 12: The fluorescence dyes fluorescein and rhodamine B

If a nanoparticle contains more than one fluorescence dye and the emission spectra of one dye (donor chromophore) overlaps with the excitation spectra of the other dye (acceptor chromophore), it is possible to study the integrity of an nanoparticle using FÖRSTER resonance energy transfer (FRET)[215]. After excitation of the donor chromophore a part of the absorbed energy is transferred non-radiatively to the acceptor chromophore which emits light in addition to the emission spectra of the former one. The intensity of the emitted light depends on the distance between the dye molecules with an inverse 6th power law based on the dipole-dipole coupling mechanism[215]. Due to the rapidly decreasing intensity the energy transfer is constricted to a distance of lower than 10 nm. If a nanoparticle with a degradable shell filled with one dye and undegradable core of the other dye, FRET will occur only if the shell is intact. After degradation the distance between the dyes exceeds 10 nm, the FRET signal diminishes. This effect can be used to proof particle degradation within brain tissue of animals treated with nanoparticles.

1.5.4. Light and neutron scattering

1.5.4.1. General scattering theory

Within this section an aqueous solution of light scattering particles will be discussed. The solution may enclose an average of N_{mol} particles in a defined scattering
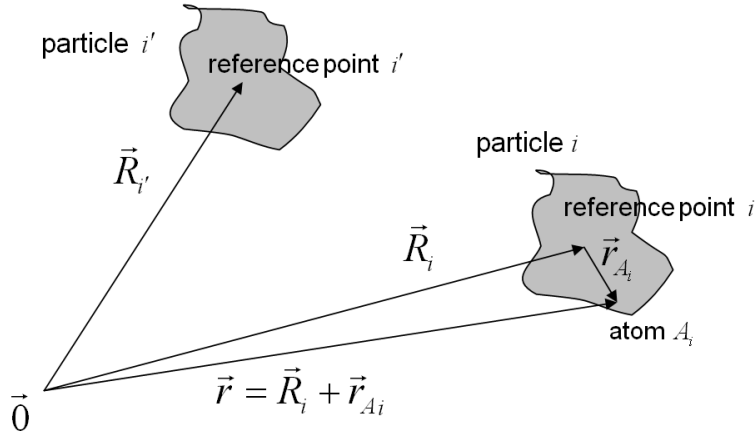
Figure 13: Definition of the position vectors

volume. The particles are numbered with a running index i $\left(i=1,...,N_{mol}\right)$ the position vector is defined as $\vec{R}_i$ (fig. 13). The vector from the reference point of particle i to an atom A_i within the particle is $\vec{r}_{A_i}$. Thus, the position vector of the atom A_i is $\vec{r}=\vec{R}_i+\vec{r}_{A_i}$.

The incident beam is scattered at the atoms of the particles in the solution, the intensity of the scattered beam is detected at an angle ϑ. The wave vector of the incident light is defined as $\vec{k}_e$, the wave vector of the scattered light $\vec{k}_s$ (fig. 14).
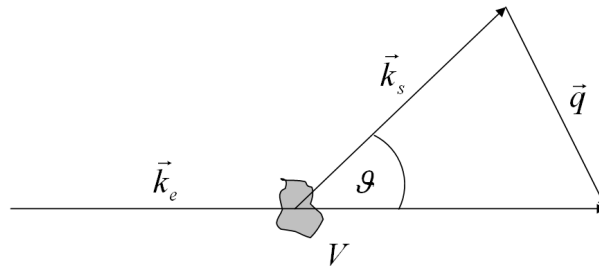
Figure 14: Scattering geometry

The scattering vector $\vec{q}$ is defined as the difference of the former two vectors.

$$\vec{q}\equiv\vec{k}_e-\vec{k}_s \qquad (12)$$

The differential scattering cross section $\dfrac{\mathrm{d}\,\sigma}{\mathrm{d}\,\Omega}$ is the basic measurement of scattering processes. It is defined as scattered power $\mathrm{d}\,P_s$ into the solid angle element $\mathrm{d}\,\Omega$ standardized by the incident intensity j_0.

$$\frac{\mathrm{d}\,\sigma}{\mathrm{d}\,\Omega} \equiv \frac{1}{j_0}\frac{\mathrm{d}\,P_s}{\mathrm{d}\,\Omega}$$
(13)

The differential cross section can also be understood as ensemble average of the squared absolute value of the scattered amplitude $F(\vec{r})$ of the sample.

$$\frac{\mathrm{d}\,\sigma}{\mathrm{d}\,\Omega}(\vec{q}) = \langle |F(\vec{q})|^2 \rangle$$
(14)

The sample scattering amplitude $F(\vec{r})$ is an in-phase interference of the scattering amplitudes $f_i(\vec{q})$ of all N_{mol} particles i in the scattering volume.

$$F(\vec{q}) = \sum_{i=1}^{N_{mol}} f_i(\vec{q})\,e^{-\mathrm{i}\vec{q}\vec{R}_i}$$
(15)

The same applies for the in-phase interference of scattering amplitudes of the atoms A of the particle i in location $\vec{r}_{A_i}$. Within a particle a continuous notation is used to describe scattering centers with continuous scattering length densities $\rho(\vec{r})$.

$$f_i(\vec{q}) \equiv \int_{V_i} \rho(\vec{r})\,e^{-\mathrm{i}\vec{q}\vec{r}}\,\mathrm{d}\,V$$
(16)

The integration is carried out over the particle volume V_i. The scattering length density $\rho(\vec{r})$ is a measure for the scattering strength of the atoms in $\vec{r}$. In light scattering this is determined by the polarizability α, whereas in neutron scattering the scattering strength of the atomic nucleus b comes into play.

Typically, the intensities of a scattering experiment are corrected by the isotropic scattering of the surrounding solvent ρ_S. Therefore, the real scattering length density of the particle $\rho_P(\vec{r})$ is reduced by the scattering length density of the solvent resulting in a relative scattering length density $\rho_{P-S}(\vec{r}) = \rho_P(\vec{r}) - \rho_S$.

$$f_i(\vec{q}) \equiv \int_{V_i} \rho_{P-S}(\vec{r})\,e^{-\mathrm{i}\vec{q}\vec{r}}\,\mathrm{d}\,V$$
(17)

With an adequate high dilution the resulting differential scattering cross section is

$$\frac{d\sigma}{d\Omega}(\vec{q})=\langle|F(\vec{q})|^2\rangle=\left\langle\left|\sum_{i=1}^{N_{mol}}f_i(\vec{q})e^{-i\vec{q}\vec{R}_i}\right|^2\right\rangle=\left\langle\sum_{i=1}^{N_{mol}}\sum_{j=1}^{N_{mol}}f_i(\vec{q})f_j^*(\vec{q})e^{-i\vec{q}(\vec{R}_i-\vec{R}_j)}\right\rangle. \tag{18}$$

Under the assumption, that all particles in the sample are distributed uniformly, but irregular, and independent from each other, averaging over $|f_i(\vec{q})|^2$ and $e^{-i\vec{q}\vec{R}_{ij}}$ can be separated.

$$\frac{d\sigma}{d\Omega}(\vec{q})=\underbrace{\langle|f_i(\vec{q})|^2\rangle}_{form\ factor}\cdot\underbrace{\left\langle\sum_{i,j=1}^{N_{mol}}e^{-i\vec{q}(\vec{R}_i-\vec{R}_j)}\right\rangle}_{structure\ function} \tag{19}$$

The structure function can be developed into a power series depending on the particle concentration[216].

$$\left\langle\sum_{i,j=1}^{N_{mol}}e^{-i\vec{q}(\vec{R}_i-\vec{R}_j)}\right\rangle=N_{mol}\left(1+\gamma c+O(c^2)\right) \tag{20}$$

If one uses a higher sample dilution concentration-dependent terms diminish.

$$\frac{d\sigma}{d\Omega}(\vec{q})\approx N_{mol}\langle|f_i(\vec{q})|^2\rangle \tag{21}$$

Furthermore, it will be assumed that the particles show spherical symmetry, which is a usable assumption for the used nanoparticles.

$$\rho_{P-S}(\vec{r})\equiv\rho_P(\vec{r})-\rho_S\overset{!}{=}\rho_P(r)-\rho_S=\rho_{P-S}(r) \tag{22}$$

Using the GUINIER approximation the form factor $\langle|f_i(\vec{q})|^2\rangle$ for small q-values is

$$\langle|f_i(\vec{q})|^2\rangle=\left\langle\left|\int_{V_i}\rho_{P-S}(r)e^{-i\vec{q}\vec{r}}dV\right|^2\right\rangle=\left\langle\int_{V_i}dV'\rho_{P-S}(r')e^{-i\vec{q}\vec{r}'}\int_{V_i}dV''\rho_{P-S}(r'')e^{-i\vec{q}\vec{r}''}\right\rangle$$
$$=\left\langle\int_{V_i}\int_{V_i}dV'dV''\rho_{P-S}(r')\rho_{P-S}(r'')e^{-i\vec{q}(\vec{r}'-\vec{r}'')}\right\rangle \tag{23}$$
$$=\int_{V_i}\int_{V_i}dV'dV''\rho_{P-S}(r')\rho_{P-S}(r'')\langle e^{-i\vec{q}(\vec{r}'-\vec{r}'')}\rangle$$

With $\langle e^{-i\vec{q}(\vec{r}'-\vec{r}'')}\rangle\approx1-iq(\vec{r}'-\vec{r}'')\langle\cos\theta\rangle-\frac{q^2(\vec{r}'-\vec{r}'')^2}{2}\langle\cos^2\theta\rangle=1-\frac{q^2(\vec{r}'-\vec{r}'')^2}{2}$ follows

$$\langle|f_i(\vec{q})|^2\rangle=\int_{V_i}\int_{V_i}dV'dV''\rho_{P-S}(r')\rho_{P-S}(r'')\left(1-\frac{q^2(\vec{r}'-\vec{r}'')^2}{2}\right). \tag{24}$$

From the definitions

$$\frac{d\sigma}{d\Omega}(0)=\int_{V_i}\int_{V_i}dV'dV''\rho_{P-S}(r')\rho_{P-S}(r'')$$

(25)

and

$$R_G^2=\frac{N_{mol}\int_{V_i}\int_{V_i}dV'dV''\rho_{P-S}(r')\rho_{P-S}(r'')(r'-r'')^2}{2\frac{d\sigma}{d\Omega}(0)}$$

$$=\frac{\int_{V_i}\int_{V_i}dV'dV''\rho_{P-S}(r')\rho_{P-S}(r'')(r'-r'')^2}{2\int_{V_i}\int_{V_i}dV'dV''\rho_{P-S}(r')\rho_{P-S}(r'')}$$

(26)

it follows, that the differential cross section of the sample $\frac{d\sigma}{d\Omega}$ under the assumption

of small q and spherical symmetrical particles (radius of gyration R_G) equals

$$\frac{d\sigma}{d\Omega}(q)=\frac{d\sigma}{d\Omega}(0)\cdot\left(1-\frac{q^2R_G^2}{3}\right)\qquad\forall\,q\,R_G\ll1$$

(27)

The same applies for the macroscopic cross section of the sample $I(q)$.

$$I(q)\equiv\frac{d\Sigma}{d\Omega}(q)=\frac{1}{V}\frac{d\sigma}{d\Omega}(q)$$

(28)

The value V represents the scattering volume of the sample. This results in

$$I(q)=I(0)\cdot\left(1-\frac{q^2R_G^2}{3}\right)\qquad\forall\,q\,R_G\ll1\,.$$

(29)

1.5.5. Scattering of light

The propagation of light can be understood as a continuous scattering of the incident electromagnetic wave from every point of the illuminated medium. In uniform medium all rescattered secondary waves have the same amplitude, which is proportional to the polarizability at its originating point, and interfere destructively except in the direction of the incident beam. If the refraction index at some point differs from its average value, then the resulting secondary waves do not interfere only destructively and light can be observed in different directions. The polarizability and the refractive index are connected by the CLAUSIUS-MOSOTTI-Relation. The scattered light results from heterogeneities within the sample; its properties are determined by the properties of the heterogeneity, which may be molecules or nanoparticles.

Turbidometry and nephelometry are simple light scattering techniques, to determine concentrations but also aggregation, agglutination or phase separation. The former measures the attenuation of transmitted light (absorbance, see chapter 1.5.2.); the latter measures the intensity of scattered light at a fixed angle to the incident light.

1.5.5.1. Basic principles of light scattering

During a light scattering experiment the light scattered by the sample is detected under the angle ϑ. To achieve high intensity, stability and a narrow spectrum and
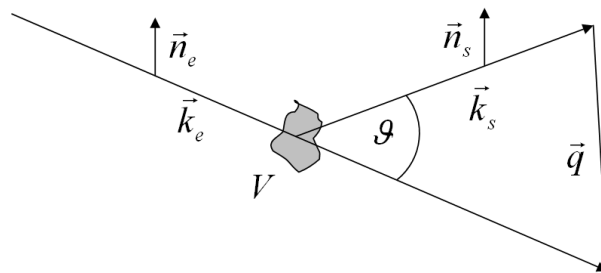
<div align="center">Figure 15: Light scattering process</div>

beam widening, polarized laser light is used. The scattered light is detected using photomultipliers or photo diodes. The scattering process is shown in fig. 15, the point of origin lies in the center of the scattering volume. The vectors $\vec{k}_e$ and $\vec{k}_s$ represent the direction of propagation of the incident and the scattered light.

$$\vec{k}_{els} = k_{els} \cdot \hat{\vec{k}}_{els} = \frac{2\pi n_S}{\lambda_{els}} \hat{\vec{k}}_{els} \tag{30}$$

λ_e and λ_s are the wavelengths of the incident and the scattered waves. For elastic scattering $\lambda_e = \lambda_s$ applies, for inelastic scattering $\lambda_e \neq \lambda_s$. $\vec{n}_i$ and $\vec{n}_s$ represent the direction of polarization, n_S the refractive index of the solvent at wavelength λ_{els}.

For elastic scattering $\left(|\vec{k}_e| = |\vec{k}_s| \right)$ the absolute value of the scattering vector $|\vec{q}|$ is

$$\sin\left(\frac{\vartheta}{2}\right) = \frac{|\vec{q}|}{2|\vec{k}_e|} \quad \rightarrow \quad q \equiv |\vec{q}| = \frac{4\pi n_S}{\lambda} \cdot \sin\left(\frac{\vartheta}{2}\right) \tag{31}$$

The detection unit records count rates, a measure for scattering intensity, with a time resolution from 200 ns. Thereby, the time interval is shorter than dynamic processes within the sample. Depending on the evaluated time interval one differentiates between static and dynamic light scattering.

1.5.5.2.   Static light scattering

If the detected signals are averaged over a long time period (e.g. 30 min), which is large compared with times characteristic for molecular movement processes, the information for dynamic measures like diffusion coefficients or rotational constants disappear. On the other hand, it is a useful method to determine molecular weight and radius of gyration of the scatterer. The derivation of the following equations is given in the appendix (see 7.3).

In static light scattering the ratio Kc/R_ϑ is measured with the RAYLEIGH ratio R_ϑ

$$R_\vartheta \equiv \frac{1}{2\left(\vec{n}_e \vec{n}_s\right)^2} \frac{1}{V} \frac{d\sigma}{d\Omega} ,$$
(32)

an constant K which combines all fixed parameters

$$K \equiv \frac{2\pi^2 n_S^2}{N_A \lambda^4} \left(\frac{dn_D}{dc}\right)^2 ,$$
(33)

And the scattering function $P(\vartheta)$

$$P(\vartheta) = 1 - \frac{q^2 R_G^2}{3} + O\left(q^4 R_G^4\right).$$
(34)

Finally, the ratio equals

$$\frac{Kc}{R_\vartheta} \approx \frac{1}{P(\vartheta)} \left(\frac{1}{M} + 2A_2 c\right)$$
(35)

and is used to interpret data from static light scattering experiment in a GUINIER plot.

1.5.5.3.   GUINIER plot

Data from static light scattering experiments are acquired for different scattering angles and sample concentrations. For small $q^2 R_G^2$ the scattering function $P(\vartheta)$ (eqn. 35) can be approximated by an exponential function.

$$P(\vartheta) = e^{-\frac{1}{3} q^2 R_G^2} \qquad \forall \; \frac{q^2 R_G^2}{3} \ll 1$$
(36)

It follows, that

$$\frac{Kc}{R_\vartheta} \approx e^{\frac{1}{3} q^2 R_G^2} + \left(\frac{1}{M} + 2A_2 c\right).$$
(37)

In a GUINIER plot $\ln\left(\frac{Kc}{R_\vartheta}\right)$ is plotted against $q^2 + \beta c$, whereas β is an arbitrary value.

$$\ln\left(\frac{Kc}{R_\vartheta}\right) \approx \frac{1}{3}q^2 R_G^2 + \ln\left(\frac{1}{M} + 2A_2 c\right) \tag{38}$$

A linear fit $f(q^2) \overset{!}{=} A + B \cdot q^2$ provides the slope $B = R_G^2/3$. Therefore, the radius of gyration can be calculated from $R_G = \sqrt{3B}$. If the refractive index increment $\left(\mathrm{d}\, n_D/\mathrm{d}\, c\right)$ is known, the molecular mass M and the second virial coefficient A_2 can be calculated from double extrapolation of $\vartheta = 0$ and $c = 0$.

1.5.5.4.   Dynamic light scattering

While using dynamic light scattering, the time resolution of the scattered signal is recorded and averaged over time intervals τ from 200 ns up to 100 s or higher. For time intervals lower than 10 ms movement of particles within the sample must be considered. Therefore, the above mentioned data interpretation has to be expanded.

The incident light may be understood as the electrical field according to equation 34. This field polarizes molecules within the scattering volume; thereby, the charged compounds of the molecule (electrons, atomic nuclei) receive a force and, therefore, will be accelerated. According to the classical electromagnetic theory, accelerated charges emit electromagnetic radiation. The incoming field, measured at the detector, is a superimposition of all these emitted fields. Triggered by thermal interactions the molecules perform translation and rotary motion as well as intramolecular vibrations. In consequence, the detected field fluctuates in intensity and phase, but these fluctuations contain information about positions, orientations and motions within the sample. The function of dynamic light scattering is the connecting of the gained information and particle properties. The theoretical background of dynamic light scattering is given in the appendix section (see 7.4).

In dynamic light scattering a characteristic relaxation time τ_R is calculated. τ_R is related to the translational diffusion coefficient D. Moreover, D is related to the hydrodynamic radius R_{hy} by the STOKES-EINSTEIN relation, which results in

$$R_{hy} = \frac{8}{3}\frac{k_B T \pi n_s^2}{\eta \lambda^2}\sin^2\left(\frac{1}{2}\Theta\right)\tau_R . \tag{39}$$

1.5.6. Scattering of neutrons

Whereas light scattering reveals information about the surface of a particle, neutrons are able to penetrate soft matter. The transferred energy is low and, therefore, small angle neutron scattering (SANS) is a non-destructive methodology. Furthermore, neutrons are able to penetrate aqueous solutions and are sensitive to light elements like hydrogen, which is important when studying biological material or polymers. On the other hand, SANS does not provide direct structure information like transmission-electron or atomic force microscopy. Moreover, due to the low energy and the lack of charges, neutron detection efficiency is low and, therefore, time consuming.

1.5.6.1.   Theoretical background of small angle neutron scattering

After transmission of the highly collimated beam through the sample, the neutrons are detected in an angle ϑ typically below 5°. The scattering vector ϑ is defined as given in equation 12. The differential cross section consists of a coherent and an incoherent scattering fraction.

$$\frac{d\sigma}{d\Omega}=\left(\frac{d\sigma}{d\Omega}\right)_{coh}+\left(\frac{d\sigma}{d\Omega}\right)_{inc}$$

(40)

Incoherent scattering origins from scattering of unpolarized neutrons on unpolarized nuclei, and results in a diffuse, angle-independent background signal. Otherwise, the coherent fraction results in an angle-dependent scattering pattern.

$$\left(\frac{d\sigma}{d\Omega}\right)_{coh}(\vec{q})=\left\langle |F(\vec{q})|^2 \right\rangle$$

(41)

$F(\vec{q})$ denotes the form factor of the investigated structure and equals

$$F(\vec{q})=2\int_0^\infty \frac{r\rho(r)\sin(\vec{q}r)}{\vec{q}}dr .$$

(42)

For a particle with a spherical symmetry and the radius R the form factor equals

$$F(q)=3\rho \frac{\sin qR - qR\cos qR}{(qR)^3}$$

(43)

If the particle consists of several layers with the scattering length density $\rho_i(r)$ then equation 42 can be written as

$$F(q)=2\left(\int_0^{R_1} \frac{\rho_1 r\sin(qr)}{q}dr + \int_{R_1}^{R_2} \frac{\rho_2 r\sin(qr)}{q}dr +...+ \int_{R_{n-1}}^{R_n} \frac{\rho_n r\sin(qr)}{q}dr \right).$$

(44)

1.5.6.2. Data acquisition and correction

To obtain radius dependent neutron intensities two different detector technologies are used, either ring-shaped counter tubes or a two-dimensional grid of small square-shaped detector cells. The scattering vector q can be calculated from the distance from the beam center to the detector position r.

$$q = \frac{4\pi}{\lambda} \sin\left(\frac{1}{2}\arctan\left(\frac{r}{L_{SD}}\right)\right) .$$
(45)

Various parameters influence variance of q, an approximation is given by

$$\left[\frac{\Delta q}{q}\right]_{tot} = q\left[\frac{\Delta(2\Theta)}{(2\Theta)}\right]_{tot} \approx \frac{q}{(2\Theta)} \frac{\sqrt{[\Delta(2\Theta)]_{\lambda}^{2} + [\Delta(2\Theta)]_{PSD}^{2} + [\Delta(2\Theta)]_{coll}^{2}}}{2\sqrt{2\ln 2}} .$$
(46)

The wavelength distribution $[\Delta(2\Theta)]_{\lambda} = (2\Theta)(\Delta\lambda/\lambda)$ is determined by time-of-flight measurements. The resolution of the position-sensitive neutron detector depends on the size of a detector cell $[\Delta(2\Theta)]_{PSD} = 2\tan(((2\Theta) - \arctan(r - 0.01)/LSD)/2)/\cos^{2}(2\Theta)$ and the collimation resolution by the length of the collimator and the diameter of the two pinholes $[\Delta(2\Theta)]_{coll} = \sqrt{(d_{H1}^{2} + d_{H2}^{2})}/L_{CS}$.

It should be noted, that the position of the beam center depends from the neutron wavelength. Neutrons which are used in SANS measurements are moderated within the neutron source to a wavelengths typically between 0.5 and 25 Å. These "cold" neutrons travel with $v_n = h \cdot m_n^{-1} \cdot \lambda^{-1}$ (DE BROGLIE relation) between $7900\,\mathrm{m \cdot s}^{-1}$ and $160\,\mathrm{m \cdot s}^{-1}$, respectively, especially neutrons with a higher wavelength are influenced by gravitation. Therefore, detector grids are preferable. On the other hand, the direct beam must be blocked during SANS measurements, because its high intensity may damage the neutron sensitive detectors. The beam center has to be determined in an additional experiment using the direct but attenuated beam. These additional measurements are also used to determine the transmittance T of neutrons through the sample. Absorption processes within the sample, the solvent or the cuvette attenuate the beam intensity as well as the intensity of the scattered neutrons I with $I \propto T$.

The intensity of the scattered neutrons is determined by further parameters. The thickness d of the used sample has two different effects. The increased number of scatterers within the beam increases the measured intensities with $I \propto d$ and

decreases the transmittance which is included in T. The cross section of the beam is defined by a circular hole with an area A around the sample with $I \propto A$. Moreover, the intensity is determined by the distance L_{SD} between the sample and the detector with $I \propto L_{SD}^{-2}$.

In an additional measurement the neutron beam is completely blocked by a cadmium plate to obtain a background signal I_{Cd} which is subtracted directly from the original neutron intensity measurements. Using all above mentioned corrections the initial signal is corrected by

$$I_{corr} = \frac{L_{SD}^2}{A \cdot d \cdot T} \left(I - I_{Cd} \right) . \tag{47}$$

The corrected neutron scattering intensity I_{corr} contains the scattering signal of the sample as well as the scattered neutron originating from the solvent and the cuvette. Therefore, the signal of a cuvette only filled with the solvent is subtracted from the sample signal.

Light water can be used as a calibrator for SANS measurements, the sample signal is corrected by the data obtained with water, an isotropic scatterer with a known scattering intensity $\left(\frac{\partial \sigma}{\partial \Omega} \right)_W$. Finally, the differential cross section $\left(\frac{\partial}{\partial \Omega} \right)_S$ of the sample is corrected by from the measured intensities I (indices S sample, W water, C empty cuvette, b buffer (or solvent) and background Cd)

$$\left(\frac{\partial \sigma}{\partial \Omega} \right)_S = \left(\frac{\partial \sigma}{\partial \Omega} \right)_W \frac{\left(I_S - I_{Cd} \right) \dfrac{L_{SDS}^2}{A_S d_S T_S} - \left(I_b - I_{Cd} \right) \dfrac{L_{SDb}^2}{A_S d_S T_b}}{\left(I_W - I_{Cd} \right) \dfrac{L_{SDW}^2}{A_W d_W T_W} - \left(I_C - I_{Cd} \right) \dfrac{L_{SDC}^2}{A_W d_W T_C}} . \tag{48}$$

The theoretical neutron scattering cross section of water can be estimated by the JACROT-factor F_{Jacrot} using transmission data

$$F_{Jacrot} = \left(\frac{\partial \sigma}{\partial \Omega} \right)_W = \frac{1 - \dfrac{T_W}{T_C}}{4 \pi} g \frac{1}{T_W T_C} . \tag{49}$$

The factor g takes into account that, due to inelastic scattering, the intensity is stronger in the forward direction[217]. g depends on the wavelength λ and is given by

$$g = \frac{1}{1 - e^{-0.6\sqrt{\lambda}}} \tag{50}$$

The error for the calculated neutron scattering intensity ($I_x^* = I_x - I_{Cd}$) is given by

$$\frac{\Delta\left(\frac{\partial\sigma}{\partial\Omega}\right)_S}{\left(\frac{\partial\sigma}{\partial\Omega}\right)_S} = \sqrt{\frac{(L_{SDS}^2 T_b \Delta I_S^*)^2 + (L_{SDb}^2 T_S \Delta I_b^*)^2}{\left(L_{SDS}^2 T_b I_S^* - L_{SDb}^2 T_S I_b^*\right)^2} + \frac{(L_{SDC}^2 T_W \Delta I_C^*)^2 + (L_{SDW}^2 T_C \Delta I_W^*)^2}{\left(L_{SDC}^2 T_W I_C^* - L_{SDW}^2 T_C I_W^*\right)^2}} \ . \tag{51}$$

1.5.6.3. Calculation of the coherent neutron scattering length density

The extent of neutron scattering is an atom-specific property, the neutron scattering length density ρ_n. The coherent neutron scattering length density ρ_n of a particle is calculated from the mass density density ρ_m, the molecular weight M and the sum of coherent scattering lengths b of the each atom of the compound

$$\rho_n = N_A \frac{\rho_m}{M} \sum b_i \tag{52}$$

The neutron scattering length densities of the used substances are given in Table 3.

Table 3: Coherent scattering length density of used compounds

material	sum formula	ρ_m / kg m^{-3}	M / g mol^{-1}	$\sum b_i$ / m	ρ_n / m^{-2}
water	H_2O	1000	18	$-1.680 \cdot 10^{-15}$	$-0.56 \cdot 10^{14}$
heavy water	D_2O	1106	20	$19.15 \cdot 10^{-15}$	$6.37 \cdot 10^{14}$
PS	$[C_8H_8]_n$	1050	104	$23.25 \cdot 10^{-15}$	$1.41 \cdot 10^{14}$
D8-PS	$[C_8D_8]_n$	1130	112	$106.6 \cdot 10^{-15}$	$6.47 \cdot 10^{14}$
PBCA	$[C_8H_{11}O_2N]_n$	1120	153	$32.99 \cdot 10^{-15}$	$1.45 \cdot 10^{14}$
EPMA / MAA (8+1)	$[C_7H_8O_2]_{8n} + [C_4H_6O_2]_n$	~1050	1061	$243.1 \cdot 10^{-15}$	$1.45 \cdot 10^{14}$
Thioflavin T	$C_{17}H_{19}N_2S$	~1200	319	$51.65 \cdot 10^{-15}$	$1.6 \cdot 10^{14}$
Fluorescein	$C_{20}H_{12}O_5$	~1190	332	$83.96 \cdot 10^{-15}$	$2.5 \cdot 10^{14}$
Rhodamine B	$C_{28}H_{31}N_2O_3$	1190	444	$76.22 \cdot 10^{-15}$	$1.7 \cdot 10^{14}$
Tween 80	$C_{64}H_{124}O_{26}$	1080	1309	$112.6 \cdot 10^{-15}$	$0.56 \cdot 10^{14}$
PLE[†]	$C_{2732}H_{4225}N_{703}O_{785}S_{18}$	~1400	60026	$13550 \cdot 10^{-15}$	$~1.9 \cdot 10^{14}$
PLE glycoprotein / sugars[‡]					$1.3 - 2.0 \cdot 10^{14}$

[†]Porcine liver carboxylesterase, amino acids 19-566[218]

[‡]A range is given for the eight different sugars which are contained in eucariotic glycoproteins (β-D-Glucose, β-D-Galactose and β-D-mannose (all $C_6H_{12}O_6$), α-L-fucose ($C_6H_{12}O_5$), N-acetylgalactosamine and N-acetylglucosamine (both $C_8H_{15}NO_6$), N-acetylneuraminic acid ($C_{11}H_{19}NO_9$) and xylose ($C_5H_{10}O_5$) as well as their condensation products). The total mass of the porcine liver esterase glycoprotein is ~162.000 g mol^{-1}. PS - polystyrene, EPMA - 2,3-epoxypropylmethacrylate, PBCA – poly(butyl cyanoacrylate), MAA - methacrylic acid, PLE - porcine liver esterase.

1.5.6.4.   Contrast and contrast variation

Because the neutron scattering of a sample is not measured directly, but by the difference between the sample and the solvent signal (see 1.5.6.2), the difference in the neutron scattering length density of the sample and the solvent determines the intensity of the corrected signal. When using different solvents it is possible to calculate the neutron scattering length density of the sample, which can be used as a marker of the sample composition (Fig. 16)[219]. If one uses an adjusted solvent a component of the sample is "invisible" in the measurement. This is helpful to study a second component in a two-component system exclusively. Therefore, in a core-shell nanoparticle the degradation of the shell can be monitored when the solvent scattering length density matches the core scattering length density.

| 0.0 | 0.2 | 0.4 | 0.6 | 0.8 |
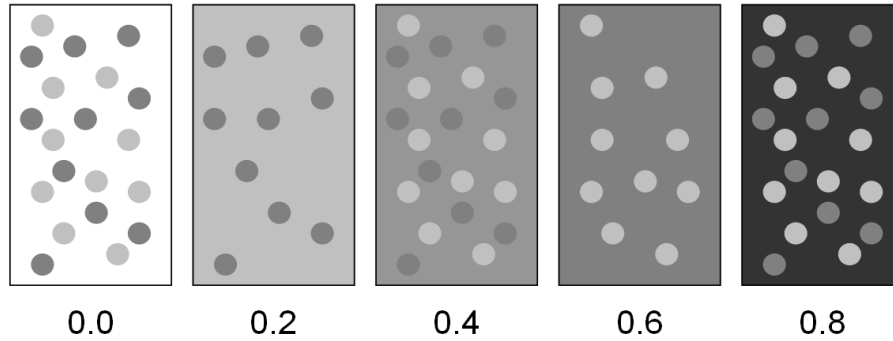
Figure 16: The principle of contrast variation and matching: the observable intensity increases with the contrast difference; objects are "invisible" when embedded in a environment of the same contrast, (bright circles, contrast 0.2; dark circles, contrast 0.6; the contrast of the environment is given below)

From the number N of homogeneous spherical particles in the sample (eqn. 2), the scattering intensity $I(q)$ can be calculated as (eqn. 28 and 43)

$$I(q,\rho)=\frac{c\,V_P}{\rho_M}\rho^2\frac{9}{(q\,R)^6}\left(\sin(q\,R)-q\,R\cos(q\,R)\right)^2.\tag{53}$$

For $q\rightarrow 0$ this relationship simplifies to

$$I(0,\rho)=\frac{c\,V_P}{\rho_M}\rho^2.\tag{54}$$

ρ denotes the neutron scattering length density difference between the sample and the solvent. It is noteworthy, that $I(0,\rho)$ is a non-negative value, although the scattering length density difference may be negative and results in a v-shaped graph. For the easier interpretation of the data, values that lie above $\rho_{sample}=\rho_{solvent}$ are

multiplied by -1. If the resulting relationship between $I(0,\rho)$ and ρ^2 is linear then the investigated sample can be considered as homogeneous.

1.5.6.5. GUINIER plot and radius of gyration

Analogous to static light scattering there is a nearly linear relationship between the natural logarithm of the intensity $\ln(I(q))$ and the squared scattering vector q^2 for small values of q

$$\ln(I(q)) \approx \ln(I(0)) - \frac{1}{3} q^2 R_G^2 . \tag{55}$$

A linear fit with $f(q^2) = A + B \cdot q^2$ allows direct determination of the radius of gyration for the used sample $R_G = \sqrt{-3B}$. The radius of gyration is a measure of the size of an object and it is calculated as the root mean square distance of the objects' parts from either its center of gravity or an axis. Under the assumption of small q-values and small particle polydispersity R_G can approximated[219] by

$$R_G^2 \approx \frac{\int\limits_0^\infty d\,r\,\rho(r)r^4}{\int\limits_0^\infty d\,r\,\rho(r)r^2} . \tag{56}$$

For a homogeneous sphere with a radius R, the neutron scattering length density ρ and no polydispersity, R_G is approximated by

$$R_G^2 \approx \frac{3}{5} R^2 . \tag{57}$$

For a core-shell nanoparticle without polydispersity (core R_C and ρ_C, shell R_S and ρ_S) the radius of gyration can be estimated by

$$R_G^2 \approx \frac{3}{5} \frac{(\rho_C - \rho_S) R_C^5 + \rho_S R_S^5}{(\rho_C - \rho_S) R_C^3 + \rho_S R_S^3} . \tag{58}$$

1.5.6.6. Fit models and procedure

Because the above mentioned relationships are mostly valid for homogeneous particles with no or very low polydispersity two different fit models were introduced, to estimate specific particle properties from $I(q)$ for greater q-values. Using equation 44 the neutron scattering intensity of a multilayer spherical particle can be written as

$$I(q) = K \cdot \left(2 \sum_{i=1}^{n} \left(\int_{R_{i-1}}^{R_i} \frac{\rho(r) r \sin(qr)}{q} \, dr \right) \right)^2 . \tag{59}$$

Both models are based on an assumed scattering length density distribution. In the first model (1) the nanoparticle is assumed a spherical particle with a core radius R_C, a shell radius R_S with corresponding contrast, and a total radius R_I (fig. 17). The latter takes into account that the particle surface may be inhomogeneous due to solvent entry. The scattering length density of the inhomogeneity is assumed to fall linearly from R_S to R_I. Additionally, R_I is estimated to be GAUSSIAN distributed.

$$I(q) = \frac{4}{\sqrt{2\pi\sigma_X^2}} \int_{-\infty}^{\infty} \left(\left(\int_0^{R_C+X} \frac{\rho_C r \sin(qr)}{q} dr + \int_{R_C+X}^{R_S+X} \frac{\rho_S r \sin(qr)}{q} dr + \int_{R_S+X}^{R_I+X} \rho_S \left(1 - \frac{R_I-r}{R_I-R_S}\right) \frac{r\sin(qr)}{q} dr \right)^2 e^{-\frac{1}{2}\frac{X^2}{\sigma_X^2}} \right) \tag{60}$$

Furthermore, the radii R_C and R_S are estimated by their difference to R_I with $l = R_I - R_C$ and $d = R_I - R_S$. As a consequence of this definition R_C as well as R_S show the same radius distribution as R_I.
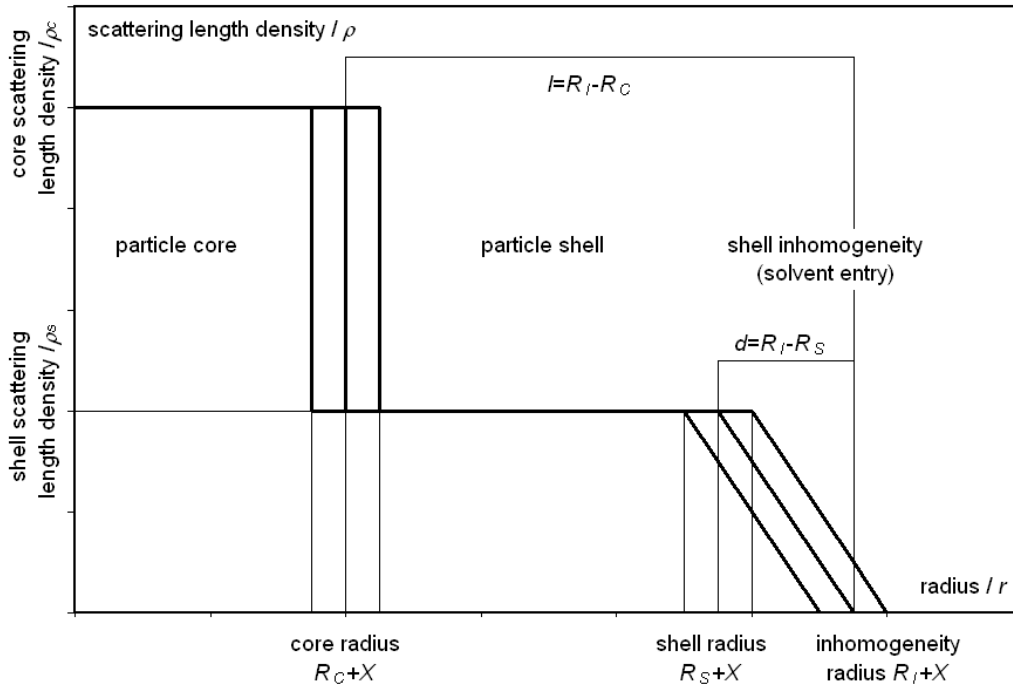
Figure 17: Nanoparticle scattering length density profile according to model 1: the parameters R_I, d and l are fitted as well as the Gaussian distributed X. Due to the definition of d and l the radii R_S and R_C show the same distribution. Note, that the scattering length densities of nanoparticle core and shell represent the difference to the solvents scattering length density, therefore, also negative values are possible.

Model 1 was designed to achieve the lowest possible number of variables in a fit procedure. A disadvantage of this model is the uniform radius distribution of the all three radii. Nevertheless, it can be used to analyze homogeneous nanoparticles and to estimate the radius dimensions for further analysis.

In the second model (model 2) the nanoparticle consists of a core radius R_C, a shell thickness R_S, both Gaussian distributed (standard deviation X and Y, respectively) and an inhomogeneity with a thickness R_I (fig. 18). The scattering length density of the inhomogeneity is assumed to fall linearly within R_I.
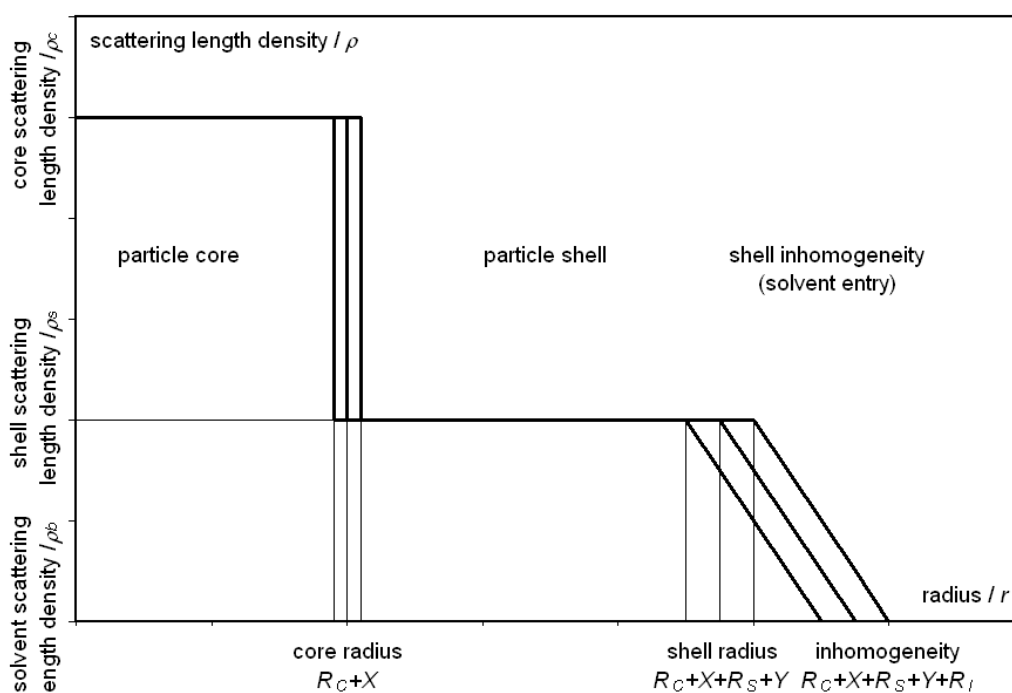
Figure 18: Nanoparticle scattering length density profile according to model 2: R_C, R_S and R_I are fitted as well as the Gaussian distributed X and Y. Note, that the scattering length densities of nanoparticle core and shell represent the difference to the solvents scattering length density, therefore, also negative values are possible.

In this model five variables are used in the fit procedure. Due to the variance in data, the broadened neutron wavelength distribution and detector dimensions it would be impossible to gain reliable results, especially for the widths of the radius distributions. On the other hand, this model can be used if cores of a core-shell nanoparticle were investigated separately and, therefore, the data of the shell could be estimated while the core data will be fixed. Furthermore, this model can be used if data from contrast variation series are fitted simultaneously.

The definition of the variables in both models allows to reduce their number in the fit procedure if a homogeneous nanoparticle is investigated. Furthermore, the used equations contain exclusively integrals that can be solved analytically and, therefore, improve accuracy and reduce computing time.

For data fitting a slightly modified Nelder-Mead simplex method (or downhill simplex method) is used[220][221]. Besides the above mentioned parameters a scaling factor K was fitted (see eq. 59) as well as a asymptotic intensity I_{asy} which corrects the fact that the intensity may not fall to exact zero for high values of q.

1.5.7. Nanoparticle design

To investigate nanoparticle structure and properties different types of polymeric nanoparticles were applied in this work.

Core-shell nanoparticles were used for the investigation of the uptake into the brain. Uncoated particles as well as negatively charge polystyrene cores of early degraded particles are unable to cross the blood-brain barrier[189]. Due to its hydrophilic properties early released dye can not cross the blood-brain barrier either (fig. 19). Intact nanoparticles will be degraded after endocytosis or transcytosis by endothelial cells. In both cases the stable core may remain in place whereas the released model drug thioflavin T may diffuse to its target β-amyloid. The uptake can be proven by the fluorescence of the remaining particle core, the targeting of β-amyloid by the fluorescence of the dye.

To investigate nanoparticle degradation characteristics, homogeneous particles of poly(butyl cyanoacrylate) as well as core-shell nanoparticles were used.
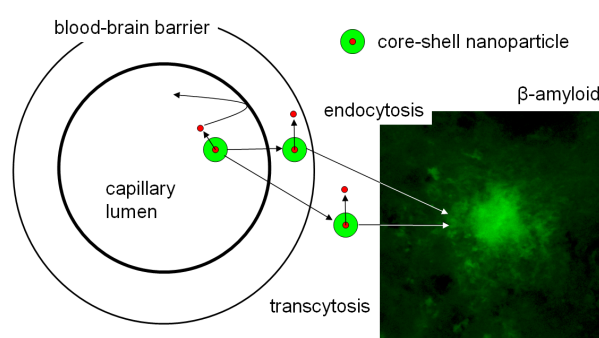
Figure 19: Principle to verify nanoparticle uptake, drug release and targeting. After the ApoE-mediated penetration of the blood-brain barrier by endocytosis or transcytosis the nanoparticle is degraded; the model drug, which is enclosed in the degradable shell (green), is released and binds to its target β-amyloid, whereas the stable core (red) remains at the site of degradation. Core particles from premature degradation within the capillary lumen are unable to pass the blood-brain barrier due to the lack of the ApoE signal.

Furthermore, to investigate the influence of nanoparticle composition and surface, particles consisting of undegradable poly(methyl methacrylate) and poly(methacrylic acid) were introduced.

For the small-angle neutron scattering experiments core-shell nanoparticles are used to determine structure and degradation of the polymeric material. Polystyrene and poly(butyl cyanoacrylate) have similar neutron scattering length densities; therefore, perdeuterated d8-polystyrene were used to achieve a high contrast between particle core and shell. With these particles it is possible to observe the degradation of the shell material directly.

2. Materials, devices and methods

2.1. Materials

2.1.1. Chemical substances

Common chemicals in standard purity grade, unless otherwise noted, are purchased form Merck (Darmstadt, Germany), Sigma-Aldrich (Taufkirchen, Germany), Carl Roth GmbH (Karlsruhe, Germany), Fluka (Buchs, Switzerland) or other manufacturers.

2.1.1.1.   Dyes, fluorogenic substrates

Thioflavin T, Thioflavin S and BTA-2	Sigma-Aldrich, Taufkirchen, Germany
Z-Gly-Gly-Arg-AMC	Bachem, Heidelberg, Germany

2.1.1.2.   Antibodies, lectins

Rabbit anti-β-amyloid SA 720 and SA 721	Schering AG, Berlin, Germany
Cy2-, Cy3- and Cy-5-tagged goat-anti-mouse IgG and IgM	Dianova, Hamburg, Germany
Biotinylated-goat-anti-mouse IgG	Dianova, Hamburg, Germany
Biotinylated *Solanum tuberosum* lectin	Vector, Burlingame, CA, USA
Cy3 and Cy5-streptavidin	Dianova, Hamburg, Germany
PE-labeled anti-human GPIIb/IIIa (CD41)	Beckman Coulter, Krefeld, Germany
FITC-labeled anti-human GMP (CD62P)	Beckman Coulter, Krefeld, Germany

2.1.1.3.   Enzymes, proteins, peptides

Porcine liver carboxylesterase EC 3.1.1.1	Sigma-Aldrich, Taufkirchen, Germany
	(E 3019, activity >15 units/mg)
Lipidated tissue factor	Bachem, Bubendorf, Switzerland
Biotinylated ApoE dipeptide $(141\text{-}150)_2$	Kindly provided by Dr. M. Dathe (FMP, Berlin)
(Ac-LRKLR KRLLR LRKLR KRLLR-NH_2)	

2.1.1.4.   Sera

Bovine serum albumin	Serva, Heidelberg, Germany
Normal donkey serum	Dianova, Hamburg, Germany
Normal goat serum	Dianova, Hamburg, Germany
Normal rabbit serum	Sigma-Aldrich, Taufkirchen, Germany

2.1.1.5.   Microscopy

Sudan Black B	Merck, Darmstadt, Germany
Entellan (in toluene)	Merck, Darmstadt, Germany
Glycerol / gelatin	Sigma-Aldrich, Taufkirchen, Germany
Durcupan	Fluka, Buchs, Switzerland

2.1.1.6.   Other chemicals

Pathromtin SL	Siemens Healtcare Diagnostics, Eschborn, Germany
Thrombin receptor activating peptide 6 (TRAP-6, SFLLRN)	
	möLab GmbH, Langenfeld, Germany
Adenosine diphosphate	möLab GmbH, Langenfeld, Germany

2.1.2. Buffers and solutions

2.1.2.1.   Hank's Buffered Salt Solution (HBSS)

0.137 M sodium chloride, 5.4 mM potassium chloride, 0.25 mM disodium phosphate dihydrate, 0.44 mM monopotassium phosphate, 1.3 mM calcium chloride, 1.0 mM magnesium sulfate and 4.2 mM Sodium bicarbonate in distilled water.

2.1.2.2.   PBS buffer, pH 7.4

571 mg monosodium phosphate dodecahydrate (1.7 mM), 926 mg disodium phosphate dihydrate (5.2 mM) and 8.5 g sodium chloride in 1 l deionized water.

2.1.2.3.   TBS buffer (Tris-buffered saline)

12.1 g Tris(hydroxymethyl)aminomethane (100 mM) and 8.5 g sodium chloride adjusted to pH 7.4 with hydrochloric acid and filled up to 1 l with deionized water

2.1.2.4.   0.05 M TBS buffer, pH 8.0

6.05 g Tris(hydroxymethyl)aminomethane (50 mM) and 8.5 g sodium chloride adjusted to pH 8.0 with hydrochloric acid and filled up to 1 l with deionized water

2.1.2.5.   Storage buffer, TBS-NaN$_3$

0.2% sodium azide (w/v) in TBS buffer

2.1.2.6.   Staining buffer, pH 8,0

6.05 g Tris(hydroxymethyl)aminomethane (50 mM), adjusted to pH 8.0 with hydrochloric acid and filled up to 1 l with deionized water

2.1.2.7. TBS-BSA buffer

2% bovine serum albumin (w/v) in TBS buffer

2.1.2.8. Goat, donkey and rabbit blocking solution

5% normal goat, donkey or rabbit serum and 0.3% Triton X-100 in TBS buffer

2.1.2.9. ABC-Complex

12.5 µg/ml streptavidin (stock solution: 1 mg/ml in PBS:glycerol 56:44, (v/v)) and 2.5 µg/ml biotinylated horseradish peroxidase (horseradish peroxidase modified by biotinylamidocaproyl-N-hydroxy-succimide ester; stock solution: 0.5 mg/ml in PBS:glycerol 56:44, (v/v)) in TBS-RSA, one hour incubated at room temperature[222]

2.1.2.10. DAB-nickel solution

2 mg 3,3'- Diaminobenzidine tetrahydrochloride and 40 mg ammonium nickel sulfate hexahydrate in 10 ml staining buffer (Tris buffer, pH 8.0)

2.1.3. Animal experiments

2.1.3.1. Mice

In the present work, two different strains of animals were investigated.

The APPswe/PS1(A246E)[151] double transgenic mouse strain was crossbred in C57BL/6J. The resulting mice express amyloid precursor protein (695 isoform, Swedish double mutation K595N and M596L) as well as presenilin-1 (Finnish mutation A246E) causing an accelerated Aβ deposition in brain[151]. These mice show typical signs of progressive memory impairment dependent on the amount of insoluble (aggregated) $A\beta_{42}$ within the hippocampus[153].

The APPswe/PS1dE9[152] double transgenic mouse strain was crossbred in C57BL/6J. Newly generated mice express amyloid precursor protein (695 isoform, Swedish double mutation K595N and M596L) as well as presenilin-1 (deletion of exon 9). These animals display a significant plaque number after six months[223].

The double transgenic mice were a courtesy gift of Dr. Heikki Tanila (Departments of Neuroscience and Neurology, University of Kuopio, Finland) and Drs. Joanna L. Jankowsky and David Borchelt (Department of Pathology, Johns Hopkins

University, Baltimore, MD, USA), the colony founders of both APPswe/PS1dE9 and APPswe/PS1(A246E) mouse strains.

2.1.3.2. Medication

Hypnomidate®   Janssen-Cilag, Neuss, Germany

Xylocitin®   Jenapharm, Jena, Germany

2.2. Devices

2.2.1. Microscopy

2.2.1.1. Light and fluorescence microscopy

Axioplan   Carl Zeiss, Jena, Germany

Axioplan 2   Carl Zeiss, Jena, Germany

     equipped with Sony DXC-930P, 3 CCD Color Video Camera

Axiophot   Carl Zeiss, Jena, Germany

2.2.1.2. Confocal laser-scanning microscopy

LSM 510 Meta NLO   Carl Zeiss, Jena, Germany

TCS SP2 AOBS   Leica Microsystems, Wetzlar, Germany

     laser light source Argon-ion-laser, Acousto-Optical Beam Splitter

2.2.2. Photometry, fluorescence spectroscopy, flow cytometry

Anthos HTIII ELISA reader   Anthos Labtec Instruments, Salzburg, Austria

Jasco V560 Spectrophotometer   Jasco Corp, Gross-Umstadt, Germany

Jobin Yvon Spex Fluoromax-2   Instruments S.A., Edison, NJ, USA

Fluoroskan Ascent   Thermo Labsystems, Helsinki, Finland

Epics XL flow cytometer   Beckman Coulter, Fullerton, FL, USA

2.2.3. Animal experiments

Slide microtome Leica SM2000R   Leica Microsystems, Wetzlar, Germany

Stereotaxic frame   Stoelting, Wood Dale, IL, USA

2.2.4. Small angle neutron scattering

The determination of small angle neutron scattering is technically challenging; the quality of the results depends strongly on the neutron quantity, narrow neutron wavelength distribution and resolution of the detectors. Therefore, all three used instruments and facilities ("YuMO" at Frank Laboratory of Neutron Physics, Dubna, "Yellow Submarine" at the Budapest Neutron Centre and "V4" at Berlin Neutron Scattering Center) are described briefly.

2.2.4.1.   YuMO - Small angle scattering spectrometer at Frank Laboratory of

Neutron Physics, Joint Institute for Nuclear Research, Dubna, Russia

The YuMO small-angle instrument[224] is installed at the 4th channel of the IBR-2 reactor (fig. 20). The IBR-2 is a pulsed neutron source[225] fueled with PuO_2 which is cooled by liquid sodium. By means of two synchronized neutron reflectors pulses with a frequency of 5 Hz and a peak power of 1.500 MW are generated. During burst maximum $10^{16} n \, \mathrm{cm^{-2} s^{-1}}$ are emitted on the moderator surface.
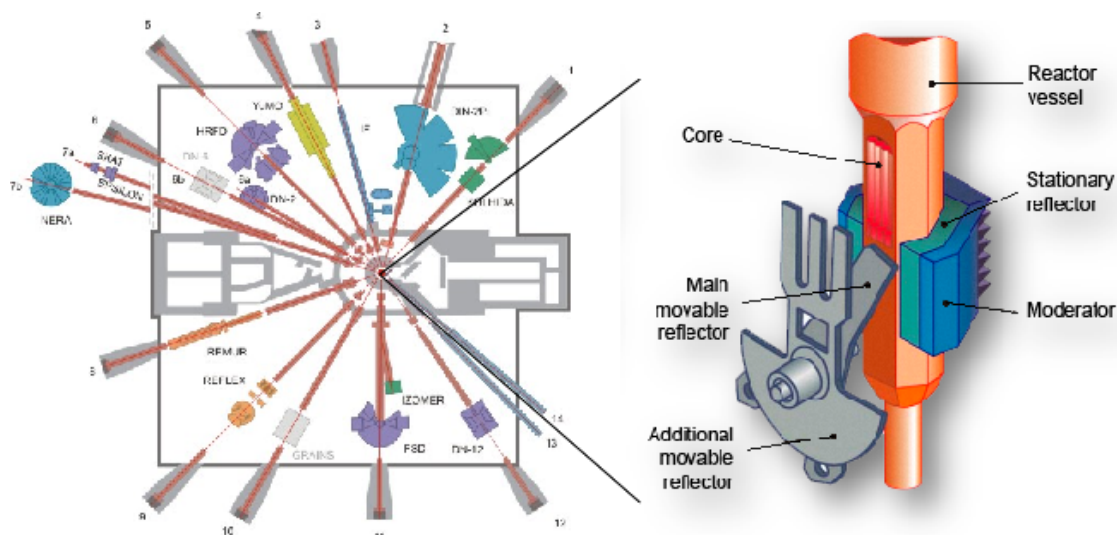
Figure 20: Experimental facilities on IBR-2 beams (small angle neutron scattering instrument YuMO on beam 4) and design of the IBR-2 reactor[225]

The SANS diffractometer YuMO operates with cold as well as thermal neutrons. Therefore, the instrument needs an extensive shielding with cadmium-loaded heavy concrete and a lockable sample changer (fig. 21) Due to its time-of-flight setup, neutrons are not selected by a velocity selector but by the time in which the neutrons

travel from the core to the detector. Higher neutron energy results in a shorter wavelength and a higher speed (DE BROGLIE relation).

The neutron flux on the sample reaches $10^7 - 4 \cdot 10^7 \, n \, \text{cm}^{-2} \, \text{s}^{-1}$ with a q-range of $7 \cdot 10^{-3} - 0.5 \, \text{Å}$. Using the cold moderator the neutron wavelength ranges from 0.5 to 8 Å. The scattered neutrons are detected time-dependently by two ring detectors, each detector consists of eight independent ^{3}He-filled wires

$$^3He + n \rightarrow p + {}^3H \tag{61}$$

Furthermore, the sample transmission is detected by a direct beam detector based on ^{6}Li. The calibration can be done by an insertion of a movable vanadium standard.
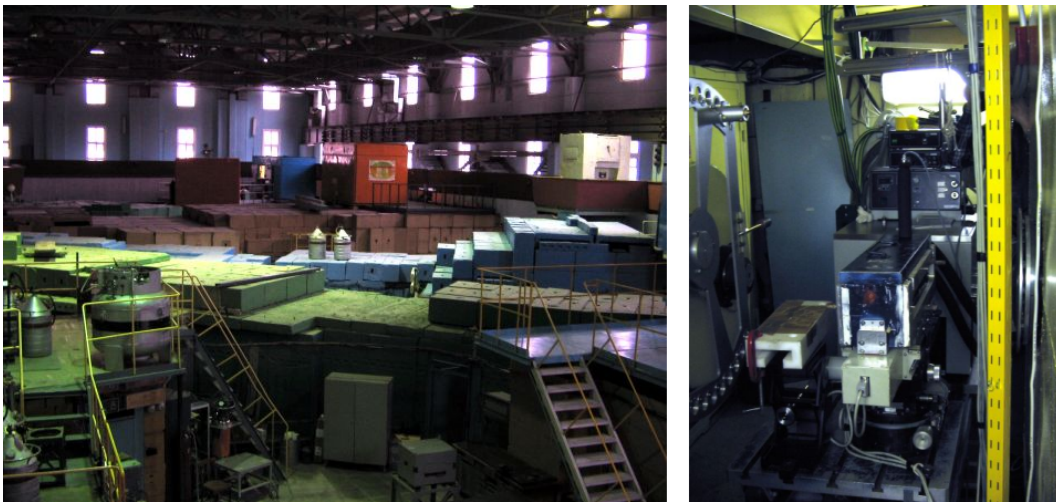
Figure 21: View into the experimental hall (left) and on the YuMO cuvette holder (right) at the Frank Laboratory of Neutron Physics, Dubna

2.2.4.2. Yellow Submarine - SANS diffractometer at Budapest Neutron Centre

SANS diffractometer at the Budapest Neutron Center is placed on beam 2 in the CNS measuring hall originating from the Budapest Research Reactor BRR (fig. 59). This reactor is a tank-type reactor, moderated and cooled by light water[226]. The neutrons are produced using VVR-SM rods (^{235}U) and beryllium based reflectors which result in a nominal thermal power of 10 MW and a neutron flux of in the core.

Due to the continuous neutron flux the neutron wavelength is determined by a mechanical multi-disk velocity selector ranging from 3 to 25 Å. The instrument covers a the transferred momentum (q-range) from 0.003 to 0.5 Å^{-1} allowing to measure

density compositions on a length scale from 5 up to 1400 Å[227]. Samples are placed in a automatic sample changer (fig. 23) and can be tempered between -30 and 150°C. The neutron flux at the sample is $5 \cdot 10^7 n\,\mathrm{cm}^{-2}\mathrm{s}^{-1}$, scattered neutron are detected by a movable 2D multi-detector with 64 x 64 square cells each 1 cm^2 filled with BF$_3$. The detector measures indirectly the induced release of charged α particles

$$^{10}B + n \rightarrow \alpha + {}^7 Li \tag{62}$$
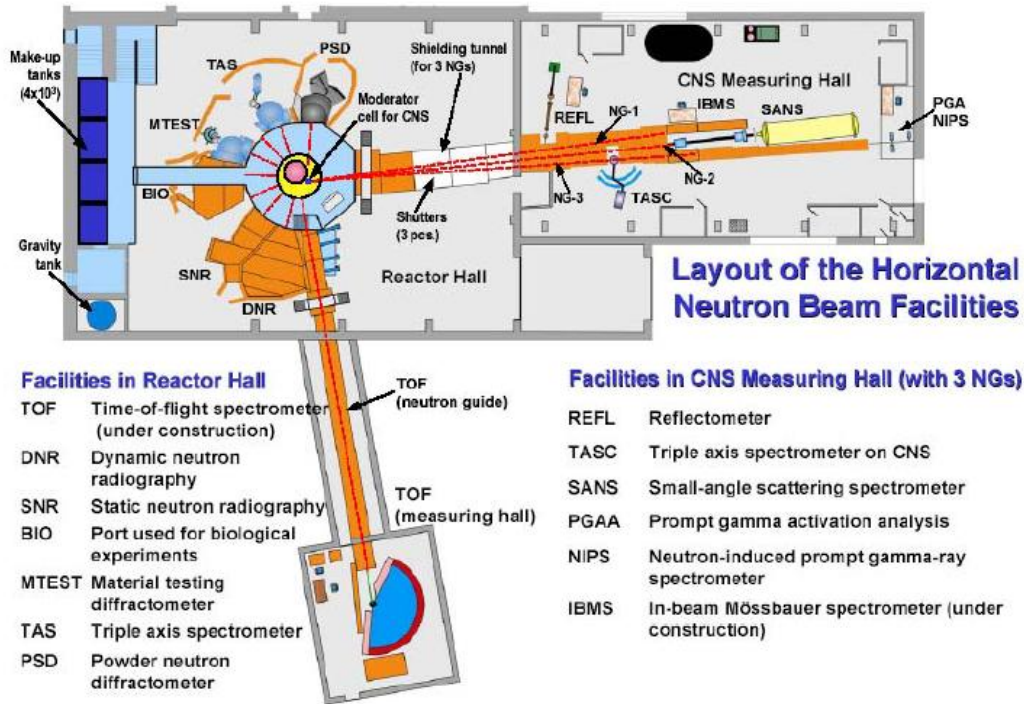
Figure 22: Budapest Research Reactor and experimental facilities on BNC, Budapest[226]

Figure 23: Small angle neutron scattering detector "Yellow Submarine" (left) and automatic sample changer (right) at Budapest Neutron Centre

2.2.4.3.   V4 - Small Angle Neutron Scattering Instrument at Berlin Neutron Scattering Center at Hahn-Meitner-Institute

The research reactor BER II is a light water cooled and moderated reactor operating at 10 MW thermal power[228]. The core operates with 24 fuel elements and six additional control elements consisting of low enriched uranium. The core is surrounded by beryllium reflectors where the neutron flux amounts to $1.2 \cdot 10^{14} \, n\,\mathrm{cm}^{-2}\mathrm{s}^{-1}$. The cold source is operated with hypercritical hydrogen at about 25 K and 14-17 bar; cold neutrons from the moderator are delivered by eight curved neutron guides into the experimental hall (fig. 24).

The small angle neutron diffractometer V4 is installed at the neutron guide NL3a. Incoming neutrons are monochromatized by a mechanical velocity selector with variable wavelength resolution (from 8% to 18%) and collimated on a variable length from 1 to 16 m. A high transmission supermirror allows the use of polarized neutrons and can be introduced by remote control.
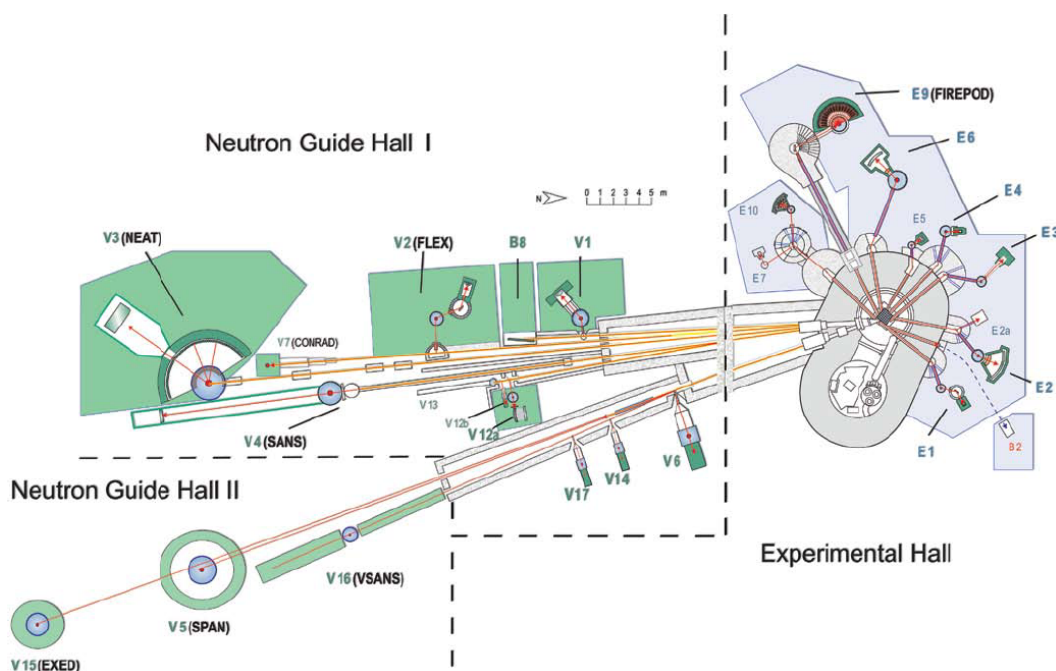
Figure 24: The research reactor BER II and neutron scattering instrumentation at BENSC, Berlin[228]

Neutron flux at sample is up to $2 \cdot 10^{7} \, n\,\mathrm{cm}^{-2}\mathrm{s}^{-1}$. The automatic sample changer is placed in a pressure vessel to avoid scattering from air humidity and to allow setups with different temperatures and pressures (fig. 25). The neutron detector can be

moved from a sample detector distance of 1 m up to 16 m. It consists of a 2D ^{3}He gas detector with a size of 64 x 64 cm^2 with a pixel size of 5 x 5 mm. The data are acquired in a histogram mode but also allow a list mode for time-stamped experiments.

Figure 25: The SANS diffractometer V4 at BENSC, Berlin[228]

2.2.5. Light scattering, ALV/DLS-5000 compact goniometer system

The ALV/DLS-5000 compact goniometer system (ALV GmbH, Langen, Germany) allows simultaneous angular dependent determination of dynamic and static light scattering systems. A scheme of the basic setup is given in fig. 26.
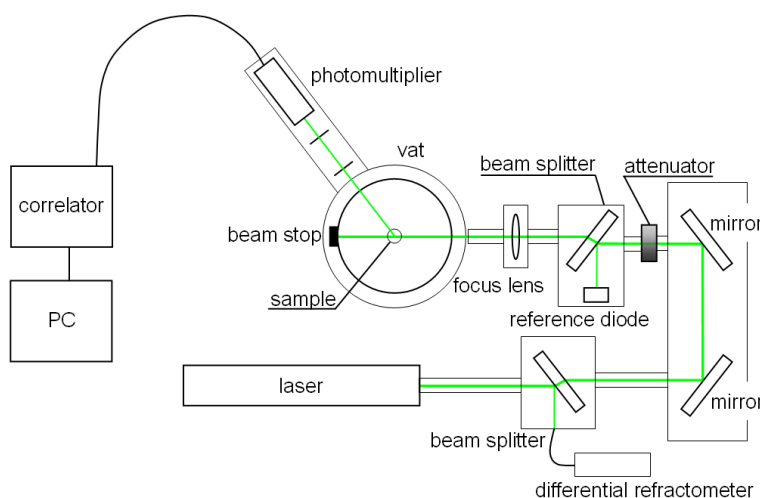
Figure 26: Layout of the ALV-5000 compact goniometer system

Laser light source is a 120 mW frequency-doubled continuous wave diode-pumped Nd:YAG laser (DPY 315 II, AdLas GmbH, Lübeck, Germany) with a wavelength of 532 nm. To achieve a longtime stable signal and a prolonged durability, the laser was operated at about 50 mW. The diverted beam from the first beam splitter is used in a differential refractometer to determine the refraction index increment of the sample. Two adjustable mirrors are used to guide the beam into the center of the detection system. The beam may enter and leave the vat exactly perpendicular to the vat wall. Between the second mirror and the vat an liquid crystal attenuator is placed (model 932-CX, Newport Cooperation, Irvine, CA, USA), as well as a second beam splitter and a focus lens). At the second beam splitter the intensity and spatial stability of the attenuated laser beam is determined using a 4-quadrant photo diode. A shutter allows to block the beam, which is needed to protect the detection system when the sample is changed.
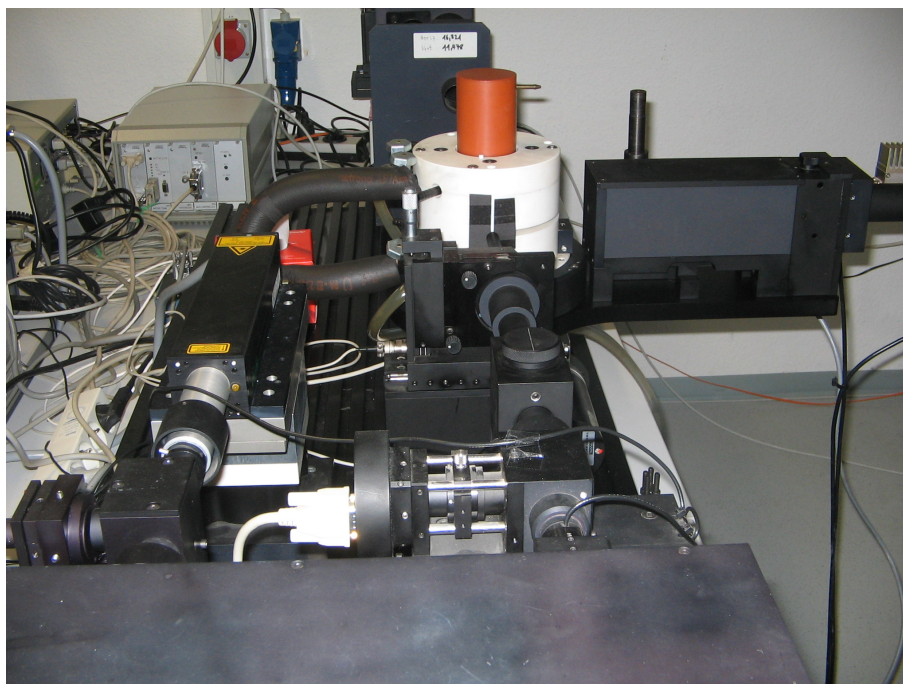
Figure 27: ALV-5000 compact goniometer system (see fig. 26 for layout details, view from the right side)

The vat is filled with toluene which fits the refractive index of the vat as well the cylindrical sample cuvettes to avoid reflections. The vat is placed in a socket which contains a sample holder, a temperature control system and the detection system. The latter consists of a rotatable base, high-precision step motor, a detection unit to focus on the scattering volume, and a photomultiplier. The time-dependent counting

rate is analyzed by a auto correlator (ALV-5000 multiple tau digital correlator), and the resulting data were analyzed with an attached computer.

During this work the ALV/DLS-5000 compact goniometer system was disassembled, rebuild and newly adjusted. The manual[229][230] gives only a short description, therefore, a detailed description for the vat socket and vat adjustment is given by Steffen Lindert[219], whereas a description of the focus lens and the photomultiplier adjustment is provided in the result section (see chapter 3.2.1.).

2.2.6. Software

Text	OpenOffice.org 3.2 Writer
Tables	OpenOffice.org 3.2 Writer, Microsoft Office Excel 2003
Figures	ACD/ChemSketch 12, Adobe Illustrator CS2, IrfanView 4.20, Microcal Origin 5, Microsoft Office Excel 2003, Microsoft Office PowerPoint 2003, Waterloo Maple 7
Programming	Borland Delphi 10 for Microsoft Windows

2.3. Methods

2.3.1. Nanoparticle synthesis

All used nanoparticles were synthesized by Dr. Bernd-Reiner Paulke[32], Fraunhofer Institute for Applied Polymer Research, Science Center Golm. The nomenclature of the nanoparticles was given by Dr. Paulke. The nanoparticles were named 'HL' for 'Härtig Latices' followed by a consecutive number.

Thioflavin T is bound non-covalently to the nanoparticles by inclusion or adsorption, this also applies for thioflavin S. The dye rhodamine B is bound covalently to the nanoparticles.

2.3.1.1.   Polystyrene core HL-22 (core of HL-23)

166 ml of ultra-pure water were mixed with 10 ml of absolute ethanol, 27 mg sodium tetraborate, 30 mg thioflavin T and 300 mg sodium dodecyl sulfate. Under stirring (350 min^{-1}) and nitrogen gassing 12 g styrene were added under nitrogen gassing within 20 minutes. The continuously stirred mixture was heated up to 60°C (reflux condenser) for 24 hours. Next, the reaction was started by adding 134 mg potassium peroxidisulfate in 20 ml ultra-pure water. The resulting intensive colored colloidal polymer dispersion with a solids content of 5.6% was dialyzed for 7 days. The final dispersion contains a solids content of 4.8% with a mean particle radius of 34 nm.

2.3.1.2.   PS-PBCA core-shell nanoparticles HL-23

20.7 ml dialyzed latex HL-22 (equals 1 g) were primarily mixed with 2 g Poloxamer 188 and 5 mg thioflavin T. The solution was then adjusted to pH 2 with hydrochloric acid and filled up to 200 ml with ultra-pure water. Subsequently, 2 g butyl cyanoacrylate were added under stirring (400 min^{-1}) for 4 hours at 4°C. The reaction mixture was neutralized with sodium hydroxide and the resulting core-shell nanoparticles were purified by dialysis and ultracentrifugation. Resulting particles displayed a radius of 64.5 nm and a solids content of 2.2%.

2.3.1.3.   PS cores HL-28 and PS-PBCA core-shell nanoparticles HL-29

HL-28 was synthesized analogous to HL-22; HL-29 was coated on HL-28 analogous to HL-23. In both preparations thioflavin T was replaced by thioflavin S.

2.3.1.4.   PS cores HL-30 and PS-PBCA core-shell nanoparticles HL-33

HL-30 was synthesized analogous to HL-22 using 5 mg of thioflavin T; HL-33 was coated on HL-30 with additional 5 mg thioflavin T as well.

2.3.1.5.   PS cores HL-31 and PS-PBCA core-shell nanoparticles HL-32

HL-31 was synthesized analogous to HL-22 without any dye; HL-33 was coated on HL-28 with additional 5 mg thioflavin T.

2.3.1.6.   PS core HL-49, PS-PBCA core-shell nanoparticles HL-50 and HL-50T

HL-49 and HL-50 were synthesized like HL-22 and HL-23, respectively. The surface of HL-50 was coated with polysorbate 80[231] and the coated nanoparticle was named HL-50T.

2.3.1.7.   Polymethacrylate nanoparticles HL-35 up to HL-42

176 ml of ultra-pure water were mixed with 4 ml of absolute ethanol, 140 mg sodium tetraborate, 200 mg carbowax 6000, 500 mg sodium dodecyl sulfate and 500 mg sodium dodecyl sulphopropyl maleate. Furthermore, different mixtures of methacrylic acid (MAA), methylmethacrylate (MMA), hydroxyethylmethacrylate (HEMA) and 2,3-epoxypropylmethacrylate (EPMA) as well as thioflavin T (see table 4). The reaction was started routinely by adding 100 mg potassium peroxidisulfate in 20 ml ultra-pure water and stirred overnight at 350 min^{-1} at 60°C.

Table 4: Monomer and dye composition of HL-35 up to HL-42 (abbreviations see above)

name	monomers	thioflavin T content
HL-35	4 g EPMA, 0.5 g MAA	10 mg
HL-36	4 g EPMA, 0.5 g MAA	20 mg
HL-37	4 g EPMA, 0.5 g MAA	30 mg
HL-38	4 g EPMA, 0.5 g MAA	45 mg
HL-39	2 g EPMA, 2 g MAA	10 mg
HL-40	1 g EPMA, 3 g MAA	10 mg
HL-41	0.5 g EPMA, 0.5 g HEMA, 3 g MMA	10 mg
HL-42	3.5 g MMA, 0.5 g MAA	10 mg

2.3.1.8. Core-shell nanoparticles RB-FIX2-PBCA-TF and RB-FIX3-PBCA-TF

The cores of both nanoparticles were synthesized with 10.8 g styrene in 196 ml ultra-pure water. Red fluorescent rhodamine B was added, which is bound covalently to 1 g or 0.5 g epoxypropylmethacrylate or RB-FIX2-PBCA-TF and RB-FIX3-PBCA-TF, respectively. After dialysis, the particles shells were made analogous to HL-23 with thioflavin T as dye.

2.3.1.9. PS-PBCA core-shell nanoparticle with perdeuterated polystyrene

To achieve a different neutron scattering length density between nanoparticle core and shell for SANS experiments, these particles synthesized like HL-22 and HL-23, but the cores are made of perdeuterated styrene. The particles were named HL-51 (core) and HL-52 (core-shell particle).

2.3.1.10. Polymethacrylate nanoparticles 2003/I-SA and 2003/I-SA/ApoE

The nanoparticle 2003/I was synthesized analogous to HL-35 and streptavidin was coupled to the nanoparticle. Therefore, 5 mg 1-ethyl-3-(3-dimethylaminopropyl)-carbodiimide 10 ml to an 1.1% suspension, 10 µmol streptavidin was added under stirring. After 4 h the solution was dialyzed for at least five times. A biotinylated ApoE dipeptide (ApoE $(141-150)_2$, Ac-LRKLR KRLLR LRKLR KRLLR-NH_2) was incubated overnight with the particle suspension (0.2 mg in 20 ml)[119].

2.3.2. Animal experiments

All animal experiments were performed at the University of Leipzig and approved by the Animal Care and Use Committee of the University of Leipzig (TVV 9/04).

2.3.2.1. Intrahippocampal and intracerebroventricular nanoparticle application

Animals were anesthetized with an intraperitoneal injection of etomidate (Hypnomidate; 33 mg/g body weight). In addition, local anesthesia at the skull was achieved with a subcutaneous injection of 1% lidocaine hydrochloride (Xylocitin). Next, their heads were mounted in a stereotaxic frame (Stoelting, Wood Dale, IL, USA). Thereafter, 1–2 µl of a nanoparticles suspension or the free thioflavins (2 mg/ml) were injected into the dorsal hippocampus (AP = #1.7 mm, L = 1 mm,

DV = 2 mm, relative to bregma). Intracerebroventricular (i.c.v.) injections were done with 5 µl of selected substances.

2.3.2.2. Intravenous nanoparticle application

Mice were anesthetized with an intraperitoneal injection of etomidate (Hypnomidate; 33 mg/g body weight). 10 - 20 µl of nanoparticles were injected into the tail vein.

2.3.2.3. Collecting mouse organs, fixation, storage and sectioning

Three days post-injection, the mice were transcardially perfused with 4% paraformaldehyde and 0.1% glutaraldehyde in 0.1 M sodium phosphate buffer, pH 7.4. Brains were post-fixed in 4% paraformaldehyde overnight and subsequently cryoprotected in 30% sucrose in phosphate buffer. Liver, lung, heart, kidneys and spleen of mice received intravenous nanoparticle application were cryoprotected in 30% sucrose in phosphate buffer. Frozen sections were cut at a thickness of 30 µm with a freezing microtome and collected in 0.1 M Tris-buffered saline, pH 7.4, (TBS) containing sodium azide.

2.3.3. Histochemistry and immunohistochemistry

2.3.3.1. Histochemical detection of thioflavins

For the analysis of fibrillar Aβ labeled with thioflavins *in vivo*, sections were washed with TBS, dipped in distilled water, mounted onto fluorescence-free glass slides, air-dried and coverslipped with Entellan or glycerol/gelatin.

2.3.3.2. Histochemical detection of *Solanum tuberosum* lectin

For the detection endothelial cells free-floating sections were blocked with 5% normal goat serum in TBS containing 0.3% Triton X-100 for at least 1 h. Next, the sections were incubated overnight at room temperature with 20 µg/ml biotinylated *Solanum tuberosum* lectin in the blocking solution. After thorough rinsing in TBS, the sections were reacted with Cy3- or Cy5-streptavidin (10 µg/ml or 20 µg/ml in TBS containing 2% bovine serum albumin, respectively) for 1 h, rinsed and processed as above.

2.3.3.3.   Immunohistochemical detection of β-amyloid

For the concomitant detection of thioflavins and immunostained β-amyloid, free-floating sections were processed with a rabbit antiserum directed against a central amino acid sequence of β-amyloid (SA 720 or SA 721). First, the tissue was blocked with 5% normal goat serum in TBS containing 0.3% Triton X-100 for at least 1 h. Next, the sections were incubated with rabbit anti-β-amyloid (1:1500 in the blocking solution) overnight. After thorough rinsing in TBS, the sections were reacted with Cy3-conjugated goat anti-rabbit IgG (20 µg/ml in TBS containing 2% bovine serum albumin) for 1 h. Finally, the sections were rinsed and processed as above.

2.3.3.4.   Histological controls

Histological controls were carried out by omitting the primary antibodies resulting in the absence of any red fluorescent immunosignal.

2.3.3.5.   Quenching of autofluorescence

To quench autofluorescence of the tissue, some sections were treated with Sudan Black B[232], mounted and coverslipped in glycerol/gelatin.

2.3.4. Photoconversion for electron microscopy

Fluorescence-labeled tissue sections were incubated in a solution consisting of 1.5% DAB and 1.5% potassium cyanide in 0.1 M PBS pH 7.4 for 30 minutes. Subsequently, the tissue was placed on a wet filter paper in a closed conversion chamber[233] and again incubated in the DAB solution. After the solution was sucked off with a pipette, the chamber was closed and filled with oxygen. Fluorescently labeled structures were illuminated with a 20x long distance objective of a Zeiss Axiophot microscope with a HBO-100W lamp until the fluorescence has faded. Thereafter, the sections were washed three times for 15 minutes in cold buffer and transferred into 1% buffered osmium tetroxide solution for 10-15 minutes. The sections were dehydrated in ascending series of ethanol, including blockstaining with uranyl acetate. For ultrathin sectioning the tissue was embedded in Durcupan.

2.3.5. Thrombin generation assay

Fresh drawn citrate blood was centrifuged for 10 minutes at 170 g to obtain platelet-rich plasma. Platelet-poor plasma (PPP) was prepared by double centrifugation of platelet-rich plasma at 2860 g each time for 20 minutes. The nanoparticles were diluted 1:20 in PPP or PRP, respectively.

The fluorogenic substrate used for thrombin generation was Z-Gly-Gly-Arg-aminomethylcoumarin at a concentration of 0.24 mM. It has a low affinity to thrombin and is consumed slowly. This avoids a premature plateau of the fluorescence curve due to substrate depletion. The start reagent with the fluorogenic substrate also contains dimethyl sulfoxide (diluted 1:21), isotonic saline (0.3 g/l), $CaCl_2$ (16 mM), tris puffer (pH 7.4, diluted 1:10), as well as an exogenous and an endogenous activator (tissue factor and pathromtin SL, respectively, each at a dilution of 1:1250).

25 µl of the reagent was added to 100 µl of PRP or PPP. Fluorescence intensity was detected using the Fluoroscan Ascent 2.2 at wavelengths of 340 nm (excitation wave length) and 440 nm (emission wavelength). The measurement lasted 120 minutes and ETP was given as arbitrary units of fluorescent activity (FU), the maximum reaction velocity as FU s^{-1}.

2.3.6. Platelet activation by flow cytometry

Blood was drawn using a 21-gauge needle into 5 ml syringes containing 3.8% sodium citrate and incubated with nanoparticle suspension (dilution 1:20) at 37°C for 30 minutes. Thereafter, blood was diluted 1:10 in HBSS with 1% BSA (total volume 500 µl), the nanoparticles were added to a final dilution of 1:20. Aliquots of the platelet suspension were activated for 10 minutes with ADP (final concentration 5µM) or TRAP-6 (10µM); native non-activated whole blood from the same sample served as control. The aliquots were incubated at 37°C with saturating concentrations of a murine PE-labeled anti-GPIIb/IIIa (CD41) monoclonal antibody and a murine FITC-labeled anti-GMP 140 (CD62P) monoclonal antibody. Platelet activation and staining were stopped after 5 minutes by adding 2 ml of 4°C HBSS buffer.

The activation of platelets was determined by flow cytometry. Platelet fragments as well as aggregates were excluded by gating platelets in the forward scatter signal. CD41-negative cells were excluded by a discriminator. Platelet activation was determined by the intensity of the CD62P expression.

3. Results

3.1. Physical properties of nanoparticles

3.1.1. Absorbance spectra of polymeric nanoparticles

For the PBCA nanoparticles HL-50 a linear relationship between absorbance and the inverse 4th power of the wavelength was found (fig. 28). The signal was superimposed by the absorbance from polystyrene and PBCA at about 350 nm and the dye thioflavin T at 420 nm but the spectrum was dominated by RAYLEIGH scattering.
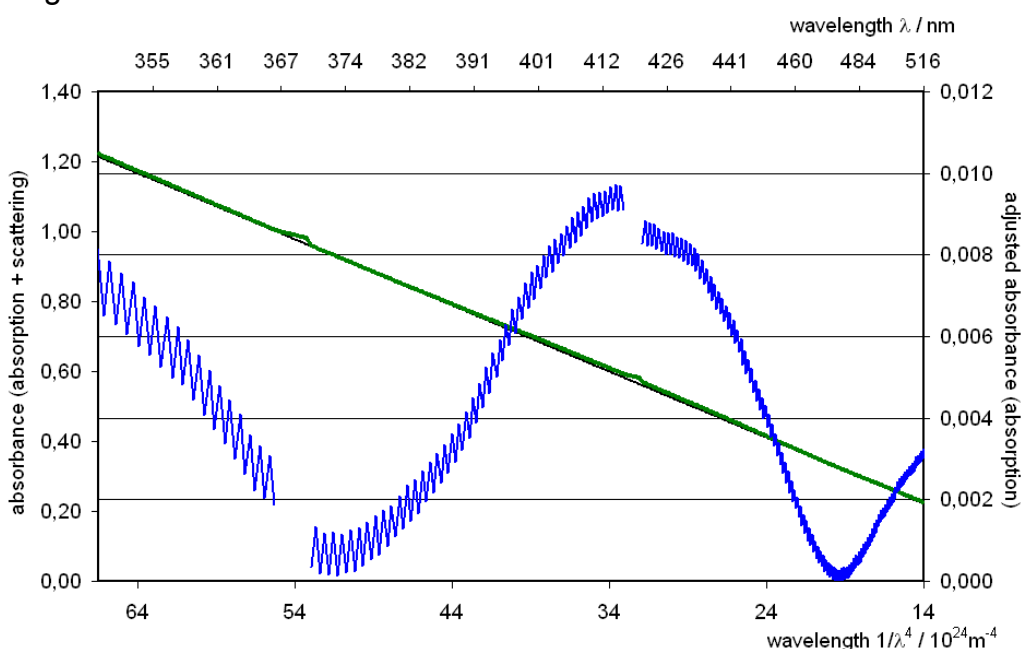
Figure 28: Absorbance spectrum of HL-50 (3 g/l); the absorbance (green dots) closely follows a inverse 4th power law with respect to the wavelength, which is composed of RAYLEIGH scattering (black line) and absorption (blue line); absorption is caused by the polymers (PS and PBCA, ~350 nm) and Thioflavin T (~420 nm), the fluctuations are caused by discrete steps of the signal intensity, the gaps are caused by changing mirrors in the analyzer (Jasco V560 UV-VIS Spectrophotometer).

On the other hand, the spectra of the EPMA/MAA nanoparticles were superimposed by a significant absorbance of thioflavin T, besides this a linear relationship between absorbance and the inverse 4th power of the wavelength was observed (fig. 29). For the double-fluorescent particles RB-FIX2-TF-PBCA and RB-FIX3-TF-PBCA two absorbance peaks for the dyes were observed (fig. 29).
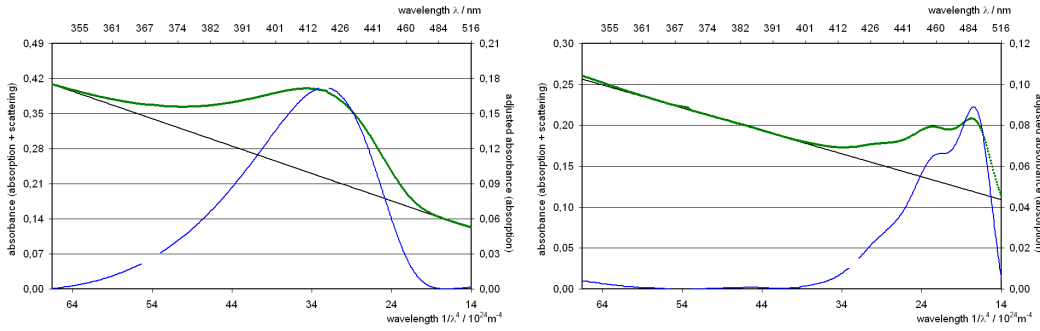
Figure 29: Absorbance spectra of polymeric nanoparticles. HL-35 (left, 3 g/l) and 2003/I-SA (right, 3 g/l); absorbance (green dots); RAYLEIGH scattering (black line) is superimposed by strong absorption of thioflavin T (left, blue line) or rhodamine B (right, blue line); Jasco V560 UV-VIS Spectrophotometer

For the EPMA/MAA nanoparticles an almost linear relationship between the slope of absorbance over the inverse 4th power of the wavelength was found (fig. 30).
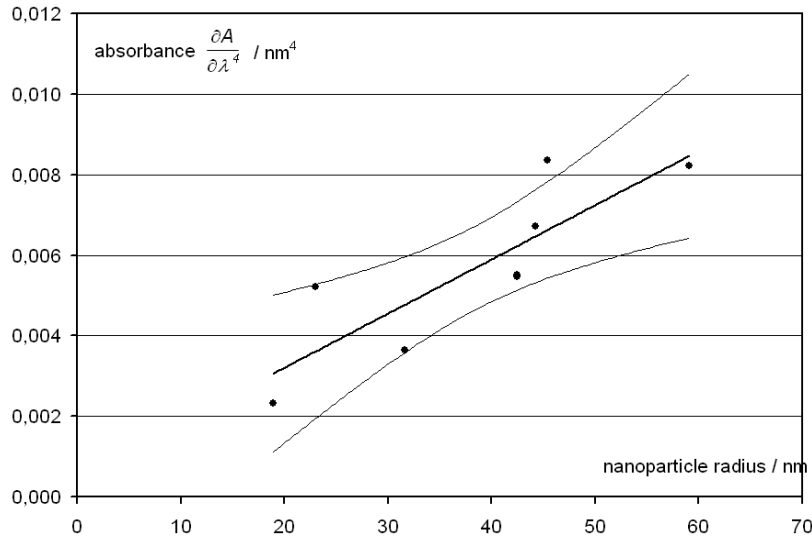
Figure 30: Relationship between nanoparticle radius (EPMA/MAA) and absorbance over the inverse 4th power of the wavelength

3.1.2. Degradation of nanoparticles observed by absorbance measurements

Degradation experiments were performed by incubating HL-50 and HL-50T with porcine liver esterase (fig. 31) at 37°C in a PBS buffered solution.

The change in the absorbance was measured at multiple wavelengths and was analyzed using a normalized absorption $A_n(t)$ given by

$$A_n(t) = \frac{A(t) - A_\infty}{A(0) - A_\infty} \ .$$

(63)

$A(t)$ is the absorption of the sample at time t, A_∞ is the asymptotic value of A for large t (here $t > 13$ h) and $A(0)$ is the initial absorption. The normalized absorption $A_n(t)$ is a measure for the degree of PBCA nanoparticle degradation.

The degradation lasted several hours. A relationship was found between reaction velocity and enzyme concentration. If the concentration of the nanoparticles was increased, the time until complete degradation was prolonged. Furthermore, the polysorbate 80-coating of HL-50T slowed down the reaction velocity (tab. 5).

The linear relationship between absorbance and the inverse 4th power of the wavelength was not affected during the measurements (data not shown).
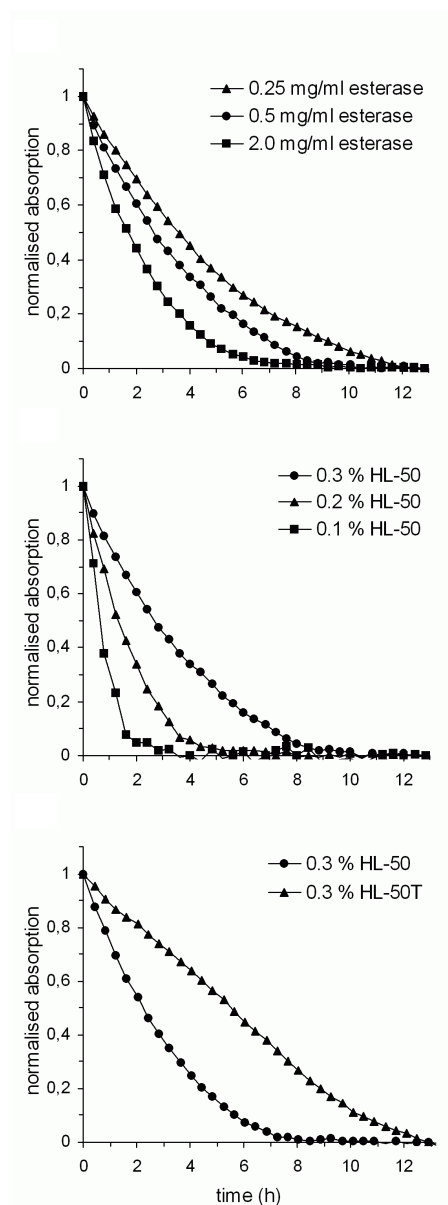
Figure 31: Enzymatic degradation of PBCA nanoparticles HL-50 with porcine liver esterase in vitro at 37°C. Spectrophotometric measurement of the time course of the normalized absorption $A_n(t)$ at 405 nm correlating with the degree of degradation. Only every 8th data point is shown as average value from at least three experiments. The standard deviation was found to be less than 5 % and is not shown.

(top) Degradation of HL-50 (3 g/l) with different porcine liver esterase concentrations.

(center) Degradation of different concentrations of HL-50 suspensions with 0.5 mg/ml esterase.

(bottom) Comparison between the degradation of HL-50 and polysorbate 80 coated HL-50T with 0.5 mg/ml esterase.

Table 5: Degradation of nanoparticles in dependence of particle and enzyme concentration and particle surface modification

Nanoparticle	Enzyme concentration	Half-life
HL-50 (3 g/l)	0.25 mg/ml	3.6 h
HL-50 (3 g/l)	0.5 mg/ml	2.8 h
HL-50 (3 g/l)	2.0 mg/ml	1.8 h
HL-50 (1 g/l)	0.5 mg/ml	0.7 h
HL-50 (2 g/l)	0.5 mg/ml	2.1 h
HL-50T (3 g/l)	0.5 mg/ml	5.6 h

3.1.3. Fluorescence spectra

Excitation-emission spectra of the nanoparticles were obtained. Thioflavin T-containing particles showed strong fluorescence (fig. 32) with a maximum at 419 nm (excitation) and 466 nm (emission).
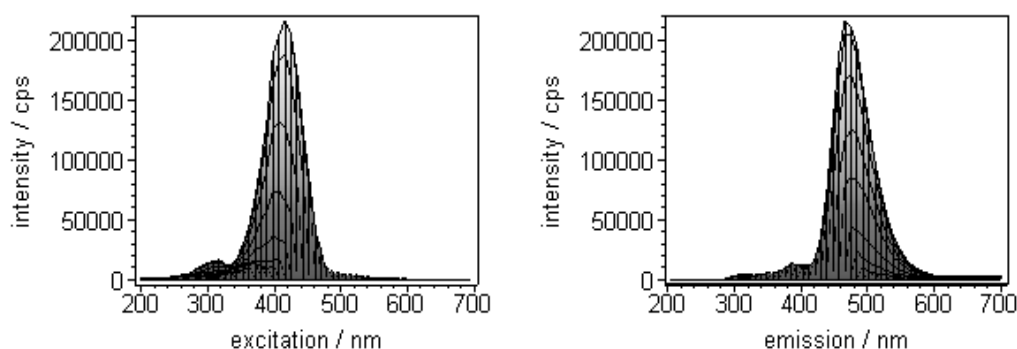
Figure 32: Excitation-emission spectrum of HL-50 (3 g/l)

The double-fluorescent particles RB-FIX2-TF-PBCA and RB-FIX3-TF-PBCA showed a trimodal spectrum (fig. 33) with the first peak at 419 nm and 466 nm (thioflavin T) and the second peak at 564 nm and 583 nm (rhodamine B). The third peak could be found at 419 nm (excitation) and 583 nm (emission) induced by Förster resonance energy transfer; energy was absorbed by thioflavin T, the light was emitted by rhodamine B.
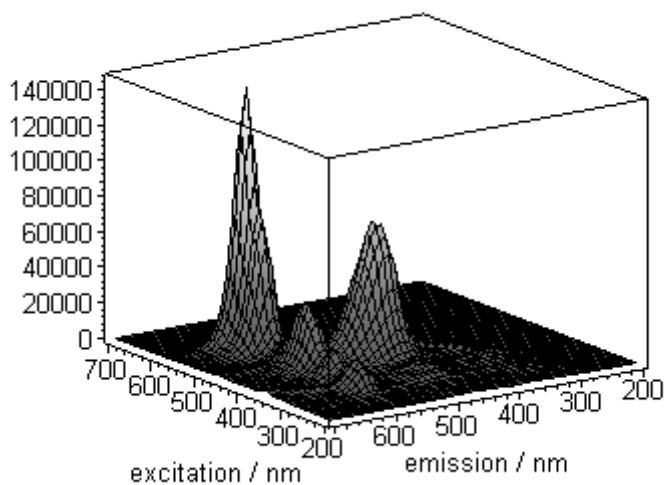
Figure 33: Excitation-emission spectrum of RB-FIX2-PBCA-TF (3.8 g/l)

3.2. Nanoparticle analysis by light scattering

3.2.1. Adjustment of the ALV/DLS-5000 compact goniometer system

A detailed description for the vat socket and vat adjustment is given by Steffen Lindert[219]. Thereafter, the focus lens is placed directly in front of the vat socket. The vat is filled with toluene, no sample is placed in the vat. Both horizontal and vertical micrometer gauge are used to adjust the focus lens. Goal of the adjustment is a high signal intensity and a low slope over the entire angle range. Angle dependent measurements were performed using different positions of the vertical and the horizontal micrometer gauge (fig. 34).
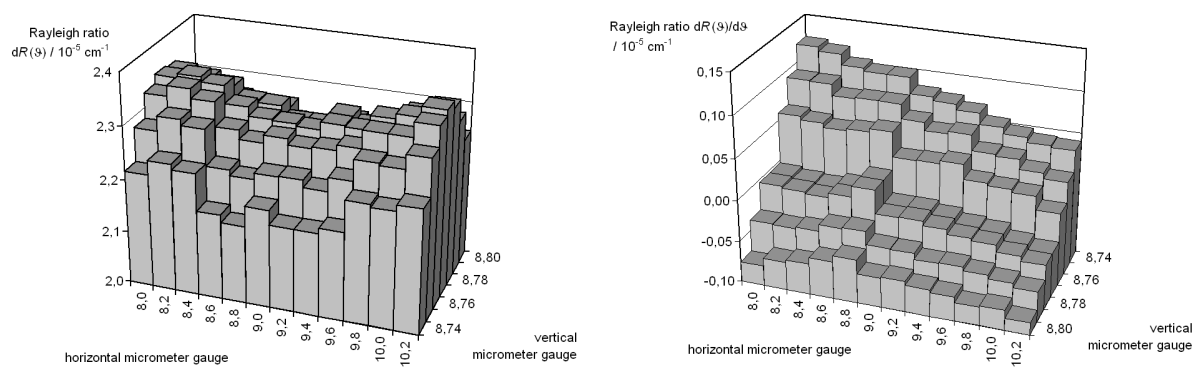
Figure 34: Focus lens adjustment, the final position was 9.00 mm (horizontal) and 8.77 mm (vertical)

No micrometer gauges are installed at the photomultiplier unit. Using the same instrument setup, the horizontal and vertical adjustment screws of the photomultiplier were loosen. Measurements were done with by a clockwise quarter-turn of the adjustment screws below the photomultiplier and on one side. The opposite screws were loosen before and tighten after the adjustment (fig. 35). .
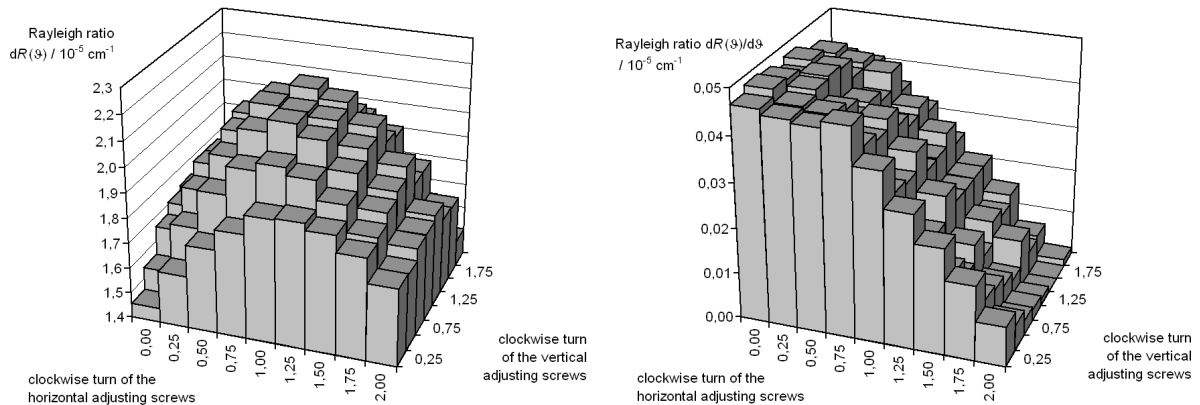
Figure 35: Photomultiplier adjustment, final position was 1 turn (horizontal) and 1.25 (vertical)

3.2.2. Determination of nanoparticle radii by light scattering

For the determination of nanoparticle radii the original solutions must be diluted to give an adequate intensity but avoid multiple scattering processes by high particle content. Using dynamic light scattering, low standard deviation between measurements and low angle dependency were found between particle concentrations of 3.75 and 12.5 mg/ml (fig. 36).
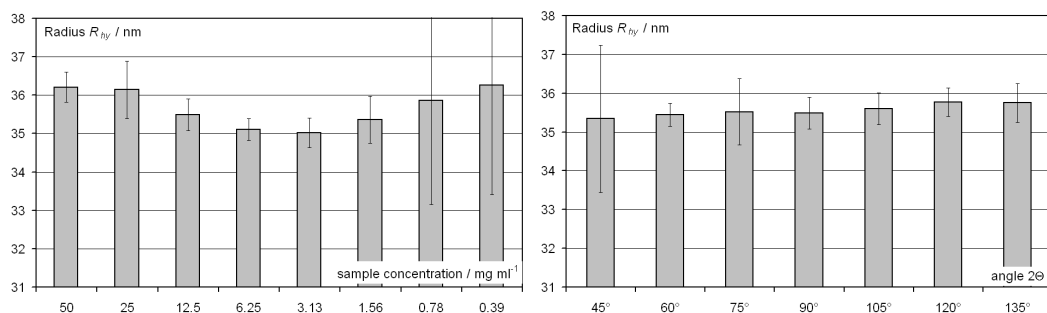
Figure 36: Hydrodynamic radius of nanoparticles HL-22 depending on particle concentration (left) and scattering angle (right). The radii are calculated by a "Simple fit" using the ALV software from dynamic light scattering data.

The concentration-dependent data can be further used in a Guinier plot (see eqn. 38), where the Rayleigh ratio $\ln\left(Kc/R_\vartheta\right)$ is plotted against $q^2+\beta\cdot c$ (fig. 37). For each concentration the slope is determined by $f(q^2)\overset{!}{=}A+B\cdot q^2$, and the radius of gyration can be determined by $R_G=\sqrt{3\,B}$ (tab. 6).
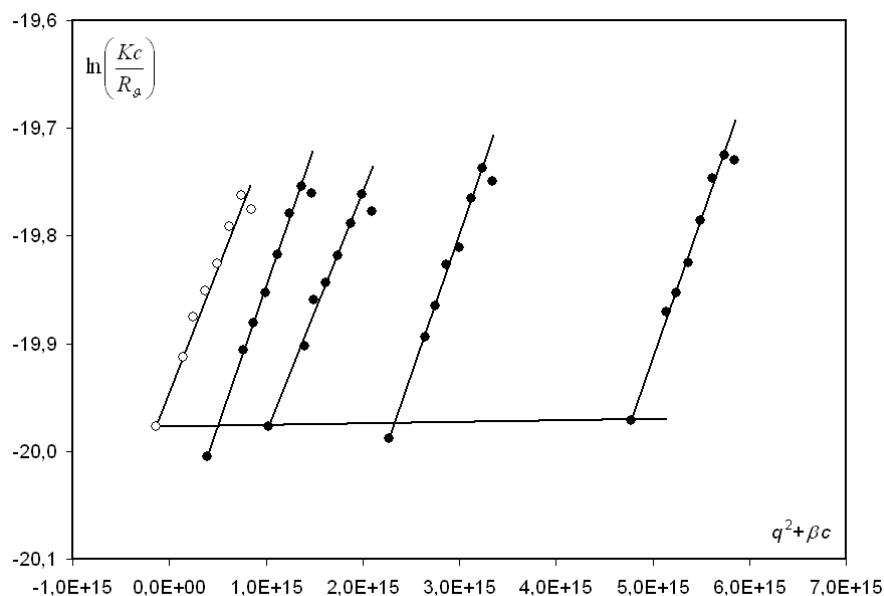
Figure 37: Guinier plot of polystyrene core HL-22 ($\beta=10^{17}$)

The molar mass and the second virial coefficient A_2 (see equation 38) can be determined by double extrapolation to $c=0$ and $\vartheta=0$ only if the refractive index increment of sample is known. The refractive index increment could not be determined for the nanoparticles due to a lack of reliable data. The radius of gyration R_G of a sphere is connected to its real radius R by $R^2=5/3\cdot R_G^2$.

Table 6: Radius determination by static (radius of gyration R_G) and static light scattering (hydro-dynamic radius R_{hy}) for polymeric particles, all radii in nm

Concentration	R_G (HL-22)	R_{hy} (HL-22)	R_G (HL-23)	R_{hy} (HL-23)	R_G (HL-31)	R_{hy} (HL-31)
50 mg/l	26.1	36.2 ± 0.2			30.7	41.1 ± 0.4
25 mg/l	25.9	36.0 ± 0.1			30.9	41.0 ± 0.5
12.5 mg/l	23.7	35.5 ± 0.2			31.3	40.8 ± 0.3
10 mg/l			55.9	67.5 ± 2.8		
6.3 mg/l	26.2	35.2 ± 0.2			30.6	40.4 ± 0.2
3.1 mg/l	27.7	35.0 ± 0.2			31.5	40.7 ± 0.3
Average	25.9 ± 1.4	35.6 ± 0.5	55.9	67.5 ± 2.8	31.0 ± 0.4	40.8 ± 0.3
Radius R	33.8 ± 1.8		72.2		40.0 ± 0.5	

The nanoparticle type HL-50 was compared with HL-50T, which was coated with polysorbate 80 to increase biocompatibility; hydrodynamic radii were determined with 49.6±3.4 nm and 50.1±2.6 nm, respectively. The coating can be estimated with a thickness of 0.5 nm.

3.2.3. Monitoring of nanoparticle degradation

Degradation of core-shell nanoparticles was monitored using light scattering. Therefore, 2 g/l of the nanoparticle suspension were incubated with 0.5 mg/ml of porcine liver esterase at 37°C. At defined time points between 30 minutes and 24 hours a 50 µl aliquot of the suspension was diluted in 9950 µl PBS buffer at 4°C to stop the ongoing reaction. Samples were measured using static light scattering (fig. 38). Unexpectedly, the particle radii increased (HL-50) or stayed nearly unchanged (HL-52). Data from dynamic light scattering were not analyzable, but indicate larger aggregates.
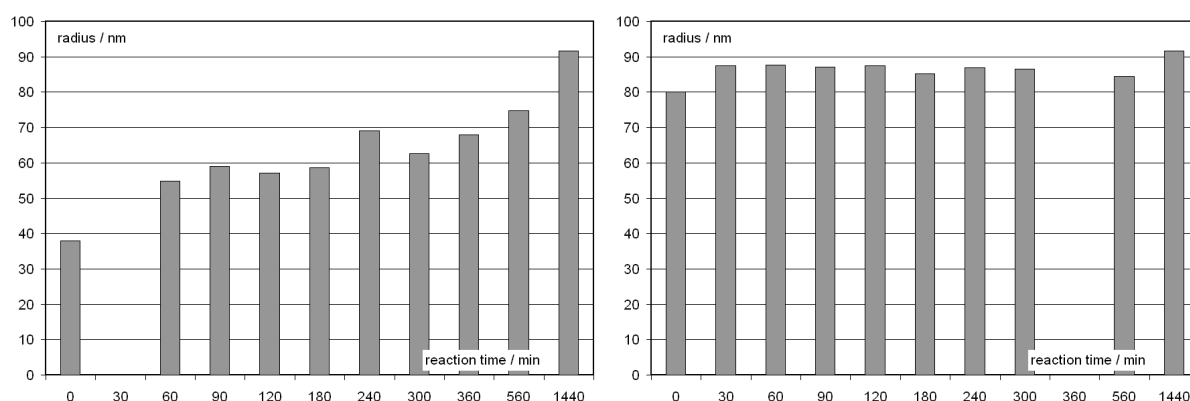
Figure 38: Degradation of polymeric core-shell nanoparticles (right: HL-50, left: HL-52) monitored using static light scattering. The increase of radii may be explained by aggregated core particles

The aggregation may be induced by the neutralization of the negative charges of the polystyrene particles. Hence, polystyrene nanoparticles HL-31 were mixed with various amounts of the positively charged thioflavin T and revealed concentration-dependent aggregation between 100 and 2000 µmol thioflavin T per gram nanoparticles.
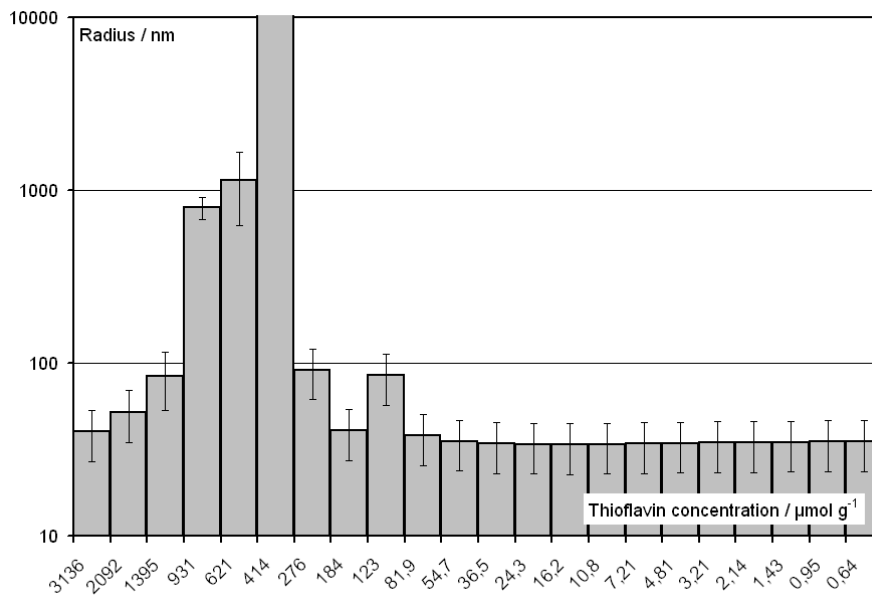
Figure 39: Polystyrene nanoparticles HL-31 showed concentration-dependent aggregation when mixed with thioflavin T (dynamic light scattering data).

3.3. Nanoparticle analysis by small angle neutron scattering

If not noted otherwise, nanoparticles were investigated at a concentration of 2 g/l. Data correction were performed by provided or self-written software.

3.3.1. Radius determination

Nanoparticle radii could be estimated using the GUINIER law; for low values of q the radius of gyration can be calculated from the slope of $\ln(I(q))$ over q^2 (fig. 40).
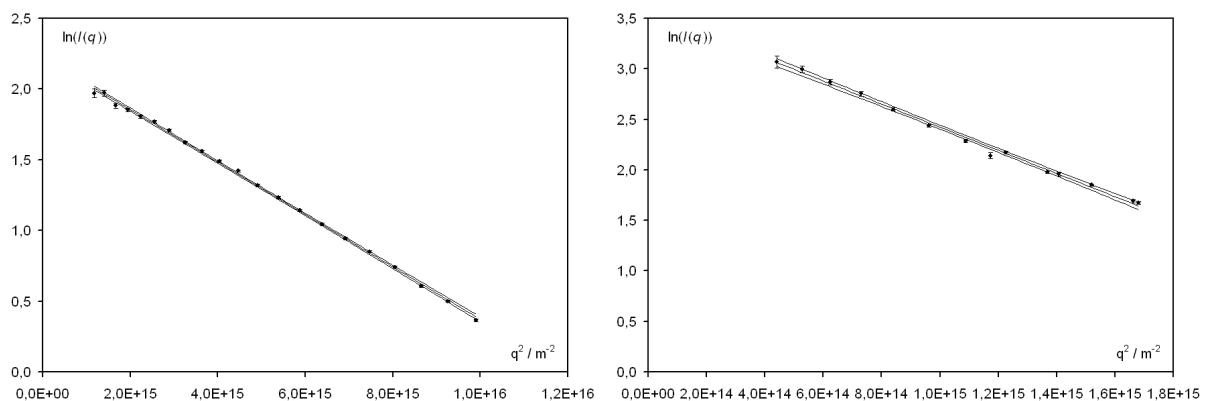
Figure 40: Radius determination by small angle neutron scattering using GUINIER law: D8-polystyrene core HL-51 (left) and core-shell particle HL-52 (right); slope and 99% confidence interval. Measured at spectrometer V4, BENSC, Berlin

A list of determined nanoparticle radii is given in table 7.

Table 7: Radius determination by small angle neutron scattering using GUINIER law

| Particle | radius of gyration R_G / nm | | | | | | Device |
	$X(D_2O)=0.0$	$X(D_2O)=0.1$	$X(D_2O)=0.3$	$X(D_2O)=0.5$	$X(D_2O)=0.8$	$X(D_2O)=0.95$	
HL-22	27.3	27.3		27.4	26.8	27.1	YuMO
HL-31	31.4	31.6		31.3	30.4	31.1	YuMO
HL-49	29.9						YelSub
HL-50	39.2						YelSub
HL-51	21.5				21.5		YuMO
HL-51	23.6						V4
HL-52	58.6		52.4		59.5	61.1	V4
2003/I-SA	19.3	20.0		28.7	12.4		YelSub

Devices: "YuMO" - SANS spectrometer YuMO, JINR, Dubna; "YelSub" - SANS spectrometer "Yellow submarine", BNC, Budapest and "V4" - SANS spectrometer V4, BENSC, Berlin

3.3.2. Contrast variation

Contrast variation experiments were used to determine the particle contrast. The achieved data were compared to theoretical values; if the measured contrast equals the estimated contrast a homogeneous particle can be assumed. $\sqrt{I(0)/c}$, extrapolated from the GUINIER plot, is plotted over the solvent contrast, usually $X(D_2O)$; to simplify the data analysis, values above the estimated particle contrast are multiplied with -1 and the interception with the X-axis is calculated (fig. 41).
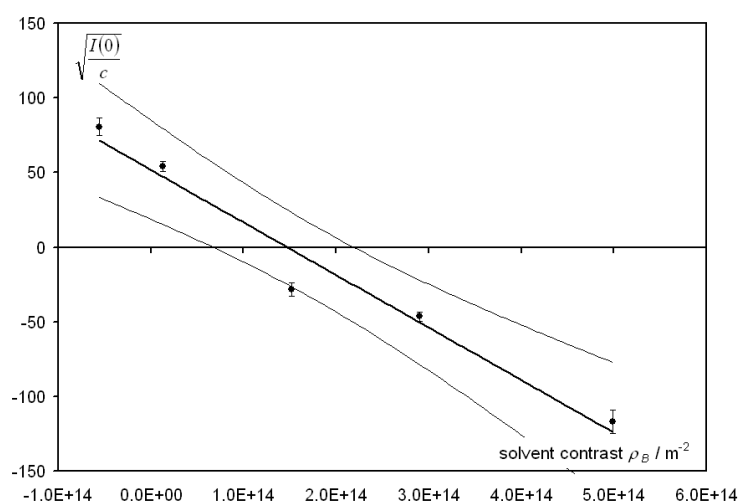
Figure 41: Determination of sample contrast using contrast variation; EPMA/MAA nanoparticle 2003/I-SA, Measured at "Yellow submarine", BNC, Budapest

Table 8 shows sample contrasts determined for various polymers. For all used polymers, the measured and the theoretical sample contrast were found to be equal, which indicates homogeneity of the particles. For the core-shell nanoparticles HL-52 a "virtual" sample contrast is given; the result is closer to PBCA, which underlines the larger amount of PBCA compared to perdeuterated polystyrene in the particle.

Table 8: Sample contrast determined by contrast

Nanoparticle		Sample contrast		
	Monomer	ρ_S / $10^{14}m^{-2}$	$X(D_2O)$	Device
HL-22	PS	1.36 ± 0.22	0.28 ± 0.04	YuMO
HL-31	PS	1.40 ± 0.24	0.28 ± 0.03	YuMO
HL-51	D8-PS	6.29 ± 0.57	0.99 ± 0.08	YuMO
HL-52	D8-PS/PBCA	2.54[†]	0.45[†]	V4
2003/I-SA	EPMA/MAA	1.47 ± 0.81	0.29 ± 0.11	YelSub

[†] An average is given of the D8-PS core and PBCA shell. Devices: "YuMO" - spectrometer YuMO, JINR, Dubna; "V4" - spectrometer V4, BENSC, Berlin; "YelSub" - spectrometer "Yellow submarine", BNC, Budapest. Monomers: PS - polystyrene, D8-PS - perdeuterated polystyrene, PBCA - poly(butyl cyanoacrylate), EPMA - 2,3-epoxypropylmethacrylate, MAA - methacrylic acid

3.3.3. Nanoparticle degradation

Core-shell nanoparticles were degraded using porcine liver carboxylesterase. To achieve stable enzyme activity the experiments were performed in 1:10 diluted HBSS buffer avoid aggregation of particles or degradation products. After adding of the enzyme to the nanoparticle suspension, the reaction batch was filled in a neutron scattering cuvette and placed in the sample holder, which was heated to 37°C.

This enzyme exhibits a neutron scattering length density of about $1.9 \cdot 10^{14}$ m^{-2}, which is close to the value for poly(butyl cyanoacrylate) with $1.45 \cdot 10^{14}$ m^{-2}. Due to the similar concentration of the nanoparticle and the enzyme (2 g/l), the scattering signal is superimposed by the enzyme. Therefore, the determination of particle radii may be distorted.

The nanoparticle type HL-50 displayed a reduction of the particle radius and decreasing scattering intensity (fig. 42). The radius of gyration felt from 28.5 nm to 18.3 nm, for a spherical particle these radii equal 36.8 nm and 23.7 nm, respectively. The former is lower than 50.6 nm, determined for HL-50, while the latter is lower than the 38.6 nm of the polystyrene core HL-49. The scattering intensity was decreased

by 92%, the half life is estimated with 1.7 hours. Data were recorded in intervals of five minutes, hence, the measured intensities exhibit high variation.
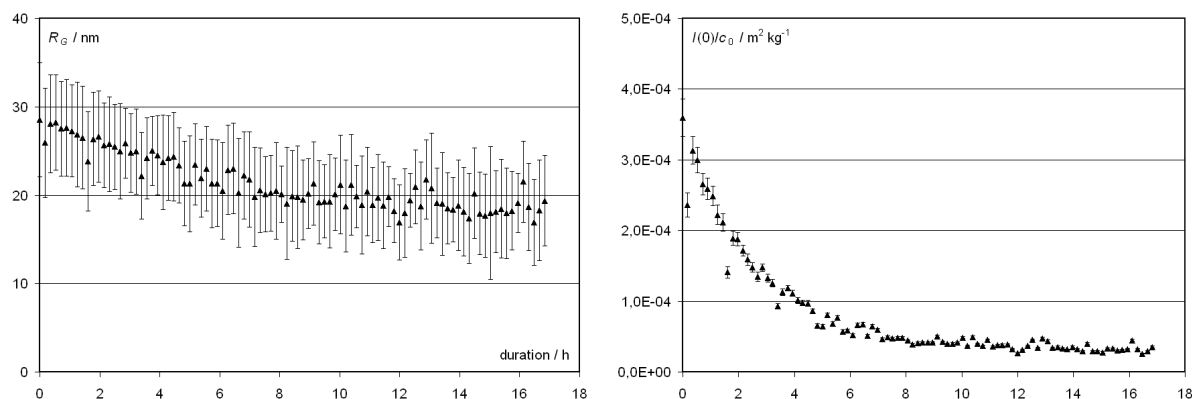
Figure 42: Degradation of nanoparticles HL-50 monitored by small-angle neutron scattering: reduction of the nanoparticle radius (left) and scattering intensity (right). HL-50 (polystyrene core and PBCA shell, 2 g/l) diluted in 1:10 HBSS buffer and porcine liver esterase (2 g/l) at 37°C. Measured at "Yellow submarine", BNC, Budapest.

Degradation of nanoparticles HL-52 consisting of a perdeuterated polystyrene core and a PBCA shell was observed with two different solvent contrasts. When the solvent matched the scattering length density of the shell, no alteration of the scattering was observed (fig. 43), the determined radius of gyration of about 26 nm nearly equals the 23.6 nm of the core particle HL-51. Using a contrast that almost
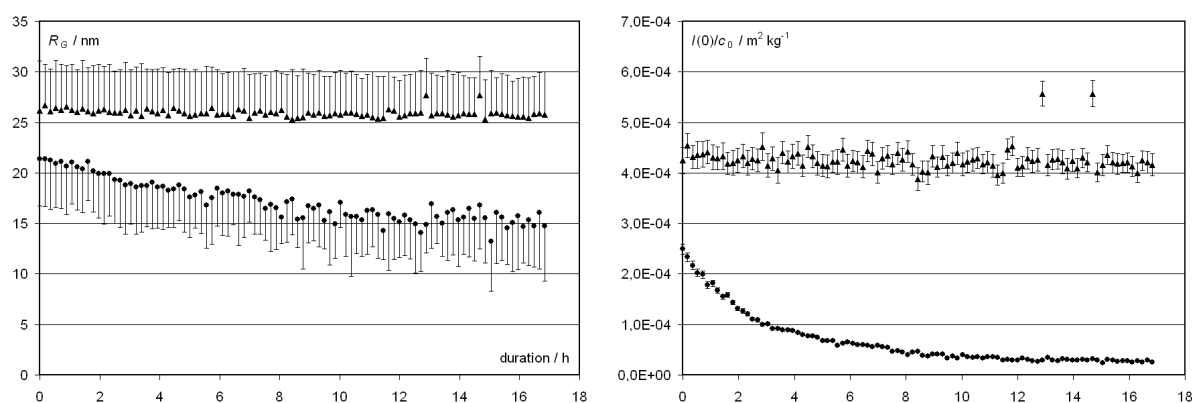
Figure 43: Degradation of nanoparticles HL-52 monitored by contrast variation and small-angle neutron scattering: reduction of the nanoparticle radius (left) and scattering intensity (right) if the solvent nearly matches the core neutron scattering length density ($X(D_2O)$=0.8, circles); unchanged particle radius and scattering intensity if the solvent matches the neutron scattering length density of the shell ($X(D_2O)$=0.3, triangles). HL-52 (perdeuterated polystyrene core and PBCA shell, 2 g/l) diluted in 1:10 HBSS buffer and porcine liver esterase (2 g/l) at 37°C. Measured at "Yellow submarine", BNC, Budapest.

matches the core (solvent $4.9 \cdot 10^{14}$ m^{-2}, D8-PS $6.3 \cdot 10^{14}$ m^{-2}) a clear degradation of the PBCA shell was observed; the radius of gyration felt from 22 nm to 15 nm. The particle radius of HL-52 was measured with 76 nm; whereas, the scattering intensity decreased by 90% and the half-live was determined with 1.9 hours.

In an alternative approach the nanoparticles HL-52 with a concentration of 10 g/l were degraded by porcine liver esterase (2 g/l) at 37°C in a 1:10 diluted HBSS buffer. At certain time points an aliquot was diluted 1+4 in 4°C cold buffer to stop the enzyme activity. Subsequently, the diluted samples were measured at 4°C for at least 1 hour; data were obtained for four different D_2O contents (fig. 44).
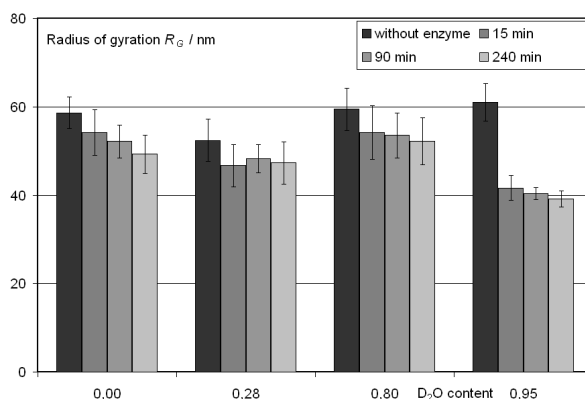
Figure 44: Degradation of nanoparticles HL-52 observed with different solvent contrasts; spectrometer V4, BENSC, Berlin

Particle degradation was found in all samples, but a complete degradation of the particle shell was not revealed. At the most, the gyration radius felt to 40 nm in the sample which matches the contrast of the core, about 16 nm larger than the radius of gyration of particle-core HL-51. Furthermore, the sample with an D_2O content of 0.28 did not match the shell contrast, proved by the large initial gyration radius of 52 nm, 12 nm more than HL-51. A "virtual" particle contrast was calculated, where the contrast of the shell equals the contrast of the core. It was revealed, that this "virtual" contrast increases with the degradation progress (fig. 45). This can be interpreted as a decreased amount of PBCA from the shell compared to the constant amount of perdeuterated polystyrene of the core.
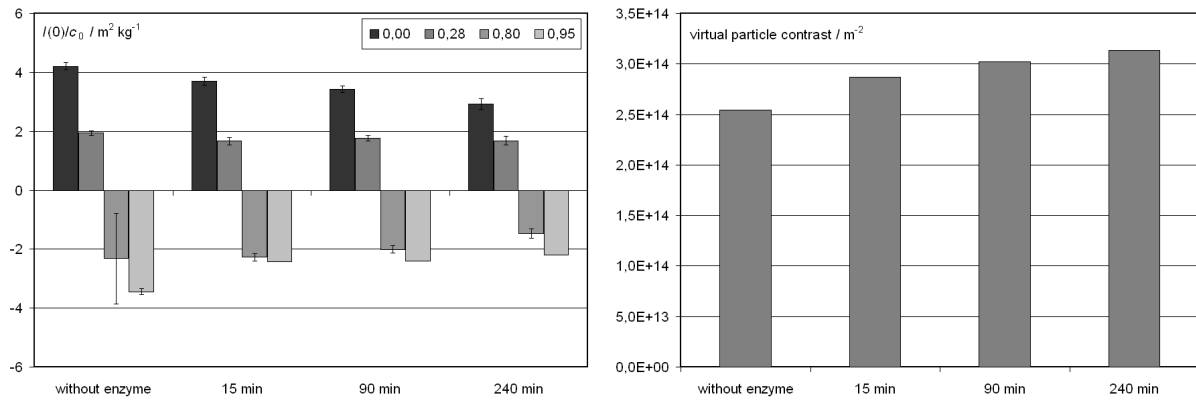
Figure 45: Degradation of nanoparticles HL-52 using contrast variation. To obtain a "virtual" particle contrast, scattering intensity for the both samples with high D_2O-content were multiplied with -1 (left) and the interceptions with the X-axis were determined (right). The data revealed an increasing portion of D8-polystyrene in the particle as a measure of shell degradation. Spectrometer V4, HMI, Berlin.

3.4. Fit models

Equation 59 can be solved analytically for both models. Besides the distribution of particle radii, the scattering vector q displays a high variability. This is caused by a GAUSSIAN distributed wavelength of the incident beam and the dimensions of sample and detectors. The error of q is estimated as GAUSSIAN distributed; the theoretical scattering intensity is calculated as a weighted average between $I(q-\alpha\cdot\sigma_q)$ and $I(q+\alpha\cdot\sigma_q)$ using $2\beta+1$ nodes. Due to the combined appearance of q and R in the numerator of equation 59 a higher variation of q is combined with a lower variation of R and *vice versa*[219]. Results were obtained for HL-22 (table 9) and HL-31 (table 10), both nanoparticles were assumed to be homogeneous with $d=0$ and $l=0$.

Table 9: Results from fitting model 1, nanoparticles HL-32, $\alpha=3$; measured at YuMO, JINR, Dubna

$X(D_2O)$	0.0		0.1		0.5		0.8		0.95	
β	1	12	1	12	1	12	1	12	1	12
Radius R_I / nm	29.2	33.5	28.1	32.2	29.2	33.9	27.5	33.1	28.4	33.4
σ_{R_I} / nm	4.6	1.6	4.7	3.2	4.9	1.9	5.7	2.0	5.2	1.8
R_G from R_I	25.9	26.3	25.3	26.5	26.2	26.8	26.2	26.2	26.1	26.4
R_G from Guinier plot	27.3		27.3		27.4		26.8		27.1	

Table 10: Results from fitting model 1, nanoparticles HL-31, $\alpha=3$; measured at YuMO, JINR, Dubna

$X(D_2O)$	0.0		0.1		0.5		0.8		0.95	
β	1	12	1	12	1	12	1	12	1	12
Radius R_I / nm	34.7	39.4	35.4	39.3	34.1	39.0	33.4	38.4	33.6	38.9
σ_{R_I} / nm	4.8	0.3	4.2	0.5	5.0	0.4	5.2	0.6	5.0	0.6
R_G from R_I	30.0	30.5	29.8	30.4	29.7	30.2	29.5	29.8	29.4	30.2
R_G from Guinier plot	31.4		31.6		31.3		30.4		31.1	

3.5. Animal experiments

3.5.1. Immunohistochemical detection of β-amyloid in mouse brain tissue

To prove the expression of β-amyloid in the applied APPSwe/PS1 mouse model, transgenic animals were tested. Both anti-β-amyloid antibodies, SA 720 and SA 721, revealed a typical pattern of a severe β-amyloidosis (fig. 46) within the whole brain tissue of the tested mice. The antibodies showed a high intensity of staining as well as a very low background. Furthermore, the cores of β-amyloid plaques exhibited stronger labeling than the peripheral deposits.
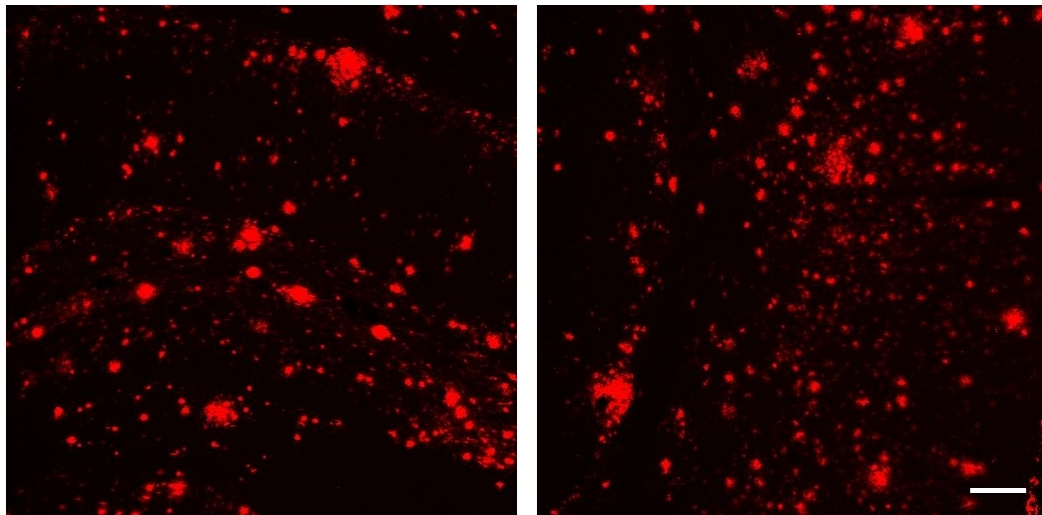
Figure 46: Immunohistochemical detection of β-amyloid in a 61 week-old female mouse (APPSwe/PS1A246E) using rabbit anti-β-amyloid SA 721, visualized with Cy3-goat-anti-rabbit; hippocampus (left), neocortex (right). Pictures were obtained by confocal laser-scanning microscopy (Zeiss LSM 510 Meta). Scale bar 100 µm

3.5.2. Histochemical detection of β-amyloid in mouse brain tissue

The use of the thioflavin T derivative BTA-2 was tested *in vitro*. The dye exhibits intensive staining of β-amyloid plaques, but also a high background (fig. 47).

BTA-2 is hardly soluble in water, therefore, DMSO and ethanol were added to increase solubility. These solvents may interfere with other staining and may damage nanoparticles. Thus, BTA-2 was not further used.
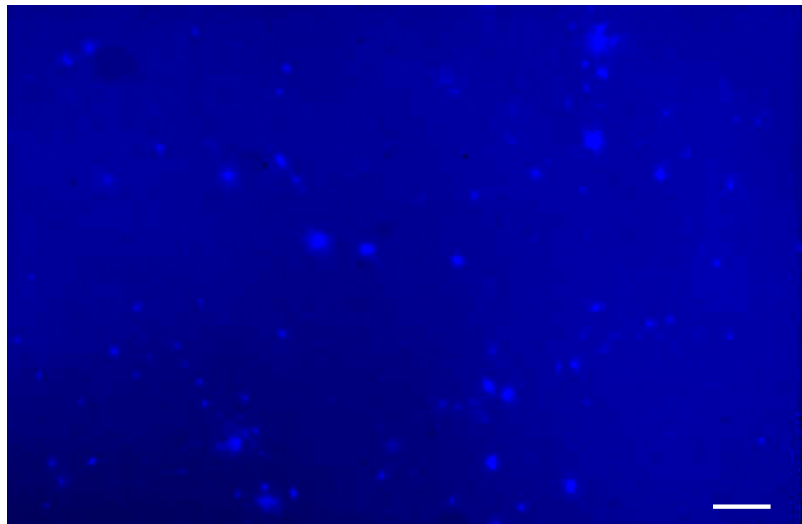
Figure 47: Histochemical detection of Aβ in a 60 week-old female mouse (APPSwe/PS1A246E) by BTA-2. Scale bar 100 µm

3.5.3. Intracerebral application of free thioflavin dyes

After intrahippocampal injection of thioflavin T the dye was found distributed over the entire hemisphere. Thioflavin T showed intensive labeling of β-amyloid containing plaques and, a low but significant background labeling (fig. 48).
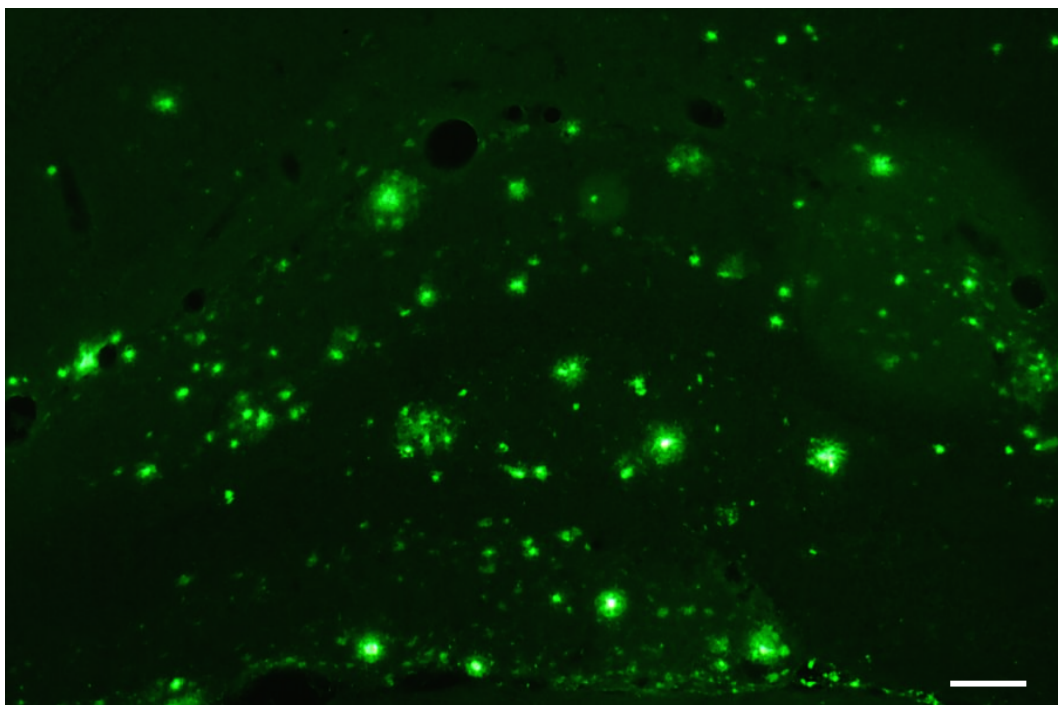
Figure 48: Intrahippocampal injection of thioflavin T in a 60 week-old female mouse (APPSwe/PS1A246E); the tissue was fixed three days after injection; hippocampal region. Picture was obtained by a Axioplan fluorescence microscope combined with a camera, exposure time 220s, gamma corrected (γ=0.5). Scale bar 100 µm

After injection of thioflavin S into one hemisphere (ipsilateral side), the labeling intensity in the other, contralateral, hemisphere was significantly diminished (fig. 49). Staining with the antibody SA 721 demonstrated homogeneous distribution of β-amyloid. Furthermore, it was observed, that the signal of thioflavin S correlates with the signal of the Aβ-specific antibody (fig. 49). No vascular β-amyloid was found.
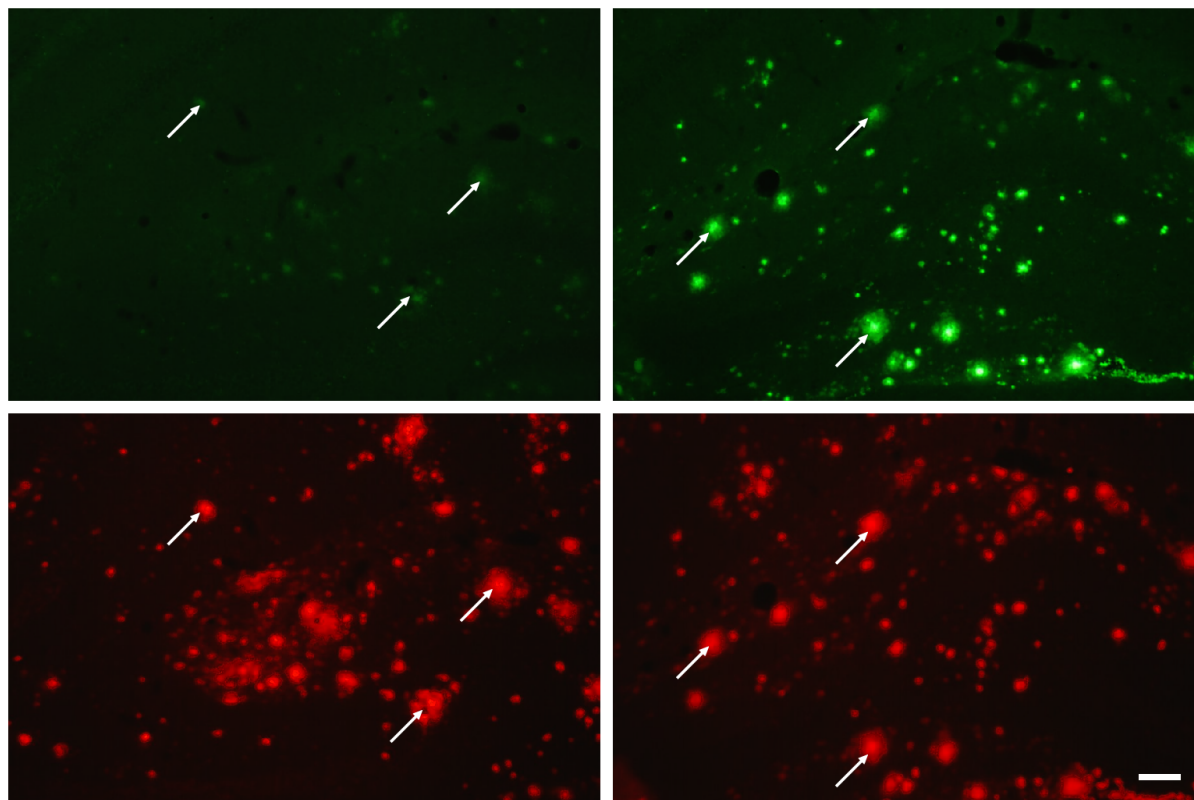
Figure 49: Double fluorescence labeling of senile plaques in the hippocampus of an aged transgenic mouse (60 weeks, female, APPSwe/PS1A246E). *In vivo* binding of thioflavin S to fibrillar β-amyloid three days after intrahippocampal dye injection combined with the Aβ-immunolabeling. Thioflavin staining *in vivo* (bottom). Indirect immunofluorescence labeling of β-amyloid deposits with rabbit anti-Aβ and red fluorescent Cy3-conjugated goat anti-mouse IgG (top). Contralateral hemisphere (left); ipsilateral side (injection site, right). Arrows indicate the co-localization of thioflavin S and Aβ immunoreactivity in selected plaques. Pictures were obtained with an Axioplan fluorescence microscope (Zeiss), gamma corrected (γ=0.5). Scale bar = 100 µm.

3.5.4. Intracerebroventricular application of nanoparticles

After intracerebroventricular injection of thioflavin S-filled nanoparticles (HL-29) a diminished staining of β-amyloid plaques was observed (fig. 50), compared to intrahippocampal application. Nevertheless, plaques were targeted by the released

dye in APPSwe/PS1 mice. Double staining with Aβ-specific antibodies revealed the selective binding of thioflavin S to β-amyloid (fig. 50). While the antibody marked the entire plaque, thioflavin S was found to be restricted to the core of plaque.
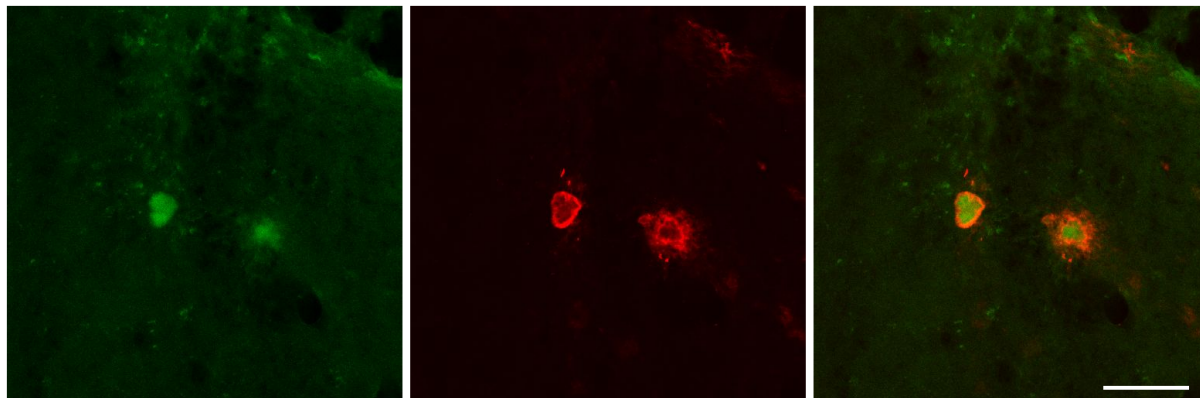
Figure 50: Hippocampal β-amyloid deposits in 53 week-old female mouse (APPSwe/PS1dE9) three days after intracerebroventricular injection of ThS-filled nanoparticles (HL-29). Thioflavin staining *in vivo* (left). Immunofluorescence labeling of Aβ deposits with rabbit anti-Aβ (SA 721) and Cy5-tagged goat anti-rabbit IgG (color-coded in red, center), merge (right). Confocal laser-scanning microscopy with a Zeiss LSM Meta 510. Scale bar 50 µm.

After intracerebroventricular application of RB-FIX3-PBCA-TF nanoparticles, the red fluorescent nanoparticle cores were found close to the application site. These particles exhibit no green fluorescence or FRET signal which proves the degradation of the PBCA shell (fig. 51). The nanoparticles were transported within the cerebro-spinal fluid and, therefore, found at the interface between tissue and fluid (fig. 52), but the particles are restricted to blood vessels and did not enter the tissue (fig. 53).
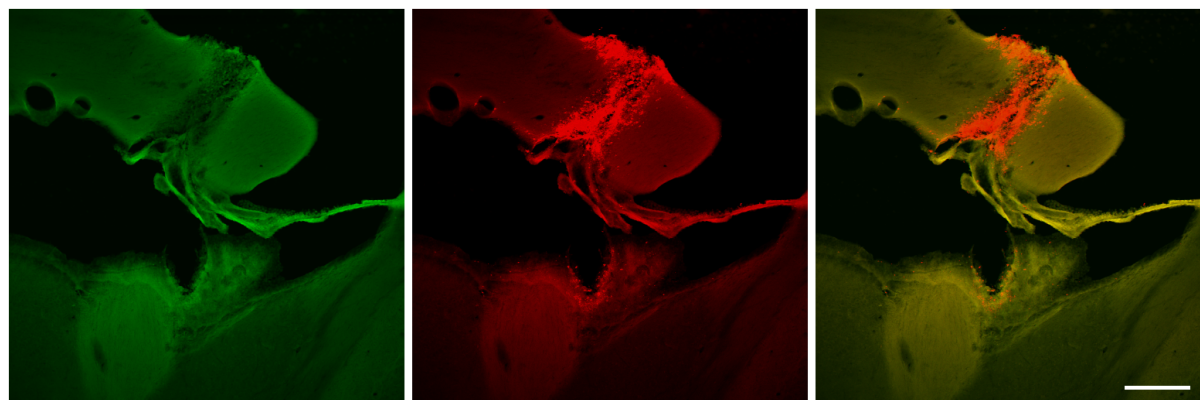
Figure 51: Intracerebroventricular application of core-shell nanoparticles in a 41 week-old male wild-type mouse; The green fluorescent shells are degraded (left). Undegradable, red fluorescent cores remain closely to the injection site (center); merge (right). Scale bar 250 µm
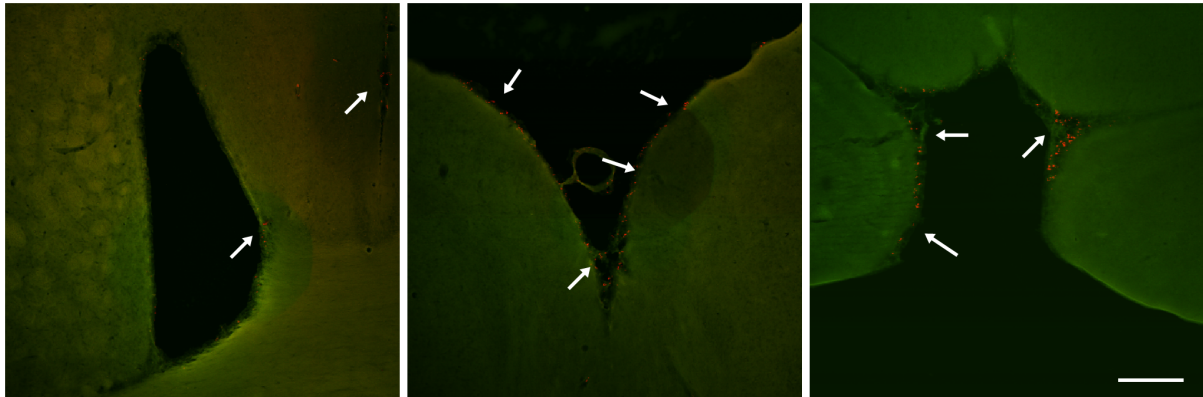
Figure 52: Intracerebroventricular application of core-shell nanoparticles in a 41 week-old male wild-type mouse; nanoparticles are transported by the cerebrospinal fluid; lateral ventricles and third ventricle (left); medial longitudinal fissure (center); fourth ventricle (right). Scale bar 500 μm
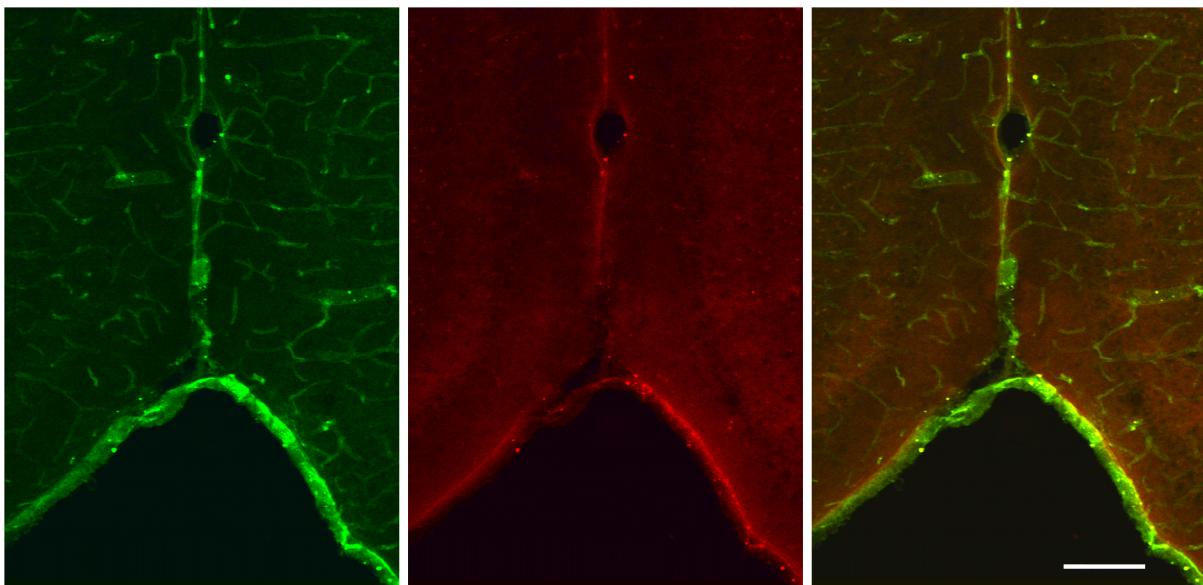
Figure 53: Nanoparticles are restricted to blood vessels after intracerebroventricular application in a 49 week-old female wild-type mouse; blood vessels stained with *Solanum tuberosum* lectin (left); red fluorescent nanoparticles (center); merge (right). Scale bar 250 μm

3.5.5. Intrahippocampal application of thioflavin-filled nanoparticles

After intrahippocampal injection of undegradable nanoparticles, the particles remained close to the injection site (fig. 54). No labeling of plaques was observed. After injection of thioflavin S-filled nanoparticles HL-29, targeting of β-amyloid could be detected (fig. 55). For the labeling of Aβ the dye has to be released from the

degradable nanoparticle. In one case the nanoparticles were found within neurons of the basal forebrain, possibly after their retrograde transport (fig. 54).
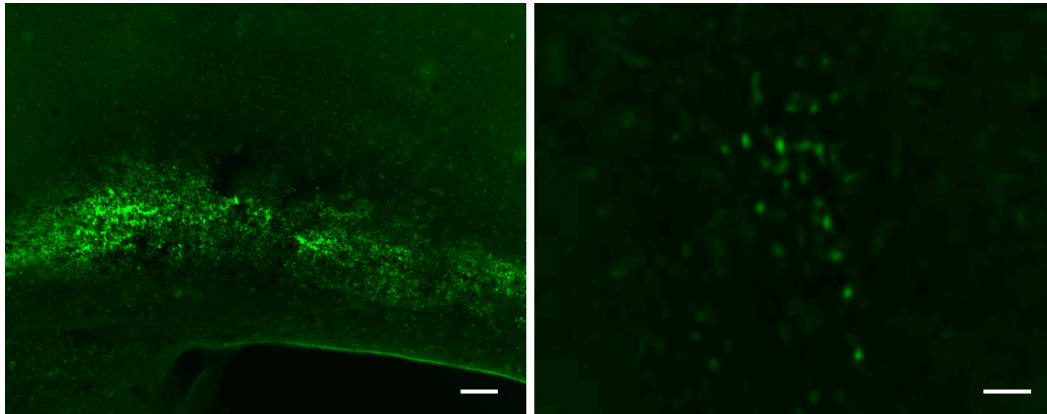
Figure 54: Intrahippocampal injection of undegradable EPMA/MAA nanoparticles (HL-38) in a female mouse (56 weeks, APPSwe/PS1dE). Left: Nanoparticles remain close to the injection site in murine hippocampus, β-amyloid plaques were found unmarked; scale bar 100 µm. Right: Nanoparticles transported within neurons are found in the basal forebrain. Scale bar 25 µm.

Thioflavin S was observed to bind β-pleated sheet structures in the core of matured plaques, which demonstrates highly ordered aggregates. The surrounding less aggregated β-amyloid molecules are stained clearly with the specific antibody but less with thioflavin S (fig. 55).
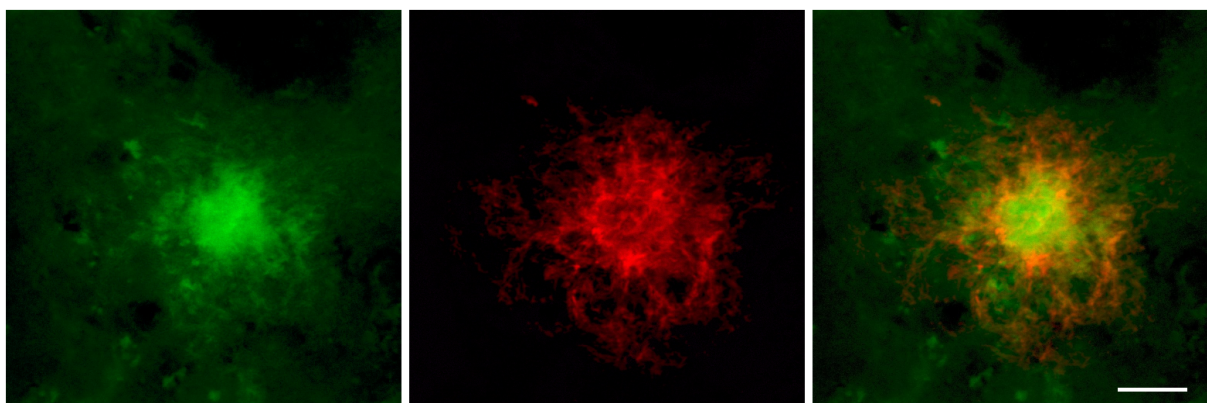
Figure 55: Hippocampal β-amyloid deposits in a 60 week-old female mouse (APPswe/PS1A246E) three days after intrahippocampal injection of thioflavin S-filled nanoparticles (HL-29). Thioflavin staining *in vivo* (left). Immunofluorescence labeling of Aβ deposits based on rabbit anti-Aβ (SA 721) and Cy3-conjugated goat anti-rabbit IgG (center). Merge (right). Note the restriction of the thioflavin staining to the β-pleated sheet structures in the core of the plaque. Confocal laser-scanning microscopy with TCS SP2 AOBS (Leica). Scale bar 10 µm.

3.5.6. Intracerebral application and detection of nanoparticle 2003/I-SA/ApoE

After intrahippocampal injection of 2003/I-SA/ApoE the nanoparticle could be detected by its fluorescence or by histochemical methods using free biotin binding sides (fig. 56). The particles showed a similar distribution within the brain like the core-shell nanoparticles after intracerebroventricular or intrahippocampal application.
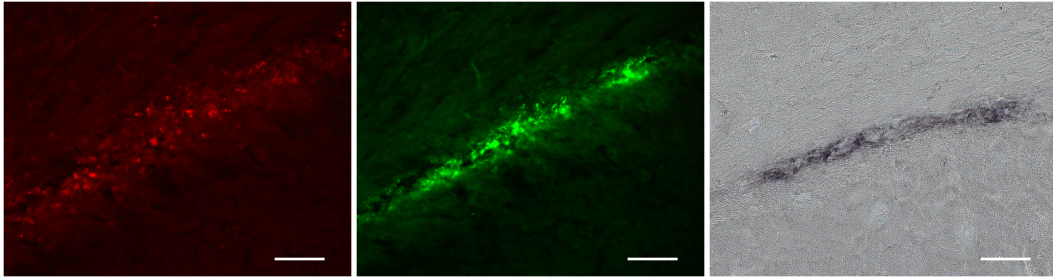
Figure 56: Detection of streptavidin-coated nanoparticle 2003/I-SA/ApoE in murine hippo-campus 24 hours after intra-hippocampal injection in a wild-type mouse. Direct detection of the red fluorescent nanoparticle (left), labeling with Cy-5-streptavidin (center, color-coded in green), labeling with biotinylated horseradish peroxidase and nickel-enhanced DAB (right). Scale bar 50 μm.

3.5.7. Detection of thioflavin T by electron microscopy

After intrahippocampal injection photoconverted thioflavin T was found binding to β-amyloid containing plaques (fig. 57 and 58). Furthermore, remnants of thioflavin T containing nanoparticles were found within phagosomes of microglia (fig. 59).
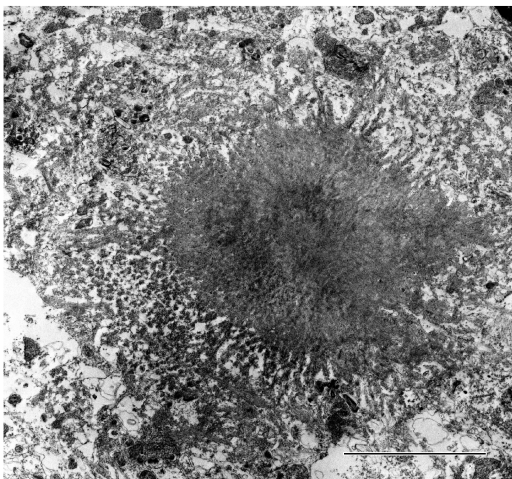
Figure 57: Binding of photoconverted thioflavin to a hippocampal β-amyloid-containing plaque. Electron-dense structures located close to the plaque are probably phagosomes. Scale bar = 1 μm.

Figure 58: Photoconverted thioflavin bound to β-sheet structures of a senile plaque with an electron-dense center. The periphery of the plaque allows the identification of linear arranged amyloid within a completely disorganized neuropil. Scale bar = 1 µm.
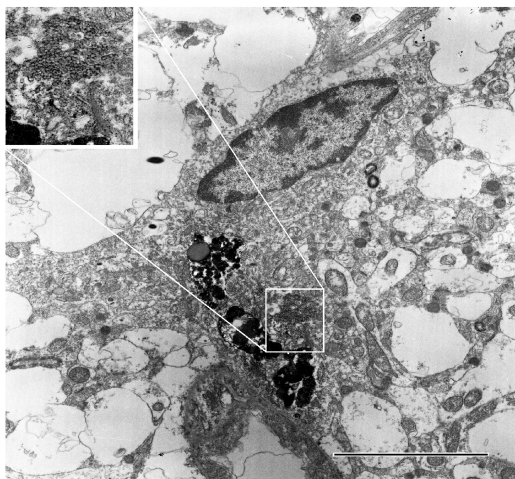
Figure 59: Hippocampal microglia displaying photoconverted thioflavin within heavily degenerated neuronal tissue. Several photoconverted phagosomes are apparent in the cell body. Note the nanoparticles in the vicinity of the cell, at higher magnification in the inset. Scale bar = 5 µm.

3.5.8. Intravenous application of nanoparticles

PBCA nanoparticles could not be found within brain after intravenous application also if coated with polysorbate 80. This applies for HL-23, HL-29, HL-32, HL-33, HL-50, HL-50T, RB-FIX2-PBCA-TF and RB-FIX2-PBCA-TF. No brain uptake were observed for the EPMA/MMA nanoparticles HL-34 – HL-42 or 2003/I-SA. Considerable amounts of all particles were seen in the liver of the injected mice and less in the spleen (Fig. 60). Negligible numbers of particles were found in kidney and lung, whereas heart muscles were apparently devoid of particles (Fig. 60). High amounts of nanoparticles were detectable in blood after one hour but not after 24 hours (data not shown).
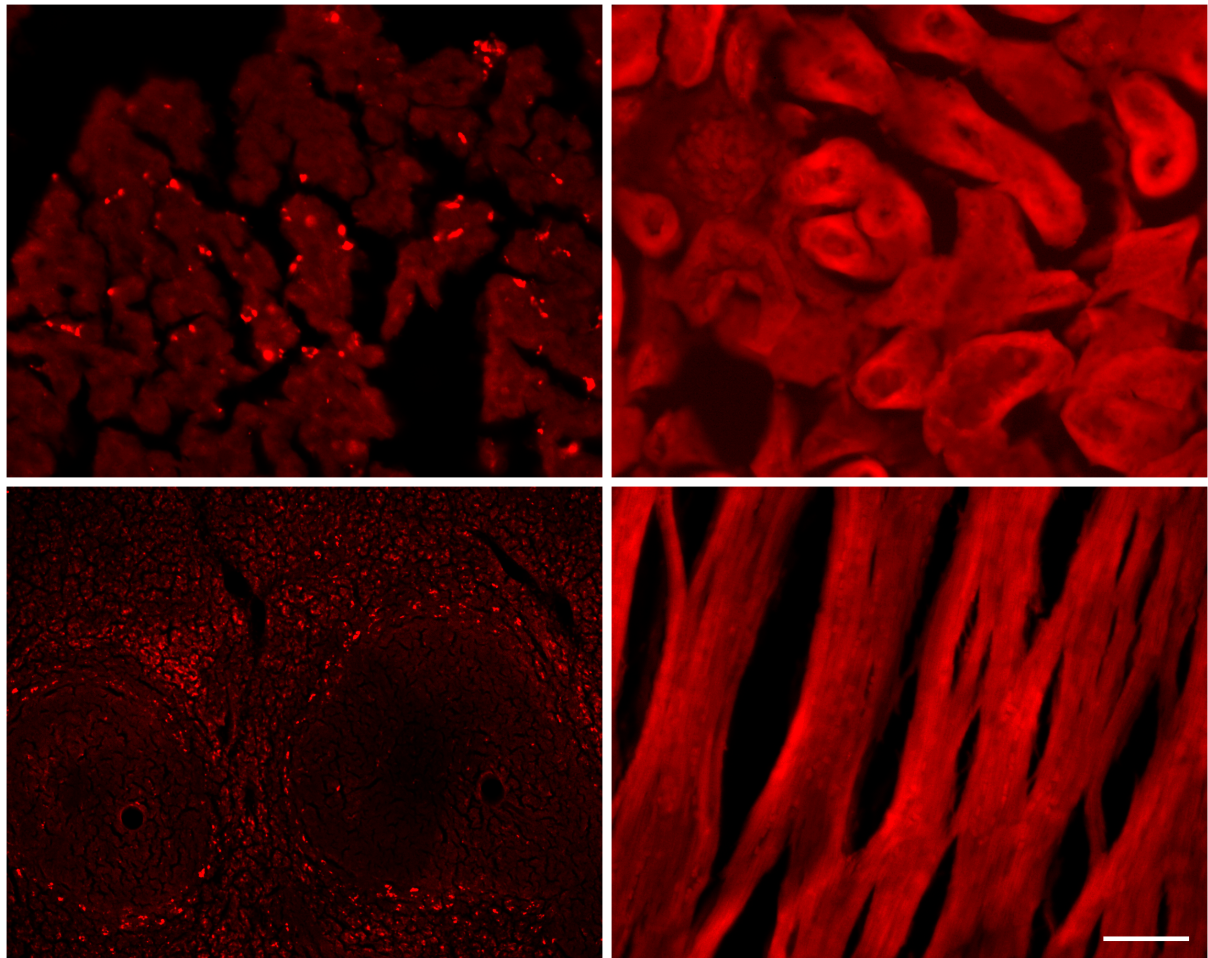
Figure 60: *In-vivo* distribution of nanoparticles 2000/I-SA/ApoE after intravenous application in a wild-type mouse. Considerable amounts could be found in liver (top left) and spleen (bottom left), whereas no particles were found in kidneys (top right) and heart (bottom right). Scale bar: 50 µm

Nanoparticles coated with ApoE peptide were detected within brain tissue (Fig. 61). However, most of the particles were found in the liver of the treated animals.
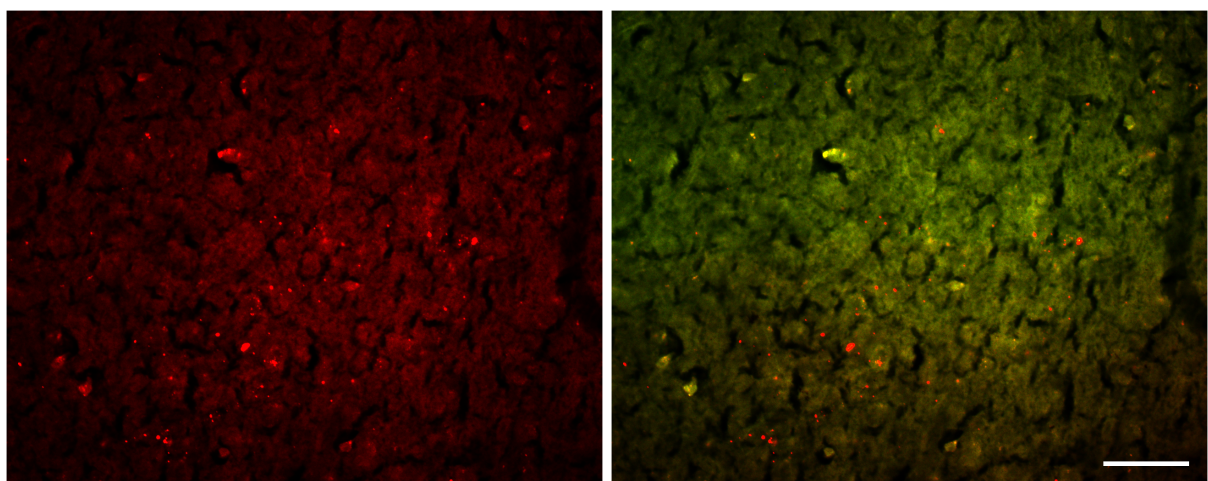
Figure 61: Nanoparticle 2003/I-SA/ApoE found in murine brain 3 days after intravenous application (wild-type mouse). Red fluorescent particles (left), within brain tissue (bottom). Scale bar 50 µm

3.6. Polymeric nanoparticles and blood coagulation

After intravenous application of the polymethacrylate nanoparticles HL-35 numerous cavities in the brain of two treated mice were observed (fig. 62). As a possible reason a stroke was suspected and, therefore, the activation of the coagulation system by polymeric nanoparticles was investigated.

Figure 62: Necrotic areas within murine brain after intravenous application of polymethacrylate nanoparticles HL-35. Photography of the isolated brain mounted on a slide microtome. Note the numerous cavities in both hemispheres.

PBCA nanoparticles displayed increased Endogenous thrombin potential as well as an increased thrombin peak compared to a reference sample (tab. 11, fig. 63). In addition, the lag phase and the time to peak is shortened. One polystyrene core was investigated and revealed an analogous result but only marginal increase of the thrombin peak. For the polymethacrylate nanoparticles it was found that the Endogenous thrombin potential and thrombin peak were slightly diminished, the lag phase was shortended.

Table 11: Thrombin generation in platelet-rich (PRP) and platelet-poor plasma (PPP) spiked with nanoparticles. PBCA nanoparticles HL-23, HL-29, HL-32, HL-33, FIX2 and FIX3; polystyrene core particle HL-31 and polymethacrylate nanoparticles HL-35 - HL-38. The values for the reference plasma are given with standard deviation.

	Endogenous thrombin potential / FU		thrombin peak / FU s^{-1}		lag phase / s		time to peak / s	
	PPP	PRP	PPP	PRP	PPP	PRP	PPP	PRP
HL-23	85,9	97,6	0,09	0,17	806	618	330	309
HL-29	90,3	96,5	0,12	0,19	663	628	354	268
HL-31	71,5	79,8	0,06	0,08	757	589	291	400
HL-32	93,9	101,6	0,12	0,24	754	590	325	309
HL-33	89,1	111,8	0,09	0,25	822	610	448	281
HL-35	47,1	52,8	0,03	0,04	448	553	604	499
HL-36	37,1	44,9	0,02	0,04	597	612	577	559
HL-37	43,0	52,7	0,03	0,07	512	482	601	270
HL-38	45,3	47,6	0,03	0,04	500	551	613	623
FIX-2	66,8	77,7	0,05	0,07	875	696	479	538
FIX-3	101,5	111,1	0,10	0,15	840	662	395	363
Reference	52,6±7,3	68,8±4,6	0,04±0,01	0,06±0,01	949±70	670±73	577±188	504±160
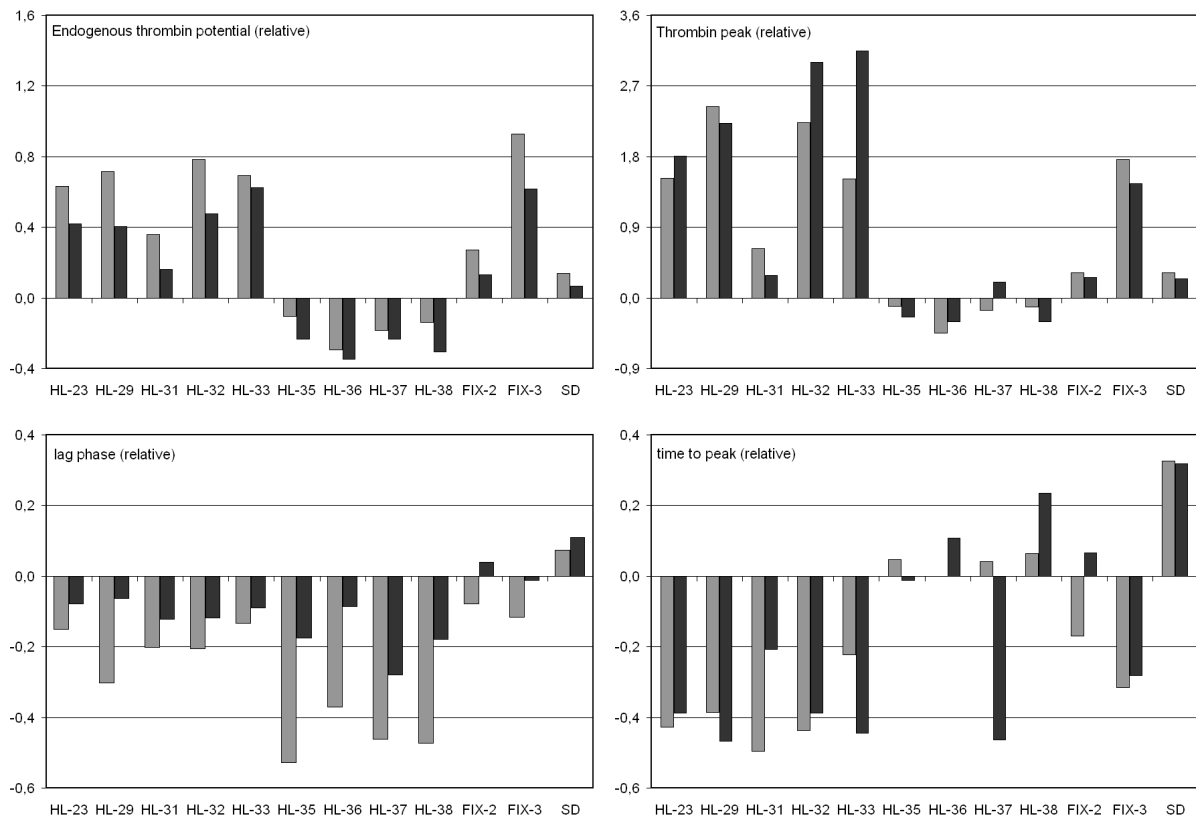
Figure 63: Relative changes in thrombin generation in platelet-rich (PRP, light gray) and platelet-poor plasma (PPP, dark gray) spiked with nanoparticles. PBCA nanoparticles HL-23, HL-29, HL-32, HL-33, FIX2 and FIX3; polystyrene core particle HL-31 and polymethacrylate nanoparticles HL-35 - HL-38. "SD" shows the standard deviation of the reference sample.

The differences between platelet-rich and platelet-poor plasma were insignificant, only the lag phase in PPP was shorter applying polymethacrylate nanoparticles.

The analysis of the platelet function using FACS revealed unchanged platelet activity and activatability for the PBCA nanoparticles HL-23, HL-29, HL-32 and HL-33 and a higher sensitivity to thrombin receptor activation (fig 64). The polystyrene core HL-31 showed strong CD62P expression in unactivated platelets as well as after activation by ADP and TRAP-6.

All polymethacrylate nanoparticles displayed increased platelet activity and activatability. These values may be interfered by the fluorescence of the particle itself.
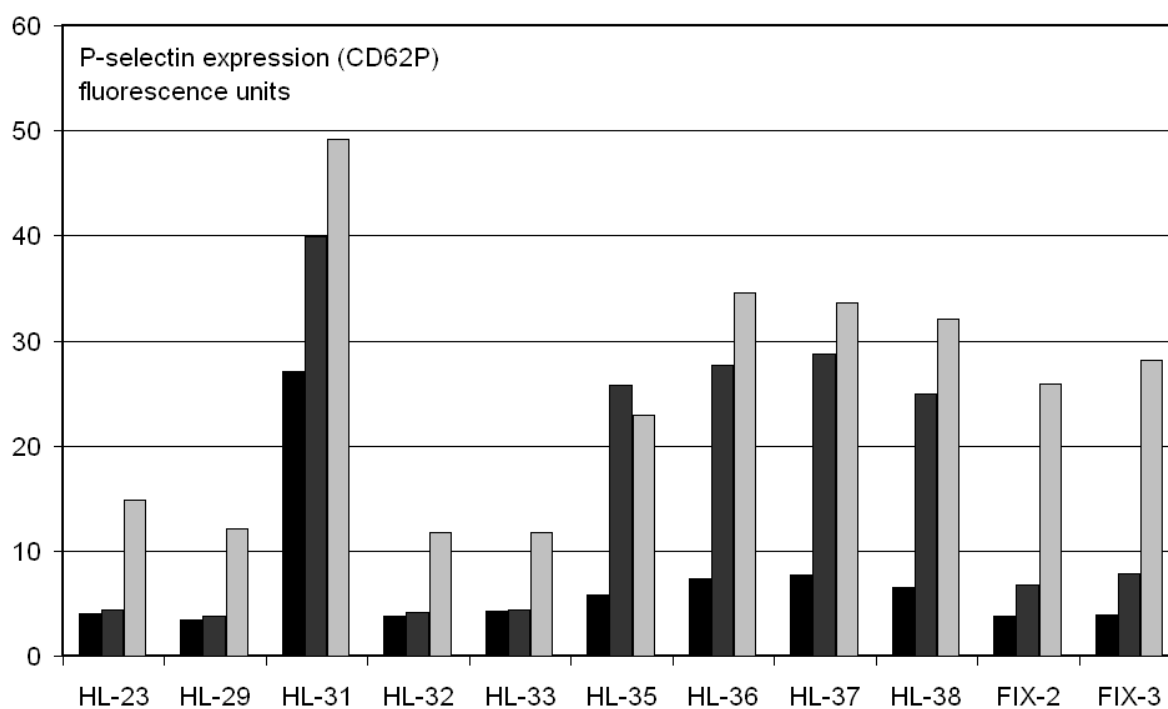
Figure 64: Determination of platelet function by P-selection (CD62P) expression, unactivated (dark gray), activated with ADP (gray) and TRAP-6 (light gray). PBCA nanoparticles HL-23, HL-29, HL-32, HL-33, FIX2 and FIX3; polystyrene core particle HL-31 and polymethacrylate nanoparticles HL-35 - HL-38.

4.   Discussion

4.1.   Physical properties of polymeric nanoparticles

4.1.1. Absorbance spectra of polymeric nanoparticles

The measurement of light absorbance spectra revealed a superimposed signal of RAYLEIGH scattering and absorbance by particle components and dyes. Therefore, it is possible to estimate particle sizes using photometric methods. Nevertheless, two different values determine RAYLEIGH scattering, the radius of the particle and its polarizability $\tilde{\alpha}$. If one is known, the other one can be estimated[61]. Polysorbate 80-coating of nanoparticles with encapsulated thioflavin T did not influence the absorbance spectrum[62].

The degradation of polymeric nanoparticles was observed using absorbance measurement data. The reaction process was determined by the concentration of enzyme and the nanoparticles, e.g., the degradation was slowed be lower enzyme concentration or increased nanoparticle concentration. Surface coating led to decreased reaction velocity, but under the used physiological condition regarding temperature, pH and salt content, the nanoparticles were degraded within hours. Changes of these reaction conditions influenced the degradation process[61]. It is noteworthy, that polymeric nanoparticles may swell when incubated in salt-containing solution, a process that must be considered in experiments[61]. To ensure physiological conditions, all further experiments were performed in buffered solutions at a pH of 7.4.

In summary, analyzing nanoparticle size and degradation by absorbance measurements allows fast and practicable handling, high throughput and requires low technical effort. Two limitations must be considered, for RAYLEIGH scattering the nanoparticle diameter must be smaller than the wavelength; aggregation and sedimentation should be avoided.

4.1.2. Fluorescence spectra of polymeric nanoparticles

The model drugs thioflavin T and thioflavin S showed strong fluorescence when encapsulated in polymeric nanoparticles. This allows the identification of particles *in vitro* and *in vivo*. Nanoparticles containing two fluorophores showed beside the spectra of the used dyes an additional Förster resonance energy transfer-signal, which enables to study the integrity of core-shell nanoparticles. *In vivo*, the fluorescence of the thioflavin-filled shell diminished and the FRET-signal diminished within three days, while the rhodamine B-signal of the the core was detectable close to the injection site.

In this work, it was not possible to investigate nanoparticle degradation *in vitro*, due to the lack of a multi-channel fluorescence spectrometer, equipped with the required wavelength filters and temperature regulation.

4.1.3. Static and dynamic light scattering

Both static and dynamic light scattering allowed to determine particle radius and radius distribution. The radii of the investigated nanoparticle core laid between 33 and 40 nm. Core-shell nanoparticles displayed values between 50 and 72 nm when measured by static light scattering and subsequent analysis in a Guinier plot. This technique bases on the acquisition of scattering intensity data using different particle concentrations and scattering angles. It is noteworthy, that higher concentrations of nanoparticle suspensions may induce multiple scattering processes, which negatively influence the analysis.

Dynamic light scattering bases on the diffusion of nanoparticles in the selected solvent and is determined by the hydrodynamic radius of the particles. This may also include water molecules that were bound to the particle by its surface charges. Therefore, hydrodynamic radii may be larger than the radius of the particle itself. For the polystyrene core HL-22 a hydrodynamic radius of 35.6 ± 0.5 nm was revealed, compared to 33.8 ± 1.8 nm from static light scattering. The radii for HL-31 were found to be nearly identical,40.8 ± 0.3 nm and 40.0 ± 0.5 nm, respectively. Polystyrene nanoparticle surfaces contain negatively charged sulfate groups from the polymerization process, which may lead to a solvation layer. For the PBCA

nanoparticles HL-23 the hydrodynamic radius was found to be slightly smaller than the radius based on static light scattering data, 67.5 ± 2.8 nm compared to 72.2 nm. Coating of PBCA nanoparticles with polysorbate 80 could be detected with a gain of about 0.5 nm. Red fluorescent nanoparticles could not be investigated due to strong absorption of the incident light and their strong fluorescence that interferes with the scattered light. Furthermore, fluorescent dyes are bleached by the intense laser light, therefore, the interference with light scattering changes during measurement.

The determination of nanoparticle degradation by light scattering failed due aggregation of particles, degradation intermediates or core particles. It could be shown, that neutralization of the negatively charged surface of polystyrene nanoparticles led to aggregation.

Light scattering requires a high technical effort, additionally, static light scattering is time consuming. Nevertheless, this technique is nearly unrivaled for radius determination. Alternative techniques like atomic force microscopy can not be used with polymeric nanoparticles that tend to aggregation and must be solved in a aqueous solution.

4.1.4. Small angle neutron scattering

The second technique to investigate nanoparticle radius and degradation was small angle neutron scattering. Radius determination using the GUINIER law revealed values comparable to light scattering. For HL-22 the radius of gyration was found to be 27.3 nm, with static light scattering 25.9 nm, for HL-31 the value was 31.4 nm compared to 31.0 nm, respectively. The variation of the solvent neutron scattering contrast had no influence on the radius determination, if the solvent did not match the particles scattering contrast. If the latter occurs, the extinguished scattering intensity precludes any data. On the other hand, using different solvent contrasts allow to investigate nanoparticle cores or shells independently from each other. This approach was used in degradation experiments, showing that the shell of the nanoparticle was clearly degraded, whereas the core remained unchanged.

The particle degradation was performed under conditions comparable to the experiments using photometry. Half-life of shell degradation revealed by both

experiments was comparable despite the used of different detection techniques. For HL-50 the scattering intensity decreased more than 90% with a half-life of 1.7 hours, compared to 1.8 hours shown by photometry. The degradation of the HL-52 shell led to a 90% reduction of the scattering intensity with a half-life of 1.9 hours. Due to the high concentration of porcine liver esterase the scattering signal may be influenced by the enzyme causing an insufficient determination of nanoparticle radii using the Guinier law. Furthermore, the short measurement interval led to data with low statistic quality.

In a second approach the degradation was performed outside the instrument and with higher particle concentrations. Prior the measurement, samples were highly diluted in cold solvent which stops the enzymatic reaction. Measurements were carried out with longer data acquisition, which led to data with higher statistical quality and lower influence of the enzyme. In this experiment, the shell of the used HL-52 nanoparticle was not degraded completely. An explanation may be the relatively low concentration of the enzyme. Furthermore, the enzyme did not degrade the polycyanoacrylate backbone of the polymer. These molecules may form random coils or stay bound to the nanoparticle core; in both cases the molecules led to isotropic scattering. A further reduction of the enzyme concentration or applying an enzyme with higher activity may be helpful to improve data quality in further experiments.

A further advantage of contrast variation is the determination of the particle neutron scattering contrast. It could be show, that all particles exhibited contrast comparable to the predicted values. This underlines that the investigated nanoparticles are homogeneous and, therefore, do not include solvent from fabrication.

Two fit models were used to interpret neutron scattering data. The results of fitting revealed high accordance to the data obtained by the Guinier law. On the other hand, in both models the minimalization parameter is dominated by the intensities determined by for low q-values, which are used in the Guinier law. The determination of radius distribution is influenced by the estimation of the error of q. If the data are calculated with a higher number of nodes for the distribution of q then a lower radius distribution was achieved.

Model 1 is useful for fitting data from homogeneous nanoparticles. Because the radius distribution of the core and the shell is constricted to the same value, fitting fails for core-shell nanoparticles, where the core radius distribution is usually smaller than the shell radius distribution. This applies especially for nanoparticles consisting of polymers with different scattering length densities like HL-52. On the contrary, HL-50 can be assumed as homogeneous particles, the contrast of core and shell differ with less than 5%. Model 2 consists of seven different parameters to be fitted in analysis. Therefore, it is impossible to fit data with reproducible results. Nevertheless, this model can be used if core or shell data are known and do not need to be fitted. Furthermore, it is possible to fit samples with different solvent contrast simultaneously. Both models can only be used, when the obtained data display good statistics.

Small angle neutron scattering is a method with extremely high technical and analytical effort. The feasibility of contrast variation allows to investigate the structure of polymeric nanoparticles. The postulated enzymatic degradation of polymeric nanoparticles could be verified using small angle neutron scattering. The reduction of scattering intensity is a direct measure of the degradation process.

4.2. Detection and targeting of β-amyloid in transgenic mice

The transgenic mice used in this work showed a severe β-amyloidosis in the brain of the APPSwe/PS1 as well as the APPSwe/PS1dE9 strain. Despite a high general β-amyloid load no vascular deposits were found. Plaques were detected using the antibodies SA 720 and SA 721 which bind to human $A\beta_{1-40}$, $A\beta_{1-42}$ and $A\beta_{1-43}$[234]. The high specificity of the performed indirect immunofluorescence labeling allows a good detection of β-amyloid with a low background signal. Furthermore, SA 720 and SA 721 enable Aβ detection without formic acid pretreatment which would interfere with the preceding thioflavin binding of fibrillar plaques *in vivo*.

The dyes thioflavin T and thioflavin S revealed a similar distribution pattern of plaques. On the other hand, concomitant thioflavin staining and Aβ immunolabeling showed slight differences; the thioflavins could only found in the core of the plaques, whereas the antibody revealed β-amyloid also in the surrounding area. These

findings are in accordance with the fact that thioflavins bind to highly aggregated fibrils, which are formed in the center of the plaque, but not bind to diffusely occurring Aβ[145][146][142]. After intrahippocampal application of the free dyes strong labeling of β-amyloid was found, whereas thioflavin T showed a low but significant background. The labeling of Aβ diminished with the distance from the injection site, especially the contralateral hemisphere showed an lower signal. Both dyes are known to be unable to pass the blood-brain barrier[146] and are, therefore, appropriate model drugs for the investigation of brain targeting.

The uncharged thioflavin derivative BTA-2 is able to pass the blood-brain barrier[146] and was considered as a possible positive control in animal experiments. However the high background of the labeling which may be mediated by its hydrophobicity and its low solubility in water led to the exclusion from further experiments. Solutions of BTA-2 which were used in the experiments contained larger amounts of dimethyl sulfoxide and alcohols, and both solvents may influence the permeability of the blood-brain barrier[166][159].

4.2.1. Intracerebral application of polymeric nanoparticles

To prove distribution and degradation the polymeric nanoparticles were injected directly into the brain. After intracerebroventricular application the particles were found distributed within the cerebrospinal fluid but not within the brain tissue. Nevertheless, staining of β-amyloid plaques by thioflavins released from degradable PBCA nanoparticles was observed. The specificity of the staining was confirmed by subsequent immunolabeling *in vitro*. Similarly, after intracerebroventricular injection an *in vivo* labeling of β-amyloid was observed with a fluorescent acetylcholinesterase inhibitor released from nanoparticles[235].

After intrahippocampal application the nanoparticles were found predominantly close to the injection site. Diffusion of the particles was more restricted within brain tissue compared to the free dyes. Restricted diffusion is a finding described earlier in aged mice with severe amyloidosis[236], but also the particle size and surface charges have to be considered. Fluorescent PMAA/MAA nanoparticles were observed close to the

injection site but no labeling of β-amyloid plaques was observed; this underlines the stability of the methacrylate nanoparticles.

In contrast, thioflavins released from PBCA nanoparticles targeted β-amyloid after intrahippocampal injection but with lower intenity compared to the free dye. Three days after application, the double-fluorescent RB-FIX3-TF-PBCA particles were found exhibiting the red fluorescence of the core but neither green fluorescence of the shell nor a FRET signal. Both findings support the methodical approach chosen in this work: after penetration of the blood-brain barrier, in this case physically, the nanoparticle shell was degraded, the dye or drug was released and the cores remained at the site of degradation.

The nanoparticle 2003/I-SA could be detected by fluorescence labeling as well as by biotinylated horseradish peroxidase and subsequent staining with nickel-enhanced diaminobenzidine. The streptavidin bound on the particle surface can be used for coupling a signal peptide for the targeting of organs, tissues or cells, for the coupling of drugs or diagnostic agents and for the detection of the particle itself.

After photoconversion of the fluorescent dye, electron microscopy was used to detect the dye and nanoparticles in brain tissue of treated mice. Nanoparticles were found in phagosomes, a cellular structure responsible for digestion of particular substances. Furthermore, electron dense β-amyloid plaques were found. Electron microscopy can be applied to detect nanoparticles also following their penetration through the blood-brain barrier[55][233].

4.2.2. Intravenous application of nanoparticles

None of the intravenously injected nanoparticles entered the brain, if the ApoE peptide was not coupled to the particle surface. Most of the particles were found in the liver, less in spleen, only a few in lung or kidney, whereas no particles were detected in the heart. The accumulation of particles in the liver can be explained by its function for detoxification, whereas the spleen plays an important role in the cellular immunity.

The uptake into the brain was observed using nanoparticles 2003/I-SA/ApoE which exhibit an ApoE signal peptide at their surface. It was described that coating with

polysorbate 80, as realized in HL-50T, leads to the binding of ApoE to the particle surface and mediates brain uptake via the LDL receptor[12][117]. Nevertheless, HL-50T was not able to pass the blood-brain barrier. This might be explained by a low efficiency of ApoE binding, since the surface charge density determines the protein adsorption on polymeric nanoparticles as shown previously by two-dimensional electrophoresis[237]. Liposomes coated with an apolipoprotein peptide fragment considerably improved their internalization by endothelial cells *in vitro*[119]. Therefore, biotinylated ApoE peptide were bound to the particle by streptavidin-biotin complexes. Despite increased targeting of the blood-brain barrier the majority of the particles were still found in liver and spleen. LDL metabolism is a function of the liver and, hence, LDL receptor-mediated uptake into the liver may be the major reason for that finding. As an alternative to artificial drug carriers natural transport systems exist, e.g., for hexoses, amino acids or monocarboxylic acids which might be useful for the transport of certain drugs through the blood-brain barrier[238]. In addition, endothelial cells of the BBB are predominantly equipped with receptors, e.g., for transferrin[239]. It might be assumed that nanoparticles with surface-bound transferrin or antibodies directed against the transferrin receptor could be preferentially bound to endothelial cells of the blood-brain barrier and facilitate the brain targeting of nanoparticles. A recently published study suggests that a combination of magnetic nanoparticles, guided by an external magnetic field, and focused ultrasound to open the blood-brain barrier, synergistically delivers therapeutics to the brain[240].

It was not possible to quantify the particle load for an organ. A possible way would be the use of radiolabeled nanoparticles[241] or radiolabeled model drugs[242] which allow quantification by its radiation.

The mechanisms of the drug delivery into the brain remain to be further elucidated. Nanoparticles may be transported simultaneously to the diapedesis of lymphocytes through endothelial cells of the blood-brain barrier[243]. In addition, alcohols like n-butanol as degradation products of PBCA and surface coating tensides like polysorbate 80 can partially disrupt the BBB[166][159]. It was shown that nanoparticle surface charges alter integrity and permeability of the blood-brain barrier[123].

Collectively, nanoparticles are promising drug carriers for charged, hydrophilic drugs with low tendency to penetrate the blood brain barrier after intravenous application.

4.3. Alteration of the blood coagulation system

The polymeric nanoparticles used in this work caused a significant alteration of blood coagulation. Two different effects were observed depending on the applied polymers. In a thrombin generation assay poly(butyl cyanoacrylate) nanoparticles showed an increased thrombin peak and an increased Endogenous thrombin potential. The former reveals the velocity of thrombin formation, the latter the total amount of thrombin that was generated. Furthermore, the lag phase, the time until the first generation of thrombin, is slightly diminished, while the time from the start of the reaction until the maximum velocity is clearly shortened. All these alterations indicate that PBCA nanoparticles activate the coagulation system and may catalyze thrombin generation and, therefore, increase the risk of thromboembolic events[244][245]. The polystyrene core particle HL-32 displays a similar pattern but with lower intensity. Platelet function were apparently not altered by the particles HL-23, HL-29 and HL-33. There is no explanation for the highly altered platelet function induced by HL-32; this finding is inconsistent with the moderate particle-induced activation of thrombin generation.

The EPMA/MAA nanoparticles showed a different pattern of coagulation activation. Whereas generation of thrombin is unchanged, the lag phase is clearly shortened. This result is supported by increased activation and activatability of the platelet function possibly resulting in a thrombophilic state. The data may explain the finding of necrotic areas within two murine brains after intravenous application of HL-35.

Blood coagulation is catalyzed by components of the platelet surface, which lead to shorter lag phase and time to peak as well as higher thrombin peak and Endogenous thrombin potential[202]. Since the effects are measured in platelet-rich and platelet-poor plasma, nanoparticles not only interact with platelets but also act like platelets.

On the other hand, these results may be helpful in the development of platelet substitutes for patients with bleeding complications and blood loss. Nano- or microparticles coated with components of the coagulation system may be a therapeutic option in the treatment of live-threatening bleedings[206][207]. Furthermore, nanoparticles could serve as tool for targeting of platelets[205].

5. Summary

The development of a great variety of nanoparticles opened new approaches in diagnosis and therapy of diseases. Nanoparticles act as carrier for drugs and control their stability, release and site of pharmacological action. This allows lower dosage, higher therapeutic impact and fewer side effects. Moreover, such carriers enable the application of insoluble or unstable drugs, which are not applicable as free compounds. In this work, thioflavins, encapsulated in polymeric nanoparticles, were used as model drugs for the targeting of β-amyloid through the blood-brain barrier.

Several materials are used for the formulation of polymeric nanoparticles. Organic non-toxic degradable polymers like poly(butyl cyanoacrylate) are used to embed or adsorb drugs. The surface of nanoparticle can be modified to suppress or increase immunological reactions, the latter may be used for vaccination, or to bind agents that control the targeting by specific or unspecific interaction with tissues, cells or receptors. Furthermore, surface modifications and the high surface-volume ratio allow a controlled release of the transported drugs.

In this work two types of polymeric nanoparticles were investigated regarding their ability to penetrate the blood-brain barrier. Core-shell nanoparticles were made from a polystyrene core and a shell of poly(butyl cyanoacrylate). The particle shells are easily degradable by enzymes in the brain tissue. Homogeneous nanoparticles were made of poly(2,3-epoxypropylmethacrylate-co-methacrylic acid) and are hardly degradable as well as the core of the core-shell particles.

Various physical techniques were investigated for *in vitro* analysis of nanoparticles. Such methods may be helpful for studying drug carriers regarding drug load, degradation and drug release and, therefore, may help to accelerate development and reduce the number of animal experiments. For these experiments porcine liver esterase was used as a model enzyme for the degradation of the particles.

In the present work it could be shown that polymeric nanoparticles exhibit RAYLEIGH scattering properties, a linear relationship between absorbance and the inverse 4th power of the wavelength. This allows to estimate the particle radius which is proportional to the slope of this relationship by a rather simple method like photometry. The absorbance signal is superimposed by the absorbance spectrum of embedded substances like thioflavin T and the polymer itself. Because the

relationship between absorbance and wavelength remained linear also during *in vitro* degradation experiments; the decreasing particle radius can be observed by diminished light absorbance. It is noteworthy, that Rayleigh scattering only applies for particles with a size clearly smaller than the wavelength of the light.

Depending on its shape and size particles scatter light in an angle-dependent manner; this property is used in static light scattering experiments. On the other hand, dynamic light scattering detects fluctuations of the scattered light induced by the Brownian movement. The velocity of the movement is determined by a diffusion constant and is connected to the hydrodynamic radius of the particles by the Einstein-Stokes equation. Both methods are suitable for the determination of radii if the radius distribution is low and nanoparticle aggregates do not occur. It was not possible to monitor enzymatic nanoparticle degradation with reliable results due to the occurrence of large aggregates caused by the neutralization of the negatively charged nanoparticle surface by ions of the buffered solution or released positively charged thioflavins. Further data are required to possibly avoid the aggregation of nanomaterials at the site of degradation.

While light scattering techniques are restricted to the surface of nanoparticles, neutrons are able to penetrate soft matter. Small angle neutron scattering is dominated by the scattering of smaller atoms, especially hydrogen, which are present in organic polymers. In this work it could be shown, that this methodology is useful for the investigation of nanoparticle structure and degradation.

Small angle neutron scattering is determined by the neutron scattering contrast difference between the sample and the surrounding solvent, each molecule or polymer exhibits a specific contrast. By the variation of the solvent contrast, the contrast of the investigated polymeric nanoparticles could be determined. The measured contrasts were identical to the calculated values and, therefore, homogeneous nanoparticles can be assumed.

The degradation of nanoparticles was investigated using small angle neutron scattering. This method revealed, that the shell of core-shell particles was degraded in a time-dependent manner, the degradation led to reduction of scattering intensity of about 90%, the half-live was comparable to experiments performed with light absorbance measurements. The introduction of perdeuterated polystyrene cores,

with a highly different scattering contrast compared to PBCA, allows to observe that hardly degradable nanoparticle cores remained unchanged during degradation.

Small angle neutron scattering is useful for the investigation of physico-chemical properties of polymeric nanoparticles. Beside the usual use for particle size determination it allows the quantification of particle degradation.

One of the most challenging drug targets is the brain, which is separated from the blood stream by the blood-brain barrier. Nearly all substances are transported either selectively or actively to the brain, and possible toxic substances are removed or degraded by cells within the blood-brain barrier. One of the most promising approaches to overcome this obstacle is to mask the drug or the drug carrier to enable receptor-mediated uptake into the brain. It was concluded before, that drugs delivered by nanoparticles passed the blood-brain barrier, but there is only indirect evidence, e.g., by measuring drug-induced diminished pain[12]. Until now the uptake and degradation of drug-loaded particles has not been shown directly by detecting them in brain tissue after intravenous application.

Nanoparticles investigated in the present study contain as model drugs the fluorescent dyes thioflavin S or thioflavin T. Both green fluorescent dyes are known to bind to β-amyloid fibrils, the major component of plaques frequently occurring in Alzheimer's disease. As free dyes thioflavin S and thioflavin T are unable to penetrate the blood-brain barrier and are, therefore, useful model drugs. If the nanoparticles penetrate the blood-brain barrier, the shell will be degraded and dye molecules are released. After binding to β-amyloid fibrils thioflavin S or T can be detected by fluorescence microscopy. A fluorescent undegradable core may remain at the injection site and is detectable simultaneously.

To ensure to uptake of drug-loaded nanoparticles, an apolipoprotein E dipeptide was coupled covalently to the particle surface which may result in receptor-mediated uptake. In this work, the uptake of polymeric nanoparticles into the brain was tested in transgenic mice with an age-dependent β-amyloidosis.

Various experiments were performed to investigate uptake, degradation and targeting of nanoparticles *in vivo*. Injection of the free model drug thioflavin T directly into the brain revealed strong labeling of β-amyloid plaques but also limited diffusion within the brain. Application of double-fluorescent nanoparticles, with a red fluorescent core

and a green fluorescent shell, showed complete degradation of the shell and targeting of plaques by thioflavin T, whereas the undegradable core remained at the injection site. After intravenous application of unmodified nanoparticles neither penetration of the blood-brain barrier was observed nor particles and labeled plaques were found in the brain. Most of nanoparticles were detected in the liver, responsible for metabolism and detoxification and in the spleen, showing involvement of the immune system. No or very few particles were found in heart, kidneys and lung.

Penetration of the blood-brain barrier was only observed with very small nanoparticles with the apolipoprotein E dipeptide bound to the surface. Nevertheless, only few particles reached the brain, the majority was still found in liver and spleen.

In summary, the present work describes various techniques for the elucidation of physico-chemical properties of polymeric nanoparticles *in vitro* and *in vivo*. It was shown, that structure and degradation of nanoparticles could be monitored using light absorbance, fluorescence measurements, light and neutron scattering. These methods may be helpful for the development of polymeric drug-carriers. Simultaneously, these methods may reduce the number of animal experiments which are needed for full understanding of nanoparticle properties and possible disadvantages.

Using animal experiments, it could be shown, that nanoparticles are able to reach the blood-brain barrier, but still with low efficiency. Further improvements, like surface modifications or alternative materials, may lead to new opportunities in diagnosis or therapy of diseases using this seminal drug carriers.

6. Bibliography

[1]   Kreuter J. Nanoparticles and nanocapsules - New dosage forms in the nanometer size range. Pharm Acta Helv 53, pp. 33-39 (1978)

[2]   Kreuter J, Liehl E. Long-term studies of microencapsulated and adsorbed influenza vaccine nanoparticles. J Pharm Sci 70, pp. 367-371 (1981)

[3]   Kreuter J. Evaluation of nanoparticles as drug-delivery systems. III: Materials, stability, toxicity, possibilities of targeting, and use. Pharm Acta Helv 58, pp. 242-250 (1983)

[4]   Couvreur P, Kante B, Roland M, Speiser P. Adsorption of antineoplastic drugs to polyalkylcyanoacrylate nanoparticles and their release in calf serum. J Pharm Sci 68, pp. 1521-1524 (1979)

[5]   Couvreur P, Kante B, Lenaerts V, Scailteur V, Roland M, Speiser P. Tissue distribution of antitumor drugs associated with polyalkylcyanoacrylate nanoparticles. J Pharm Sci 69, pp. 199-202 (1980)

[6]   Couvreur P, Kante B, Grislain L, Roland M, Speiser P. Toxicity of polyalkylcyanoacrylate nanoparticles II: Doxorubicin-loaded nanoparticles. J Pharm Sci 71, pp. 790-792 (1982)

[7]   Kante B, Couvreur P, Dubois-Krack G, De Meester C, Guiot P, Roland M, Mercier M, Speiser P. Toxicity of polyalkylcyanoacrylate nanoparticles I: Free nanoparticles. J Pharm Sci 71, pp. 786-790 (1982)

[8]   National Institutes of Health. PubMed. http://www.ncbi.nlm.nih.gov/pubmed/

[9]   Duncan R. The dawning era of polymer therapeutics. Nat Rev Drug Discov 2, pp. 347-360 (2003)

[10]   Lanza GM, Yu X, Winter PM, Abendschein DR, Karukstis KK, Scott MJ, Chinen LK, Fuhrhop RW, Scherrer DE, Wickline SA. Targeted antiproliferative drug delivery to vascular smooth muscle cells with a magnetic resonance imaging nanoparticle contrast agent: Implications for rational therapy of restenosis. Circulation 106, pp. 2842-2847 (2002)

[11]   Alyautdin RN, Petrov VE, Langer K, Berthold A, Kharkevich DA, Kreuter J. Delivery of loperamide across the blood-brain barrier with polysorbate 80-coated polybutylcyanoacrylate nanoparticles. Pharm Res 14, pp. 325-328 (1997)

[12]   Kreuter J, Ramge P, Petrov V, Hamm S, Gelperina SE, Engelhardt B, Alyautdin R, von Briesen H, Begley DJ. Direct evidence that polysorbate-80-coated poly(butylcyanoacrylate) nanoparticles deliver drugs to the CNS via specific mechanisms requiring prior binding of drug to the nanoparticles. Pharm Res 20, pp. 409-416 (2003)

[13]   Panyam J, Zhou W, Prabha S, Sahoo SK, Labhasetwar V. Rapid endo-lysosomal escape of poly(DL-lactide-co-glycolide) nanoparticles: Implications for drug and gene delivery. FASEB J 16, pp. 1217-1226 (2002)

[14]   Weissenböck A, Wirth M, Gabor F. WGA-grafted PLGA-nanospheres: Preparation and association with Caco-2 single cells. J Control Release 99, pp. 383-392 (2004)

[15]   Koziara JM, Lockman PR, Allen DD, Mumper RJ. Paclitaxel nanoparticles for the potential treatment of brain tumors. J Control Release 99, pp. 259-269 (2004)

[16]   Gupta M, Gupta AK. In vitro cytotoxicity studies of hydrogel pullulan nanoparticles prepared by aot/n-hexane micellar system. J Pharm Pharmaceut Sci 7, pp. 38-46 (2004)

[17]   Hainfeld JF, Slatkin DN, Smilowitz HM. The use of gold nanoparticles to enhance radiotherapy in mice. Phys Med Biol 49, p. N309-15 (2004)

[18]   Paciotti GF, Myer L, Weinreich D, Goia D, Pavel N, McLaughlin RE, Tamarkin L. Colloidal gold: A novel nanoparticle vector for tumor directed drug delivery. Drug Deliv 11, pp. 169-183 (2004)

[19]   Gupta AK, Gupta M. Synthesis and surface engineering of iron oxide nanoparticles for biomedical applications. Biomaterials 26, pp. 3995-4021 (2005)

[20]   Müller RH, Mäder K, Gohla S. Solid lipid nanoparticles (SLN) for controlled drug delivery - a review of the state of the art. Eur J Pharm Biopharm 50, pp. 161-177 (2000)

[21]   Wissing SA, Kayser O, Müller RH. Solid lipid nanoparticles for parenteral drug delivery. Adv Drug Deliv Rev 56, pp. 1257-1272 (2004)

[22]   Dyer AM, Hinchcliffe M, Watts P, Castile J, Jabbal-Gill I, Nankervis R, Smith A, Illum L. Nasal delivery of insulin using novel chitosan based formulations: A comparative study in two animal models between simple chitosan formulations and chitosan nanoparticles. Pharm Res 19, pp. 998-1008 (2002)

[23]   Huang M, Khor E, Lim L. Uptake and cytotoxicity of chitosan molecules and nanoparticles: Effects of molecular weight and degree of deacetylation. Pharm Res 21, pp. 344-353 (2004)

[24]   Cascone MG, Lazzeri L, Carmignani C, Zhu Z. Gelatin nanoparticles produced by a simple W/O emulsion as delivery system for methotrexate. J Mater Sci Mater Med 13, pp. 523-526 (2002)

[25]   Damascelli B, Patelli GL, Lanocita R, Di Tolla G, Frigerio LF, Marchianò A, Garbagnati F, Spreafico C, Tichà V, Gladin CR, Palazzi M, Crippa F, Oldini C, Calò S, Bonaccorsi A, Mattavelli F, Costa L, Mariani L, Cantù G. A novel intraarterial chemotherapy using paclitaxel in albumin nanoparticles to treat advanced squamous cell carcinoma of the tongue: preliminary findings. AJR Am J Roentgenol 181, pp. 253-260 (2003)

[26]   Fréchet JM. Functional polymers and dendrimers: Reactivity, molecular architecture, and interfacial energy. Science (80-) 263, pp. 1710-1715 (1994)

[27]   Shutava TG, Balkundi SS, Lvov YM. (-)-Epigallocatechin gallate/gelatin layer-by-layer assembled films and microcapsules. J Colloid Interface Sci 330, pp. 276-283 (2009)

[28]   Bowman K, Leong KW. Chitosan nanoparticles for oral drug and gene delivery. Int J Nanomedicine 1, pp. 117-128 (2006)

[29]   Mohamed F, van der Walle CF. Engineering biodegradable polyester particles with specific drug targeting and drug release properties. J Pharm Sci 97, pp. 71-87 (2008)

[30]   Vauthier C, Dubernet C, Fattal E, Pinto-Alphandary H, Couvreur P. Poly(alkylcyanoacrylates) as biodegradable materials for biomedical applications. Adv Drug Deliv Rev 55, pp. 519-548 (2003)

[31]   Arias JL, Gallardo V, Ruiz MA. Engineering of poly(butylcyanoacrylate) nanoparticles for the enhancement of the antitumor activity of gemcitabine. Biomacromolecules , (2009)

[32]   Paulke B, Möglich P, Knippel E, Budde A, Nitzsche R, Müller RH. Electrophoretic 3D-mobility profiles of latex particles with different surface groups. Langmuir 11, pp. 70-74 (1995)

[33]   Soppimath KS, Aminabhavi TM, Kulkarni AR, Rudzinski WE. Biodegradable polymeric nanoparticles as drug delivery devices. J Control Release 70, pp. 1-20 (2001)

[34]   Fitch RM, Prenosil MB, Sprick KJ. The mechanism of particle formation in polymer hydrosols. I. Kinetics of aqueous polymerization of methyl methacrylate. J Polymer Sci C 27, pp. 95-118 (1969)

[35]   Fitch R, Tsai C. Polymer Colloids. R. M. Fitch (Ed.). Plenum, New York, 1971.

[36]   Harkins W. A general theory of the mechanism of emulsion polymerization. J Am Chem Soc 69, pp. 1428-1444 (1947)

[37]   Smith W, Ewart R. Kinetics of emulsion polymerization. Journal of Chemical Physics 16, pp. 592-599 (1948)

[38]   Fitch R. The homogeneous nucleation of polymer colloids. British Polymer Journal 5, pp. 467-483 (1973)

[39]   Leonard F, Kulkarnir RK, Brandes G, Nelson J, Cameron JJ. Synthesis and degradation of poly (alkyl-alpha-cyanoacrylates). Journal of Applied Polymer Science 10, pp. 259-272 (1966)

[40]   Douglas S, Illum L, Davies S, Kreuter J. Particle size and size distribution of poly(butyl-2-cyanoacrylate) nanoparticles: I. Influence of physicochemical factors. J Colloid Interface Sci 101, pp. 149-158 (1984)

[41]   Behan N, Birkinshaw C, Clarke N. Poly n-butyl cyanoacrylate nanoparticles: a mechanistic study of polymerisation and particle formation. Biomaterials 22, pp. 1335-1344 (2001)

[42]   Douglas S, Illum L, Davies S. Particle size and size distribution of poly(butyl 2-cyanoacrylate) nanoparticles: II. Influence of stabilizers. J Colloid Interface Sci 103, pp. 154-163 (1985)

[43]   Alyautdin RN, Petrov VE, Langer K, Berthold A, Kreuter J, Kharkevich DA. The delivery of loperamide to the brain by using polybutyl cyanoacrylate nanoparticles. Eksp Klin Farmakol 61, pp. 17-20 (1998)

[44]   Gulyaev AE, Gelperina SE, Skidan IN, Antropov AS, Kivman GY, Kreuter J. Significant transport of doxorubicin into the brain with polysorbate 80-coated nanoparticles. Pharm Res 16, pp. 1564-1569 (1999)

[45]   Vezin W, Florence A. In vitro heterogeneous degradation of poly(n-alkyl-α-cyanoacrylates). J Biomed Mater Res 14, pp. 93-106 (1980)

[46]   Huang C, Lee Y. Core-shell type of nanoparticles composed of poly[(n-butyl cyanoacrylate)-co-(2-octyl cyanoacrylate)] copolymers for drug delivery application: Synthesis, characterization and in vitro degradation. Int J Pharm 325, pp. 132-139 (2006)

[47]   Bootz A, Russ T, Gores F, Karas M, Kreuter J. Molecular weights of poly(butyl cyanoacrylate) nanoparticles determined by mass spectrometry and size exclusion chromatography. Eur J Pharm Biopharm 60, pp. 391-399 (2005)

[48]   Lenaerts V, Couvreur P, Christiaens-Leyh D, Joiris E, Roland M, Rollman B, Speiser P. Degradation of poly (isobutyl cyanoacrylate) nanoparticles. Biomaterials 5, pp. 65-68 (1984)

[49]   Dobrovolskaia MA, McNeil SE. Immunological properties of engineered nanomaterials. Nat Nanotechnol 2, pp. 469-478 (2007)

[50]   Lee JH, Lee HB, Andrade JD. Blood compatibility of polyethylene oxide surfaces. Progress in Polymer Science 20, pp. 1043-1079 (1995)

[51]   Morra M, Occhiello E, Garbassi F. Surface modification of blood contacting polymers by poly(ethyleneoxide). Clin Mater 14, pp. 255-265 (1993)

[52]   Li J, Caldwell KD. Plasma protein interactions with Pluronic-treated colloids. Colloids and Surfaces B: Biointerfaces 7, pp. 9-22 (1996)

[53]   George PA, Donose BC, Cooper-White JJ. Self-assembling polystyrene-block-poly(ethylene oxide) copolymer surface coatings: resistance to protein and cell adhesion. Biomaterials 30, pp. 2449-2456 (2009)

[54]   Faraji AH, Wipf P. Nanoparticles in cellular drug delivery. Bioorg Med Chem 17, pp. 2950-2962 (2009)

[55]   Zensi A, Begley D, Pontikis C, Legros C, Mihoreanu L, Wagner S, Büchel C, von Briesen H, Kreuter J. Albumin nanoparticles targeted with Apo E enter the CNS by transcytosis and are delivered to neurones. J Control Release 137, pp. 78-86 (2009)

[56]   Herz J, Marschang P. Coaxing the LDL receptor family into the fold. Cell 112, pp. 289-292 (2003)

[57]   Gaillard PJ, Visser CC, de Boer AG. Targeted delivery across the blood-brain barrier. Expert Opin Drug Deliv 2, pp. 299-309 (2005)

[58]   Müller RH, Rühl D, Lück M, Paulke BR. Influence of fluorescent labelling of polystyrene particles on phagocytic uptake, surface hydrophobicity, and plasma protein adsorption. Pharm Res 14, pp. 18-24 (1997)

[59]   Kreuter J, Nefzger M, Liehl E, Czok R, Voges R. Distribution and elimination of poly(methyl methacrylate) nanoparticles after subcutaneous administration to rats. J Pharm Sci 72, pp. 1146-1149 (1983)

[60]   O'Sullivan C, Birkinshaw C. Hydrolysis of poly (n-butylcyanoacrylate) nanoparticles using esterase. Polym Degrad Stab 78, pp. 7-15 (2002)

[61]   Bordag N. Biochemische und physikalische Charakterisierung von Nanopartikeln als Wirkstoffträger durch die Blut-Hirn-Schranke. Falkultät für Biowissenschaften, Pharmazie und Psychologie, Universität Leipzig. 2005.

[62]   Siegemund T, Paulke B, Schmiedel H, Bordag N, Hoffmann A, Harkany T, Tanila H, Kacza J, Härtig W. Thioflavins released from nanoparticles target fibrillar amyloid β in the hippocampus of APP/PS1 transgenic mice. Int J Dev Neurosci 24, pp. 195-201 (2006)

[63]   Müller RH, Lherm C, Herbort J, Couvreur P. In vitro model for the degradation of alkylcyanoacrylate nanoparticles. Biomaterials 11, pp. 590-595 (1990)

[64]   Müller RH, Lherm C, Herbort T, Blunk P, Couvreur P. Alkylcyanoacrylate drug carriers: I. Physicochemical characterization of nanoparticles with different alkyl chain length. Int J Pharm 84, pp. 1-11 (1992)

[65]   Han G, Tar M, Kuppam DSR, Friedman A, Melman A, Friedman J, Davies KP. Nanoparticles as a novel delivery vehicle for therapeutics targeting erectile dysfunction. J Sex Med , (2009)

[66]   Eerikäinen H, Kauppinen EI. Preparation of polymeric nanoparticles containing corticosteroid by a novel aerosol flow reactor method. Int J Pharm 263, pp. 69-83 (2003)

[67]   Combadière B, Mahé B. Particle-based vaccines for transcutaneous vaccination. Comp Immunol Microbiol Infect Dis 31, pp. 293-315 (2008)

[68]   Powers M. Nanomedicine, Device & Diagnostics Report. Nanomedicine and nano device pipeline surges 68%. NanoBiotech News , pp. 1-4 (2006)

[69]   Juillerat-Jeanneret L, Schmitt F. Chemical modification of therapeutic drugs or drug vector systems to achieve targeted therapy: Looking for the grail. Med Res Rev 27, pp. 574-590 (2007)

[70]   Brannon-Peppas L, Blanchette JO. Nanoparticle and targeted systems for cancer therapy. Adv Drug Deliv Rev 56, pp. 1649-1659 (2004)

[71]   Deeken JF, Löscher W. The blood-brain barrier and cancer: Transporters, treatment, and Trojan horses. Clin Cancer Res 13, pp. 1663-1674 (2007)

[72]   De Jong WH, Borm PJA. Drug delivery and nanoparticles: Applications and hazards. Int J Nanomedicine 3, pp. 133-149 (2008)

[73]   Davis SS. Biomedical applications of nanotechnology-implications for drug targeting and gene therapy. Trends Biotechnol 15, pp. 217-224 (1997)

[74]   Mintzer MA, Simanek EE. Nonviral vectors for gene delivery. Chem Rev 109, pp. 259-302 (2009)

[75]   Leiden JM. Gene therapy - Promise, pitfalls, and prognosis. N Engl J Med 333, pp. 871-873 (1995)

[76]   Sundaram S, Roy SK, Ambati BK, Kompella UB. Surface-functionalized nanoparticles for targeted gene delivery across nasal respiratory epithelium. FASEB J , (2009)

[77]   Jung T, Kamm W, Breitenbach A, Kaiserling E, Xiao JX, Kissel T. Biodegradable nanoparticles for oral delivery of peptides: Is there a role for polymers to affect mucosal uptake?. Eur J Pharm Biopharm 50, pp. 147-160 (2000)

[78]   Pardeike J, Hommoss A, Müller RH. Lipid nanoparticles (SLN, NLC) in cosmetic and pharmaceutical dermal products. Int J Pharm 366, pp. 170-184 (2009)

[79]   Kaur IP, Garg A, Singla AK, Aggarwal D. Vesicular systems in ocular drug delivery: An overview. Int J Pharm 269, pp. 1-14 (2004)

[80]   Csaba N, Garcia-Fuentes M, Alonso MJ. Nanoparticles for nasal vaccination. Adv Drug Deliv Rev 61, pp. 140-157 (2009)

[81]   Malyala P, O'Hagan DT, Singh M. Enhancing the therapeutic efficacy of CpG oligonucleotides using biodegradable microparticles. Adv Drug Deliv Rev 61, pp. 218-225 (2009)

[82]   Azzazy HME, Mansour MMH, Kazmierczak SC. Nanodiagnostics: A new frontier for clinical laboratory medicine. Clin Chem 52, pp. 1238-1246 (2006)

[83]   Cormode DP, Skajaa T, Fayad ZA, Mulder WJM. Nanotechnology in medical imaging: Probe design and applications. Arterioscler Thromb Vasc Biol 29, pp. 992-1000 (2009)

[84]   Härtig W, Paulke BR, Brückner G. Fluorescent latex microspheres for retrograde tracing of neurons in mouse basal forebrain combined with immunocytochemistry: A methodical approach. Acta Histochem Suppl 42, pp. 261-265 (1992)

[85]   Goldstein GW, Betz AL. The blood-brain barrier. Sci Am 255, pp. 74-83 (1986)

[86]   Deiana S, Harrington CR, Wischik CM, Riedel G. Methylthioninium chloride reverses cognitive deficits induced by scopolamine: Comparison with rivastigmine. Psychopharmacology (Berl) 202, pp. 53-65 (2009)

[87]   Wischik CM, Edwards PC, Lai RY, Roth M, Harrington CR. Selective inhibition of Alzheimer disease-like tau aggregation by phenothiazines. Proc Natl Acad Sci U S A 93, pp. 11213-11218 (1996)

[88]   Fagerholm U. The highly permeable blood-brain barrier: An evaluation of current opinions about brain uptake capacity. Drug Discov Today 12, pp. 1076-1082 (2007)

[89]   Wolburg H, Liebner S, Lippoldt A. Freeze-fracture studies of cerebral endothelial tight junctions. Methods Mol Med 89, pp. 51-66 (2003)

[90]   Reese TS, Karnovsky MJ. Fine structural localization of a blood-brain barrier to exogenous peroxidase. J Cell Biol 34, pp. 207-217 (1967)

[91]   Oldendorf WH. Measurement of brain uptake of radiolabeled substances using a tritiated water internal standard. Brain Res 24, pp. 372-376 (1970)

[92]   Verkman AS. Aquaporin water channels and endothelial cell function. J Anat 200, pp. 617-627 (2002)

[93]   Hawkins BT, Davis TP. The blood-brain barrier/neurovascular unit in health and disease. Pharmacol Rev 57, pp. 173-185 (2005)

[94]   Löscher W, Potschka H. Role of drug efflux transporters in the brain for drug disposition and treatment of brain diseases. Prog Neurobiol 76, pp. 22-76 (2005)

[95]   Rolfe DF, Brown GC. Cellular energy utilization and molecular origin of standard metabolic rate in mammals. Physiol Rev 77, pp. 731-758 (1997)

[96]   Bradbury MW. The blood-brain barrier. Transport across the cerebral endothelium. Circ Res 57, pp. 213-222 (1985)

[97]   Pahnke J, Wolkenhauer O, Krohn M, Walker LC. Clinico-pathologic function of cerebral ABC transporters - implications for the pathogenesis of Alzheimer's disease. Curr Alzheimer Res 5, pp. 396-405 (2008)

[98]   Lee G, Dallas S, Hong M, Bendayan R. Drug transporters in the central nervous system: Brain barriers and brain parenchyma considerations. Pharmacol Rev 53, pp. 569-596 (2001)

[99]   Ghersi-Egea JF, Minn A, Siest G. A new aspect of the protective functions of the blood-brain barrier: Activities of four drug-metabolizing enzymes in isolated rat brain microvessels. Life Sci 42, pp. 2515-2523 (1988)

[100] Ghersi-Egea JF, Perrin R, Leininger-Muller B, Grassiot MC, Jeandel C, Floquet J, Cuny G, Siest G, Minn A. Subcellular localization of cytochrome P450, and activities of

several enzymes responsible for drug metabolism in the human brain. Biochem Pharmacol 45, pp. 647-658 (1993)

[101] Ghersi-Egea JF, Leninger-Muller B, Suleman G, Siest G, Minn A. Localization of drug-metabolizing enzyme activities to blood-brain interfaces and circumventricular organs. J Neurochem 62, pp. 1089-1096 (1994)

[102] Perrin R, Minn A, Ghersi-Egea JF, Grassiot MC, Siest G. Distribution of cytochrome P450 activities towards alkoxyresorufin derivatives in rat brain regions, subcellular fractions and isolated cerebral microvessels. Biochem Pharmacol 40, pp. 2145-2151 (1990)

[103] Hunt RM. Basal lamina. http://en.wikipedia.org/wiki/File:Basal_lamina.jpg

[104] Sofroniew MV. Reactive astrocytes in neural repair and protection. Neuroscientist 11, pp. 400-407 (2005)

[105] Stevens B. Neuron-astrocyte signaling in the development and plasticity of neural circuits. Neurosignals 16, pp. 278-288 (2008)

[106] Mathiisen TM, Lehre KP, Danbolt NC, Ottersen OP. The perivascular astroglial sheath provides a complete covering of the brain microvessels: An electron microscopic 3D reconstruction. Glia 58, pp. 1094-1103 (2010)

[107] Stewart PA, Wiley MJ. Developing nervous tissue induces formation of blood-brain barrier characteristics in invading endothelial cells: a study using quail-chick transplantation chimeras. Dev Biol 84, pp. 183-192 (1981)

[108] Rucker HK, Wynder HJ, Thomas WE. Cellular mechanisms of CNS pericytes. Brain Res Bull 51, pp. 363-369 (2000)

[109] Pardridge WM. The blood-brain barrier: Bottleneck in brain drug development. NeuroRx 2, pp. 3-14 (2005)

[110] LaVan DA, McGuire T, Langer R. Small-scale systems for in vivo drug delivery. Nat Biotechnol 21, pp. 1184-1191 (2003)

[111] Schroeder U, Sommerfeld P, Ulrich S, Sabel BA. Nanoparticle technology for delivery of drugs across the blood-brain barrier. J Pharm Sci 87, pp. 1305-1307 (1998)

[112] Whittlesey KJ, Shea LD. Delivery systems for small molecule drugs, proteins, and DNA: the neuroscience/biomaterial interface. Exp Neurol 190, pp. 1-16 (2004)

[113] Steiniger SCJ, Kreuter J, Khalansky AS, Skidan IN, Bobruskin AI, Smirnova ZS, Severin SE, Uhl R, Kock M, Geiger KD, Gelperina SE. Chemotherapy of glioblastoma in rats using doxorubicin-loaded nanoparticles. Int J Cancer 109, pp. 759-767 (2004)

[114] Grislain L, Couvreur P, Lenaerts V, Roland M, Deprez-Decampeneere D, Speiser P. Pharmacokinetics and distribution of a biodegradable drug-carrier. Int J Pharm 15, pp. 335-345 (1983)

[115]   Sullivan CO, Birkinshaw C. In vitro degradation of insulin-loaded poly (n-butylcyanoacrylate) nanoparticles. Biomaterials 25, pp. 4375-4382 (2004)

[116]   Härtig W, Paulke BR, Varga C, Seeger J, Harkany T, Kacza J. Electron microscopic analysis of nanoparticles delivering thioflavin-T after intrahippocampal injection in mouse: Implications for targeting beta-amyloid in Alzheimer's disease. Neurosci Lett 338, pp. 174-176 (2003)

[117]   Kreuter J, Shamenkov D, Petrov V, Ramge P, Cychutek K, Koch-Brandt C, Alyautdin R. Apolipoprotein-mediated transport of nanoparticle-bound drugs across the blood-brain barrier. J Drug Target 10, pp. 317-325 (2002)

[118]   Dehouck B, Fenart L, Dehouck MP, Pierce A, Torpier G, Cecchelli R. A new function for the LDL receptor: Transcytosis of LDL across the blood-brain barrier. J Cell Biol 138, pp. 877-889 (1997)

[119]   Sauer I, Dunay IR, Weisgraber K, Bienert M, Dathe M. An apolipoprotein E-derived peptide mediates uptake of sterically stabilized liposomes into brain capillary endothelial cells. Biochemistry 44, pp. 2021-2029 (2005)

[120]   Brown MS, Goldstein JL. Receptor-mediated endocytosis: Insights from the lipoprotein receptor system. Proc Natl Acad Sci U S A 76, pp. 3330-3337 (1979)

[121]   Pitas RE, Boyles JK, Lee SH, Hui D, Weisgraber KH. Lipoproteins and their receptors in the central nervous system. Characterization of the lipoproteins in cerebrospinal fluid and identification of apolipoprotein B,E(LDL) receptors in the brain. J Biol Chem 262, pp. 14352-14360 (1987)

[122]   Pitas RE, Boyles JK, Lee SH, Foss D, Mahley RW. Astrocytes synthesize apolipoprotein E and metabolize apolipoprotein E-containing lipoproteins. Biochim Biophys Acta 917, pp. 148-161 (1987)

[123]   Lockman PR, Koziara JM, Mumper RJ, Allen DD. Nanoparticle surface charges alter blood-brain barrier integrity and permeability. J Drug Target 12, pp. 635-641 (2004)

[124]   Olivier JC, Fenart L, Chauvet R, Pariat C, Cecchelli R, Couet W. Indirect evidence that drug brain targeting using polysorbate 80-coated polybutylcyanoacrylate nanoparticles is related to toxicity. Pharm Res 16, pp. 1836-1842 (1999)

[125]   Selkoe DJ. Alzheimer's disease: Genes, proteins, and therapy. Physiol Rev 81, pp. 741-766 (2001)

[126]   Arriagada PV, Growdon JH, Hedley-Whyte ET, Hyman BT. Neurofibrillary tangles but not senile plaques parallel duration and severity of Alzheimer's disease. Neurology 42, pp. 631-639 (1992)

[127] Cummings BJ, Pike CJ, Shankle R, Cotman CW. Beta-amyloid deposition and other measures of neuropathology predict cognitive status in Alzheimer's disease. Neurobiol Aging 17, pp. 921-933 (1996)

[128] Terry RD, Masliah E, Salmon DP, Butters N, DeTeresa R, Hill R, Hansen LA, Katzman R. Physical basis of cognitive alterations in Alzheimer's disease: Synapse loss is the major correlate of cognitive impairment. Ann Neurol 30, pp. 572-580 (1991)

[129] Gómez-Isla T, Hollister R, West H, Mui S, Growdon JH, Petersen RC, Parisi JE, Hyman BT. Neuronal loss correlates with but exceeds neurofibrillary tangles in Alzheimer's disease. Ann Neurol 41, pp. 17-24 (1997)

[130] Francis PT, Palmer AM, Sims NR, Bowen DM, Davison AN, Esiri MM, Neary D, Snowden JS, Wilcock GK. Neurochemical studies of early-onset Alzheimer's disease. Possible influence on treatment. N Engl J Med 313, pp. 7-11 (1985)

[131] Mesulam MM. Neuroplasticity failure in Alzheimer's disease: Bridging the gap between plaques and tangles. Neuron 24, pp. 521-529 (1999)

[132] Braak H, Braak E. Evolution of the neuropathology of Alzheimer's disease. Acta Neurol Scand Suppl 165, pp. 3-12 (1996)

[133] Avila J, Lucas JJ, Perez M, Hernandez F. Role of tau protein in both physiological and pathological conditions. Physiol Rev 84, pp. 361-384 (2004)

[134] Härtig W, Stieler J, Boerema AS, Wolf J, Schmidt U, Weissfuss J, Bullmann T, Strijkstra AM, Arendt T. Hibernation model of tau phosphorylation in hamsters: Selective vulnerability of cholinergic basal forebrain neurons - implications for Alzheimer's disease. Eur J Neurosci 25, pp. 69-80 (2007)

[135] Nunan J, Small DH. Regulation of APP cleavage by α-, β- and γ-secretases. FEBS Lett 483, pp. 6-10 (2000)

[136] Olichney JM, Hansen LA, Galasko D, Saitoh T, Hofstetter CR, Katzman R, Thal LJ. The apolipoprotein E ε4 allele is associated with increased neuritic plaques and cerebral amyloid angiopathy in Alzheimer's disease and Lewy body variant. Neurology 47, pp. 190-196 (1996)

[137] Holmes C, Boche D, Wilkinson D, Yadegarfar G, Hopkins V, Bayer A, Jones RW, Bullock R, Love S, Neal JW, Zotova E, Nicoll JAR. Long-term eff ects of Aβ42 immunisation in Alzheimer's disease: Follow-up of a randomised, placebo-controlled phase I trial. Lancet 372, pp. 216-223 (2008)

[138] Barten DM, Guss VL, Corsa JA, Loo A, Hansel SB, Zheng M, Munoz B, Srinivasan K, Wang B, Robertson BJ, Polson CT, Wang J, Roberts SB, Hendrick JP, Anderson JJ, Loy JK, Denton R, Verdoorn TA, Smith DW, Felsenstein KM. Dynamics of β-amyloid reductions in

brain, cerebrospinal fluid, and plasma of β-amyloid precursor protein transgenic mice treated with a γ-secretase inhibitor. J Pharmacol Exp Ther 312, pp. 635-643 (2005)

[139] Morgan D, Diamond DM, Gottschall PE, Ugen KE, Dickey C, Hardy J, Duff K, Jantzen P, DiCarlo G, Wilcock D, Connor K, Hatcher J, Hope C, Gorden M, Arendash GW. Aß peptide vaccination prevents memory loss in an animal model of Alzheimer's disease. Nature 408, pp. 982-985 (2000)

[140] Eli Lilly and Company. Lilly Halts Development of Semagacestat for Alzheimer's Disease Based on Preliminary Results of Phase III Clinical Trails. http://newsroom.lilly.com/releasedetail.cfm?releaseid=499794

[141] Khurana R, Coleman C, Ionescu-Zanetti C, Carter SA, Krishna V, Grover RK, Roy R, Singh S. Mechanism of thioflavin T binding to amyloid fibrils. J Struct Biol 151, pp. 229-238 (2005)

[142] Wu C, Wang Z, Lei H, Duan Y, Bowers MT, Shea J. The binding of thioflavin T and its neutral analog BTA-1 to protofibrils of the Alzheimer's disease Aβ(16-22) peptide probed by molecular dynamics simulations. J Mol Biol 384, pp. 718-729 (2008)

[143] Voropai ES, Samtsov MP, Kaplevskii KN, Maskevich AA, Stepuro VI, Povarova OI, Kuznetzova M, Turoverov KK, Fink AL, Uverskii VN. Spectral properties of thioflavin T and its complexes with amyloid fibrils. Journal of Applied Spectroscopy 70, pp. 868-874 (2003)

[144] Bacskai BJ, Hickey GA, Skoch J, Kajdasz ST, Wang Y, Huang G, Mathis CA, Klunk WE, Hyman BT. Four-dimensional multiphoton imaging of brain entry, amyloid binding, and clearance of an amyloid-β ligand in transgenic mice. Proc Natl Acad Sci U S A 100, pp. 12462-12467 (2003)

[145] Dickson DW, Farlo J, Davies P, Crystal H, Fuld P, Yen SH. Alzheimer's disease. A double-labeling immunohistochemical study of senile plaques. Am J Pathol 132, pp. 86-101 (1988)

[146] Klunk WE, Wang Y, Huang GF, Debnath ML, Holt DP, Mathis CA. Uncharged thioflavin-T derivatives bind to amyloid-beta protein with high affinity and readily enter the brain. Life Sci 69, pp. 1471-1484 (2001)

[147] Johnstone EM, Chaney MO, Norris FH, Pascual R, Little SP. Conservation of the sequence of the Alzheimer's disease amyloid peptide in dog, polar bear and five other mammals by cross-species polymerase chain reaction analysis. Brain Res Mol Brain Res 10, pp. 299-305 (1991)

[148] Härtig W, Klein C, Brauer K, Schüppel K, Arendt T, Brückner G, Bigl V. Aged animals with cortical β-amyloid deposits, abnormally phosphorylated protein tau and neurofibrillary tangles. Abstract. Eighth annual meeting of the Hungarian Neuroscience Society, 25.-27.01.2001, Szeged, Hungary, Neurobiology 9, 190-192

[149] Duff K, Rao MV. Progress in the modeling of neurodegenerative diseases in transgenic mice. Curr Opin Neurol 14, pp. 441-447 (2001)

[150] LaFerla FM, Oddo S. Alzheimer's disease: Aβ, tau and synaptic dysfunction. Trends Mol Med 11, pp. 170-176 (2005)

[151] Borchelt DR, Ratovitski T, van Lare J, Lee MK, Gonzales V, Jenkins NA, Copeland NG, Price DL, Sisodia SS. Accelerated amyloid deposition in the brains of transgenic mice coexpressing mutant presenilin 1 and amyloid precursor proteins. Neuron 19, pp. 939-945 (1997)

[152] Jankowsky JL, Slunt HH, Ratovitski T, Jenkins NA, Copeland NG, Borchelt DR. Co-expression of multiple transgenes in mouse CNS: A comparison of strategies. Biomol Eng 17, pp. 157-165 (2001)

[153] Liu L, Tapiola T, Herukka S, Heikkilä M, Tanila H. Aβ levels in serum, CSF and brain, and cognitive deficits in APP + PS1 transgenic mice. Neuroreport 14, pp. 163-166 (2003)

[154] Oberdörster G, Oberdörster E, Oberdörster J. Nanotoxicology: An emerging discipline evolving from studies of ultrafine particles. Environ Health Perspect 113, pp. 823-839 (2005)

[155] Salvi S, Holgate ST. Mechanisms of particulate matter toxicity. Clin Exp Allergy 29, pp. 1187-1194 (1999)

[156] Mills NL, Donaldson K, Hadoke PW, Boon NA, MacNee W, Cassee FR, Sandström T, Blomberg A, Newby DE. Adverse cardiovascular effects of air pollution. Nat Clin Pract Cardiovasc Med 6, pp. 36-44 (2009)

[157] Pereverzeva E, Treschalin I, Bodyagin D, Maksimenko O, Kreuter J, Gelperina S. Intravenous tolerance of a nanoparticle-based formulation of doxorubicin in healthy rats. Toxicol Lett 178, pp. 9-19 (2008)

[158] Lherm C, Müller RH, Puisieux F, Couvreur P. Alkylcyanoacrylate drug carriers II: Cytotoxicity of cyanoacrylate nanoparticles with different alkyl chain length. Int J Pharm 84, pp. 13-22 (1992)

[159] Gulati A, Nath C, Shanker K, Srimal RC, Dhawan KN, Bhargava KP. Effect of alcohols on the permeability of blood-brain barrier. Pharmacol Res Commun 17, pp. 85-93 (1985)

[160] Owens DE3, Peppas NA. Opsonization, biodistribution, and pharmacokinetics of polymeric nanoparticles. Int J Pharm 307, pp. 93-102 (2006)

[161] Roser M, Fischer D, Kissel T. Surface-modified biodegradable albumin nano- and microspheres. II: Effect of surface charges on in vitro phagocytosis and biodistribution in rats. Eur J Pharm Biopharm 46, pp. 255-263 (1998)

[162] Cedervall T, Lynch I, Foy M, Berggård T, Donnelly SC, Cagney G, Linse S, Dawson KA. Detailed identification of plasma proteins adsorbed on copolymer nanoparticles. Angew Chem Int Ed Engl 46, pp. 5754-5756 (2007)

[163]   Klein J. Probing the interactions of proteins and nanoparticles. Proc Natl Acad Sci 104, pp. 2029-2030 (2007)

[164]   Frank MM, Fries LF. The role of complement in inflammation and phagocytosis. Immunol Today 12, pp. 322-326 (1991)

[165]   Ríhová B. Immunomodulating activities of soluble synthetic polymer-bound drugs. Adv Drug Deliv Rev 54, pp. 653-674 (2002)

[166]   Calvo P, Gouritin B, Chacun H, Desmaële D, D'Angelo J, Noel JP, Georgin D, Fattal E, Andreux JP, Couvreur P. Long-circulating PEGylated polycyanoacrylate nanoparticles as new drug carrier for brain delivery. Pharm Res 18, pp. 1157-1166 (2001)

[167]   Dintzis RZ, Okajima M, Middleton MH, Greene G, Dintzis HM. The immunogenicity of soluble haptenated polymers is determined by molecular mass and hapten valence. J Immunol 143, pp. 1239-1244 (1989)

[168]   Blunk T, Hochstrasser DF, Sanchez JC, Müller BW, Müller RH. Colloidal carriers for intravenous drug targeting: Plasma protein adsorption patterns on surface-modified latex particles evaluated by two-dimensional polyacrylamide gel electrophoresis. Electrophoresis 14, pp. 1382-1387 (1993)

[169]   Peracchia MT, Harnisch S, Pinto-Alphandary H, Gulik A, Dedieu JC, Desmaële D, d'Angelo J, Müller RH, Couvreur P. Visualization of in vitro protein-rejecting properties of PEGylated stealth polycyanoacrylate nanoparticles. Biomaterials 20, pp. 1269-1275 (1999)

[170]   Göppert TM, Müller RH. Polysorbate-stabilized solid lipid nanoparticles as colloidal carriers for intravenous targeting of drugs to the brain: Comparison of plasma protein adsorption patterns. J Drug Target 13, pp. 179-187 (2005)

[171]   Labarre D, Vauthier C, Chauvierre C, Petri B, Müller R, Chehimi MM. Interactions of blood proteins with poly(isobutylcyanoacrylate) nanoparticles decorated with a polysaccharidic brush. Biomaterials 26, pp. 5075-5084 (2005)

[172]   Kim HR, Andrieux K, Delomenie C, Chacun H, Appel M, Desmaële D, Taran F, Georgin D, Couvreur P, Taverna M. Analysis of plasma protein adsorption onto PEGylated nanoparticles by complementary methods: 2-DE, CE and Protein Lab-on-chip system. Electrophoresis 28, pp. 2252-2261 (2007)

[173]   Kim HR, Andrieux K, Gil S, Taverna M, Chacun H, Desmaële D, Taran F, Georgin D, Couvreur P. Translocation of poly(ethylene glycol-co-hexadecyl)cyanoacrylate nanoparticles into rat brain endothelial cells: Role of apolipoproteins in receptor-mediated endocytosis. Biomacromolecules 8, pp. 793-799 (2007)

[174]   Gessner A, Waicz R, Lieske A, Paulke B, Mäder K, Müller RH. Nanoparticles with decreasing surface hydrophobicities: Influence on plasma protein adsorption. Int J Pharm 196, pp. 245-249 (2000)

[175]   Lück M, Schröder W, Harnisch S, Thode K, Blunk T, Paulke BR, Kresse M, Müller RH. Identification of plasma proteins facilitated by enrichment on particulate surfaces: Analysis by two-dimensional electrophoresis and N-terminal microsequencing. Electrophoresis 18, pp. 2961-2967 (1997)

[176]   Lemarchand C, Gref R, Passirani C, Garcion E, Petri B, Müller R, Costantini D, Couvreur P. Influence of polysaccharide coating on the interactions of nanoparticles with biological systems. Biomaterials 27, pp. 108-118 (2006)

[177]   Gref R, Lück M, Quellec P, Marchand M, Dellacherie E, Harnisch S, Blunk T, Müller RH. 'Stealth' corona-core nanoparticles surface modified by polyethylene glycol (PEG): influences of the corona (PEG chain length and surface density) and of the core composition on phagocytic uptake and plasma protein adsorption. Colloids and Surfaces B: Biointerfaces 18, pp. 301-313 (2000)

[178]   Allémann E, Gravel P, Leroux JC, Balant L, Gurny R. Kinetics of blood component adsorption on poly(D,L-lactic acid) nanoparticles: evidence of complement C3 component involvement. J Biomed Mater Res 37, pp. 229-234 (1997)

[179]   Diederichs JE. Plasma protein adsorption patterns on liposomes: Establishment of analytical procedure. Electrophoresis 17, pp. 607-611 (1996)

[180]   Göppert TM, Müller RH. Plasma protein adsorption of Tween 80- and poloxamer 188-stabilized solid lipid nanoparticles. J Drug Target 11, pp. 225-231 (2003)

[181]   Göppert TM, Müller RH. Protein adsorption patterns on poloxamer- and poloxamine-stabilized solid lipid nanoparticles (SLN). Eur J Pharm Biopharm 60, pp. 361-372 (2005)

[182]   Dutta D, Sundaram SK, Teeguarden JG, Riley BJ, Fifield LS, Jacobs JM, Addleman SR, Kaysen GA, Moudgil BM, Weber TJ. Adsorbed proteins influence the biological activity and molecular targeting of nanomaterials. Toxicol Sci 100, pp. 303-315 (2007)

[183]   Salvador-Morales C, Flahaut E, Sim E, Sloan J, Green MLH, Sim RB. Complement activation and protein adsorption by carbon nanotubes. Mol Immunol 43, pp. 193-201 (2006)

[184]   Thode K, Lück M, Semmler W, Müller RH, Kresse M. Determination of plasma protein adsorption on magnetic iron oxides: Sample preparation. Pharm Res 14, pp. 905-910 (1997)

[185]   Cruz T, Gaspar R, Donato A, Lopes C. Interaction between polyalkylcyanoacrylate nanoparticles and peritoneal macrophages: MTT metabolism, NBT reduction, and NO production. Pharm Res 14, pp. 73-79 (1997)

[186]   Gref R, Domb A, Quellec P, Blunk T, Müller RH, Verbavatz JM, Langer R. The controlled intravenous delivery of drugs using PEG-coated sterically stabilized nanospheres. Adv Drug Deliv Rev 16, pp. 215-233 (1995)

[187]   Illum L, Davis SS, Müller RH, Mak E, West P. The organ distribution and circulation time of intravenously injected colloidal carriers sterically stabilized with a block copolymer--poloxamine 908. Life Sci 40, pp. 367-374 (1987)

[188]   Peracchia MT, Fattal E, Desmaële D, Besnard M, Noël JP, Gomis JM, Appel M, d'Angelo J, Couvreur P. Stealth PEGylated polycyanoacrylate nanoparticles for intravenous administration and splenic targeting. J Control Release 60, pp. 121-128 (1999)

[189]   Nagayama S, Ogawara K, Minato K, Fukuoka Y, Takakura Y, Hashida M, Higaki K, Kimura T. Fetuin mediates hepatic uptake of negatively charged nanoparticles via scavenger receptor. Int J Pharm 329, pp. 192-198 (2007)

[190]   Barthels M, von Depka M. Gerinnungskompendium. Barthels, von Depka (Eds.). Georg Thieme Verlag, 2003.

[191]   Various authors. Platelets in Thrombotic and Non-Thrombotic Disorders: Pathophysiology, Pharmacology and Therapeutics. Gresele P, Page CP, Fuster V, Vermylen J (Eds.). Cambridge University Press, 2002.

[192]   Hoffman M, Monroe DM3. A cell-based model of hemostasis. Thromb Haemost 85, pp. 958-965 (2001)

[193]   Coleman RW. Contact activation pathway: Inflammatory, fibrinolytic, anticoagulant, antiadhesive, and antiagiogenetic activities. In *Hemostasis and thrombosis*. Colman RW, Hirsh J, Marder VJ, Clowes AW, George JN (Eds.). 2001. pp. 103-121.

[194]   Koziara JM, Oh JJ, Akers WS, Ferraris SP, Mumper RJ. Blood compatibility of cetyl alcohol/polysorbate-based nanoparticles. Pharm Res 22, pp. 1821-1828 (2005)

[195]   Mayer A, Vadon M, Rinner B, Novak A, Wintersteiger R, Fröhlich E. The role of nanoparticle size in hemocompatibility. Toxicology 258, pp. 139-147 (2009)

[196]   Miyamoto M, Sasakawa S, Ozawa T, Kawaguchi H, Ohtsuka Y. Mechanisms of blood coagulation induced by latex particles and the roles of blood cells. Biomaterials 11, pp. 385-388 (1990)

[197]   Sagnella S, Mai-Ngam K. Chitosan based surfactant polymers designed to improve blood compatibility on biomaterials. Colloids Surf B Biointerfaces 42, pp. 147-155 (2005)

[198]   Hemker HC, Wielders S, Kessels H, Béguin S. Continuous registration of thrombin generation in plasma, its use for the determination of the thrombin potential. Thromb Haemost 70, pp. 617-624 (1993)

[199]   Hemker HC, Béguin S. Thrombin generation in plasma: Its assessment via the endogenous thrombin potential. Thromb Haemost 74, pp. 134-138 (1995)

[200]   Hemker HC, Giesen PL, Ramjee M, Wagenvoord R, Béguin S. The thrombogram: Monitoring thrombin generation in platelet-rich plasma. Thromb Haemost 83, pp. 589-591 (2000)

[201] Petros S, Siegemund T, Siegemund A, Engelmann L. The effect of different anticoagulants on thrombin generation. Blood Coagul Fibrinolysis 17, pp. 131-137 (2006)

[202] Siegemund T, Petros S, Siegemund A, Scholz U, Engelmann L. Thrombin generation in severe haemophilia A and B: The endogenous thrombin potential in platelet-rich plasma. Thromb Haemost 90, pp. 781-786 (2003)

[203] Caruthers SD, Cyrus T, Winter PM, Wickline SA, Lanza GM. Anti-angiogenic perfluorocarbon nanoparticles for diagnosis and treatment of atherosclerosis. Wiley Interdiscip Rev Nanomed Nanobiotechnol 1, pp. 311-323 (2009)

[204] Saravanakumar G, Kim K, Park JH, Rhee K, Kwon IC. Current status of nanoparticle-based imaging agents for early diagnosis of cancer and atherosclerosis. J Biomed Nanotechnol 5, pp. 20-35 (2009)

[205] Zhu J, Xue J, Guo Z, Zhang L, Marchant RE. Biomimetic glycoliposomes as nanocarriers for targeting P-selectin on activated platelets. Bioconjug Chem 18, pp. 1366-1369 (2007)

[206] Okamura Y, Handa M, Suzuki H, Ikeda Y, Takeoka S. New strategy of platelet substitutes for enhancing platelet aggregation at high shear rates: Cooperative effects of a mixed system of fibrinogen γ-chain dodecapeptide- or glycoprotein Ibalpha-conjugated latex beads under flow conditions. J Artif Organs 9, pp. 251-258 (2006)

[207] Okamura Y, Fukui Y, Kabata K, Suzuki H, Handa M, Ikeda Y, Takeoka S. Novel platelet substitutes: Disk-shaped biodegradable nanosheets and their enhanced effects on platelet aggregation. Bioconjug Chem 20, pp. 1958-1965 (2009)

[208] Cox AJ, DeWeerd AJ, Linden J. An experiment to measure Mie and Rayleigh total scattering cross sections. Am. J. Phys 70, pp. 620-625 (2002)

[209] Mie G. Beiträge zur Optik trüber Medien, speziell kolloidaler Metallösungen. Ann Phys 330, pp. 377-445 (1908)

[210] Walling MA, Novak JA, Shepard JRE. Quantum dots for live cell and in vivo imaging. Int J Mol Sci 10, pp. 441-491 (2009)

[211] Derfus AM, Chan WCW, Bhatia SN. Probing the cytotoxicity of semiconductor quantum dots. Nanoletters 4, pp. 11-18 (2004)

[212] Yamano T, DeCicco LA, Rikans LE. Attenuation of cadmium-induced liver injury in senescent male fischer 344 rats: role of Kupffer cells and inflammatory cytokines. Toxicol Appl Pharmacol 162, pp. 68-75 (2000)

[213] Rikans LE, Yamano T. Mechanisms of cadmium-mediated acute hepatotoxicity. J Biochem Mol Toxicol 14, pp. 110-117 (2000)

[214] Zhang T, Stilwell JL, Gerion D, Ding L, Elboudwarej O, Cooke PA, Gray JW, Alivisatos AP, Chen FF. Cellular effect of high doses of silica-coated quantum dot profiled with high

throughput gene expression analysis and high content cellomics measurements. Nanoletters 6, pp. 800-808 (2006)

[215] Förster T. Zwischenmolekulare Energiewanderung und Fluoreszenz. Ann Phys 437, pp. 55-75 (1948)

[216] Schmiedel H. Vorlesungsskript Methoden der Biophysik - Lichtstreuung. Fakultät für Physik und Geowissenschaften, Universität Leipzig. 2004.

[217] Jacrot B. The study of biological structures by neutron scattering from solution. Rep. Prog. Phys. 39, pp. 911-953 (1976)

[218] Universal Protein Resource (UniProt). Protein sequence porcine liver carboxylesterase. http://www.uniprot.org/uniprot/Q29550

[219] Lindert S. Licht- und Neutronenkleinwinkelstreuung zur Untersuchung von Nanopartikeln in wässriger Lösung. Fakultät für Physik und Geowissenschaften, Universität Leipzig. 2005.

[220] Lagarias JC, Reeds JA, Wright MH, Wright PE. Convergence properties of the Nelder-Mead simplex method in low dimensions. SIAM J Optim 9, pp. 112-147 (1998)

[221] Nelder JA, Mead R. A simplex method for function minimization. Computer Journal 7, pp. 308-313 (1965)

[222] Härtig W, Brückner G, Holzer M, Brauer K, Bigl V. Digoxigenylated primary antibodies for sensitive dual-peroxidase labelling of neural markers. Histochem Cell Biol 104, pp. 467-472 (1995)

[223] Garcia-Alloza M, Robbins EM, Zhang-Nunes SX, Purcell SM, Betensky RA, Raju S, Prada C, Greenberg SM, Bacskai BJ, Frosch MP. Characterization of amyloid deposition in the APPswe/PS1dE9 mouse model of Alzheimer disease. Neurobiol Dis 24, pp. 516-524 (2006)

[224] Joint Institute for Nuclear Research, Frank Laboratory of Neutron Physics. Neutron diffractometer YuMO. http://flnp.jinr.ru/135/

[225] Joint Institute for Nuclear Research, Frank Laboratory of Neutron Physics. IBR2. http://flnp.jinr.ru/251/

[226] KFKI Atomic Energy Research Institute. Budapest Neutron Center. http://www.kfki.hu/brr/indexen.htm

[227] KFKI Atomic Energy Research Institute. Neutron diffractometer Yellow Submarine. http://www.bnc.hu/modules.php?name=News&file=article&sid=3

[228] Hahn-Meitner-Institut Berlin. Berlin Neutron Scattering Center. http://www.helmholtz-berlin.de/media/media/grossgeraete/nutzerdienst/neutronen/instrumente/inst/bensc_all.pdf

[229] ALV-Laser Vertriebsgesellschaft m.b.H. Kompakt Goniometer System Justage Handbuch. V. 1.0 (1995)

[230] ALV-Laser Vertriebsgesellschaft m.b.H. ALV-Align Utility for WINDOWS Help. V. 3.65 (2000)

[231] Kreuter J, Alyautdin RN, Kharkevich DA, Ivanov AA. Passage of peptides through the blood-brain barrier with colloidal polymer particles (nanoparticles). Brain Res 674, pp. 171-174 (1995)

[232] Schnell SA, Staines WA, Wessendorf MW. Reduction of lipofuscin-like autofluorescence in fluorescently labeled tissue. J Histochem Cytochem 47, pp. 719-730 (1999)

[233] Kacza J, Härtig W, Seeger J. Oxygen-enriched photoconversion of fluorescent dyes by means of a closed conversion chamber. J Neurosci Methods 71, pp. 225-232 (1997)

[234] Apelt J, Schliebs R. β-amyloid-induced glial expression of both pro- and anti-inflammatory cytokines in cerebral cortex of aged transgenic Tg2576 mice with Alzheimer plaque pathology. Brain Res 894, pp. 21-30 (2001)

[235] Härtig W, Kacza J, Paulke B, Grosche J, Bauer U, Hoffmann A, Elsinghorst PW, Gütschow M. In vivo labelling of hippocampal beta-amyloid in triple-transgenic mice with a fluorescent acetylcholinesterase inhibitor released from nanoparticles. Eur J Neurosci 31, pp. 99-109 (2010)

[236] Mueggler T, Meyer-Luehmann M, Rausch M, Staufenbiel M, Jucker M, Rudin M. Restricted diffusion in the brain of transgenic mice with cerebral amyloidosis. Eur J Neurosci 20, pp. 811-817 (2004)

[237] Gessner A, Lieske A, Paulke B, Müller R. Influence of surface charge density on protein adsorption on polymeric nanoparticles: analysis by two-dimensional electrophoresis. Eur J Pharm Biopharm 54, pp. 165-170 (2002)

[238] Pahnke J, Walker LC, Scheffler K, Krohn M. Alzheimer's disease and blood-brain barrier function-Why have anti-beta-amyloid therapies failed to prevent dementia progression?. Neurosci Biobehav Rev 33, pp. 1099-1108 (2009)

[239] Fishman JB, Rubin JB, Handrahan JV, Connor JR, Fine RE. Receptor-mediated transcytosis of transferrin across the blood-brain barrier. J Neurosci Res 18, pp. 299-304 (1987)

[240] Liu H, Hua M, Yang H, Huang C, Chu P, Wu J, Tseng I, Wang J, Yen T, Chen P, Wei K. Magnetic resonance monitoring of focused ultrasound/magnetic nanoparticle targeting delivery of therapeutic agents to the brain. Proc Natl Acad Sci U S A 107, pp. 15205-15210 (2010)

[241] Wunderlich G, Grüning T, Paulke BR, Lieske A, Kotzerke J. 99mTc labelled model drug carriers - Labeling, stability and organ distribution in rats. Nucl Med Biol 31, pp. 87-92 (2004)

[242] Zhuang ZP, Kung MP, Hou C, Skovronsky DM, Gur TL, Plössl K, Trojanowski JQ, Lee VM, Kung HF. Radioiodinated styrylbenzenes and thioflavins as probes for amyloid aggregates. J Med Chem 44, pp. 1905-1914 (2001)

[243] Wolburg H, Wolburg-Buchholz K, Engelhardt B. Diapedesis of mononuclear cells across cerebral venules during experimental autoimmune encephalomyelitis leaves tight junctions intact. Acta Neuropathol 109, pp. 181-190 (2005)

[244] Eichinger S, Hron G, Kollars M, Kyrle PA. Prediction of recurrent venous thromboembolism by endogenous thrombin potential and D-dimer. Clin Chem 54, pp. 2042-2048 (2008)

[245] Hemker HC, Al Dieri R, De Smedt E, Béguin S. Thrombin generation, a function test of the haemostatic-thrombotic system. Thromb Haemost 96, pp. 553-561 (2006)

[246] Pfeifer H, Schmiedel H, Stannarius R. Kompaktkurs Physik. . B.G. Teuber Verlag / GWV Fachverlage GmbH, 2004.

[247] Schätzel K. Single-photon correlation techniques. In *Dynamic Light Scattering - The Method and Some Applications*. Brown W (Ed.). 1993. .

[248] Štěpánek P. Data analysis in dynamic light scattering. In *Dynamic Light Scattering - The Method and Some Applications*. Brown W (Ed.). 1993. pp. 177-241.

7. Appendix

7.1. Abbreviations

Physical and chemical symbols are used without further explanation, amino acid codes in accordance with IUPAC rules. This applies to abbreviations in common use too.

Aβ	β-Amyloid
Aβ$_x$	β-Amyloid with a length of x amino acids
AD	Alzheimer's Disease
ADP	Adenosine diphosphate
ApoE	Apolipoprotein E
APP	Amyloid precursor protein
BBB	Blood-brain barrier
BENSC	Berlin Neutron Scattering Center
BNC	Budapest Neutron Center, Hungary
BRR	Budapest Research Reactor, see BNC
BSA	Bovine serum albumin
BTA-2	4-(6-methyl-1,3-benzothiazol-3-ium-2-yl)-N,N-dimethylaniline
CD41	Platelet glycoprotein IIb of IIb/IIIa complex
CD62P	P-selectin (also GMP-140)
DAB	3,3'- Diaminobenzidine tetrahydrochloride
DLS	Dynamic light scattering
DMSO	Dimethyl sulfoxide
DNA	Deoxyribonucleic acid
EC	Enzyme commission numbers
EPMA	2,3-Epoxypropylmethacrylate
eqn	Equation
FITC	Fluorescein isothiocyanate
FLNP	Frank Laboratory of Neutron Physics, see JINR
FRET	Förster resonance energy transfer
GMP-140	Granule membrane protein 140 (P-selectin, also CD62P)
HBSS	Hank's Buffered Salt Solution

HEMA	Hydroxyethylmethacrylate
HMI	Hahn-Meitner-Institute, Berlin, Germany
IgG	Immunoglobulin G
IgM	Immunoglobulin M
JINR	Joint Institute for Nuclear Research, Dubna, Russia
LDL	Low density lipoprotein
MAA	Methacrylic acid
MMA	Methylmethacrylate
NFT	Neurofibrillary tangles
PACA	Poly(alkyl cyanoacrylate)
PBS	Phosphate-buffered saline
PBCA	Poly(butyl cyanoacrylate)
PE	Phycoerythrin
PEG	Poly(ethylene glycol)
PLE	Porcine liver (carboxyl)esterase (EC 3.1.1.1)
PPP	Platelet-poor plasma
PRP	Platelet-rich plasma
PSD	Position sensitive detector
SANS	Small angle neutron scattering
SLS	Static light scattering
TBS	Tris-buffered saline, Tris(hydroxymethyl)aminomethane-buffered saline
TG	Thrombin generation
TOF	Time-of-flight
ThS	Thioflavin S
ThT	Thioflavin T
TRAP-6	Thrombin receptor activating peptide 6 (SFLLRN)
Tris	Tris(hydroxymethyl)aminomethane

7.2. Physical constants

Avogadro constant	N_A	$6.022 \cdot 10^{23} \, \text{mol}^{-1}$
Boltzmann constant	k_B	$1.38065 \cdot 10^{-23} \, \text{JK}^{-1}$

Coherent scattering length

hydrogen	b_H	$-3.7423 \cdot 10^{-15} \, \text{m}$
deuterium	b_D	$6.674 \cdot 10^{-15} \, \text{m}$
carbon	b_C	$6.6484 \cdot 10^{-15} \, \text{m}$
nitrogen	b_N	$9.36 \cdot 10^{-15} \, \text{m}$
oxygen	b_O	$5.805 \cdot 10^{-15} \, \text{m}$
sulfur	b_S	$2.847 \cdot 10^{-15} \, \text{m}$
Elementary charge	Q_e	$-1.602 \cdot 10^{-19} \, \text{C}$
Neutron mass	m_n	$1.6726 \cdot 10^{-27} \, \text{kg}$
Planck constant	h	$6.6261 \cdot 10^{-34} \, \text{Js}$

7.3. Theoretical background for static light scattering

An averaging over a large time interval collects a large number of scattering processes. Those are distributed symmetrically around $\lambda_s = \lambda_e$, which means, that $\lambda_s = \lambda_e + \lambda_x$ occurs with the same certainty like $\lambda_s = \lambda_e - \lambda_x$ and, therefore, $|\vec{k}_e| = |\vec{k}_s| = k$.

The incident light is an electromagnetic wave $\vec{E}_e$ with a direction of polarization $\vec{n}_e$, amplitude of the electric field strength E_0 and direction of propagation $\vec{k}_e$.

$$\vec{E}_e(\vec{r}, t) = \vec{n}_e E_0 e^{i(\vec{k}_e \vec{r} - \omega t)} \tag{64}$$

In the location $\vec{r}$ the incident field induces a time variable dipole moment $d\vec{\mu}(\vec{r}, t)$ within the volume element dV, which is proportional to $\vec{E}_e$. The proportionality constant is the susceptibility $\chi(\vec{r})$.

$$d\vec{\mu}(\vec{r}, t) = \chi(\vec{r}) dV \vec{E}_e(\vec{r}, t) \tag{65}$$

The time variable dipole moment can be interpreted as HERTZIAN dipole and, therefore, itself emits electromagnetic radiation. The scattered field $\vec{E}_i$ as the far field of the HERTZIAN dipole is proportional to the second derivative with respect to time of the dipole moment at the retarded time t_R [246]. Thus, the in the volume element dV at the location $\vec{r}$ scattered field exhibits at the detector at the location $\vec{R} = R \cdot \hat{k}_s$ and the time t the electric field strength

$$d\vec{E}_s(\vec{R}, \vec{r}, t) = \frac{\left(\left(\frac{d^2 \vec{\mu}(\vec{r}, t)}{dt^2} \right)_{t=t_R} \times \vec{k}_s \right) \times \vec{k}_s}{4 \pi \varepsilon_0 c^2 R} . \tag{66}$$

R is the distance between sample center and detector. The retarded time t_R represents the time t_R when the signal was emitted by the dipole, when the signal arrives at the detector.

$$t_R = t - \frac{R}{c} + \frac{\hat{k}_s \vec{r}}{c} \tag{67}$$

The third term of equation 64 accommodates, that the scattering volume has a finite dimension and, therefore, not all scatterers are within the origin. Every single atom within the sample is a dipole; the scattered field results from the interference of all those far fields. The resulting electric field strength in the direction of polarization $\vec{n}_s$ in the detector is

$$\vec{n}_s \vec{E}_s(\vec{R}, t) = \int_V \frac{\vec{n}_s \circ \left(\left(d\ddot{\vec{\mu}}(\vec{r}, t_R) \right) \times \vec{k}_s \right) \times \vec{k}_s}{4\pi \varepsilon_0 c^2 R} = -\int_V \frac{\vec{n}_s d\ddot{\vec{\mu}}(\vec{r}, t_R)}{4\pi \varepsilon_0 c^2 R}$$

$$= -\int_V \frac{\vec{n}_s \chi(\vec{r}) \ddot{\vec{E}}_e(\vec{r}, t_R)}{4\pi \varepsilon_0 c^2 R} dV = -\int_V \frac{\vec{n}_s \chi(\vec{r}) \vec{n}_e}{4\pi \varepsilon_0 c^2 R} \omega^2 E_0 e^{i(\vec{k}_e \vec{r} - \omega t_R)} dV \tag{68}$$

$$= \frac{\omega^2 E_0}{4\pi \varepsilon_0 c^2 R} \int_V dV \vec{n}_s \chi(\vec{r}) \vec{n}_e e^{i\vec{q}\vec{r}} e^{i(kR - \omega t)}$$

According to equation 13 the differential cross section $\frac{d\sigma}{d\Omega}$ can be introduced. The incident energy density j_0 is determined by the incident electric field.

$$j_0 = \frac{1}{2} \varepsilon_0 E_0^2 c \tag{69}$$

The measured intensity at the detector with the sample-detector distance R results from the scattered wave $\vec{E}_s$ with the direction of polarization $\vec{n}_s$.

$$dP_s = \frac{1}{2} \varepsilon_0 \left| \left(\vec{n}_s \vec{E}_s \right) \right|^2 c R^2 d\Omega \tag{70}$$

Thus, differential cross section equals

$$\frac{d\sigma}{d\Omega}(\vec{q}) = \frac{R^2}{E_0^2} \left| \left(\vec{n}_s \vec{E}_s \right) \right|^2 = \frac{\omega^4}{16\pi^2 \varepsilon_0^2 c^4} \left| \vec{n}_s \int_V dV \chi(\vec{r}) e^{-i\vec{q}\vec{r}} \vec{n}_e \right|^2 \equiv \left\langle \left| F(\vec{q}) \right|^2 \right\rangle, \tag{71}$$

and the scattering amplitude of the sample can be written

$$F(\vec{q}) \equiv \frac{\pi}{\lambda^2 \varepsilon_0} \vec{n}_s \int_V dV \chi(\vec{r}) e^{-i\vec{q}\vec{r}} \vec{n}_e = \frac{\pi}{\lambda^2 \varepsilon_0} \sum_{i=1}^{N_{mol}} \vec{n}_s e^{-i\vec{q}\vec{R}_i} \int_{V_i} dV \chi(\vec{r}) e^{-i\vec{q}\vec{r}} \vec{n}_e . \tag{72}$$

Compared to equation 15 results the scattering amplitude of the molecule.

$$f_i(\vec{q}) \equiv \frac{\pi}{\lambda^2 \varepsilon_0} \vec{n}_s \int_{V_i} dV \chi(\vec{r}) e^{-i\vec{q}\vec{r}} \vec{n}_e \tag{73}$$

Thus, the definition of the scattering length density for light scattering $\rho_{LS}(\vec{r})$ can be derived.

$$\rho_{LS}(\vec{r}) \equiv \frac{\pi}{\lambda^2 \varepsilon_0} \vec{n}_s \chi(\vec{r}) \vec{n}_e \tag{74}$$

If isotropic, spherical molecules are used, the susceptibility $\chi(\vec{r})$ is reduced to a scalar $\chi(r)$. This allows to derive an explicit form factor.

$$\langle |f_i(q)|^2 \rangle = \frac{\pi^2}{\lambda^4 \varepsilon_0^2} \left\langle \int\limits_{V_i} \int\limits_{V_i} dV' dV'' \vec{n}_s \chi(\vec{r}') \vec{n}_e \vec{n}_s \chi(\vec{r}'') \vec{n}_e e^{-i\vec{q}(\vec{r}'-\vec{r}'')} \right\rangle$$

$$= \frac{\pi^2}{\lambda^4 \varepsilon_0^2} (\vec{n}_s \vec{n}_e)^2 \int\limits_{V_i} \int\limits_{V_i} dV' dV'' \chi(r') \chi(r'') \left\langle e^{-i\vec{q}(\vec{r}'-\vec{r}'')} \right\rangle \qquad (75)$$

$$= \frac{\pi^2}{\lambda^4 \varepsilon_0^2} (\vec{n}_s \vec{n}_e)^2 \int\limits_{V_i} \int\limits_{V_i} dV' dV'' \chi(r') \chi(r'') \frac{\sin(q(r'-r''))}{q(r'-r'')}$$

Using the definition for the scattering function of a molecule $P(\vartheta)$

$$P(\vartheta) \equiv \frac{1}{\alpha_i^2} \int\limits_{V_i} \int\limits_{V_i} dV' dV'' \chi(r') \chi(r'') \frac{\sin(q(r'-r''))}{q(r'-r'')}, \qquad (76)$$

The form factor $\langle |f_i(\vec{q})|^2 \rangle$ equals

$$\langle |f_i(q)|^2 \rangle = \frac{\pi^2}{\lambda^4 \varepsilon_0^2} (\vec{n}_s \vec{n}_e)^2 \alpha_i^2 P(\vartheta) \qquad (77)$$

α_i^2 is the scattering-effective polarizability of the molecule i, which is the difference between the polarizability of the molecule and the polarizability of the solvent. The used nanoparticles can not be understood as punctiform dipole; therefore, $P(\vartheta)$ represents the ratio between the angular-dependent scattering intensity of a nanoparticle compared to punctiform scatterer with the same polarizability.

For a polymeric nanoparticle, consisting of repetitive molecules with the same averaged susceptibility $\bar{\chi}_i \equiv \alpha_i / V_i$, $P(\vartheta)$ can be written as

$$P(\vartheta) = \frac{1}{V_i^2} \int\limits_{V_i} \int\limits_{V_i} dV' dV'' \frac{\sin(q(r'-r''))}{q(r'-r'')} \approx \frac{1}{V_i^2} \int\limits_{V_i} \int\limits_{V_i} dV' dV'' \left(1 - \frac{(q(r'-r''))^2}{6} \right)$$

$$\equiv 1 - \frac{q^2 R_G^2}{3} = 1 - \frac{16\pi^2 n_S^2}{3\lambda^2} R_G^2 \sin^2\left(\frac{\vartheta}{2}\right). \qquad (78)$$

Thereby, radius of gyration of the particle was introduced.

$$R_G^2 = \frac{1}{2 V_i^2} \int\limits_{V_i} \int\limits_{V_i} dV' dV'' (q(r'-r''))^2 \qquad (79)$$

This is a special case of equation 26. For homogeneous particles the scattering length density is position-independent and can be isolated from the integral. Now the structure function can be given.

$$\left\langle \sum_{i,j=1}^{N_{mol}} e^{i\vec{q}(\vec{R}_i - \vec{R}_j)} \right\rangle = N_{mol} \left(1 - 2 A_2 M c + O(c^2) \right) \qquad (80)$$

M is the molecular mass and c the mass concentration of the particle, A_2 is called second virial coefficient and represents interaction of nanoparticles with a finite concentration. The differential cross section results in

$$\frac{d\sigma}{d\Omega}(\vartheta)=\frac{\pi^2}{\lambda^4\varepsilon_0^2}(\vec{n}_s\vec{n}_e)^2\alpha_i^2 P(\vartheta)\cdot N_{mol}\left(1-2A_2 M c+O(c^2)\right).$$ (81)

The polarizability difference α is a molecular measure and, therefore, difficult to access. Using the CLAUSIUS-MOSOTTI equation α can be expressed by the macroscopic measure refractive index.

$$n_D^2-n_S^2=\frac{\alpha_i\rho_p}{\varepsilon_0}$$ (82)

n_D is the refractive index of the dilution, whereas n_S is the refractive index of the solvent. ρ_p represents the particle density N_{mol}/V. With $(n_D-n_S)\approx(d n_D/d c)\cdot c$ and $(n_D+n_S)\approx 2 n_S$ the polarizability results in

$$\alpha_i=\frac{2\varepsilon_0 n_S c}{\rho_p}\left(\frac{d n_D}{d c}\right).$$ (83)

Therewith, the differential cross section equals

$$\frac{d\sigma}{d\Omega}(\vartheta)=\frac{\pi^2}{\lambda^4}(\vec{n}_s\vec{n}_e)^2\frac{4 n_S^2 c^2}{\rho_p}\left(\frac{d n_D}{d c}\right)^2 P(\vartheta)\cdot V\left(1-2A_2 M c+O(c^2)\right).$$ (84)

The RAYLEIGH ratio R_ϑ is defined as

$$R_\vartheta\equiv\frac{1}{2(\vec{n}_e\vec{n}_s)^2}\frac{1}{V}\frac{d\sigma}{d\Omega}.$$ (85)

Furthermore, all constants or measures that are determined by the experiment are combined to a constant K.

$$K\equiv\frac{2\pi^2 n_S^2}{N_A\lambda^4}\left(\frac{d n_D}{d c}\right)^2$$ (86)

With $\rho=c N_A/M$ the RAYLEIGH ratio R_ϑ can be written as

$$R_\vartheta=KcMP(\vartheta)\cdot(1-2A_2 Mc).$$ (87)

In an experiment Kc/R_ϑ is measured.

$$\frac{Kc}{R_\vartheta}=\frac{1}{MP(\vartheta)\cdot(1-2A_2 Mc)}\approx\frac{1}{MP(\vartheta)}(1+2A_2 Mc)=\frac{1}{P(\vartheta)}\left(\frac{1}{M}+2A_2 c\right)$$ (88)

This equation is used to interpret data from static light scattering experiment in a GUINIER plot.

7.4. Theoretical background for dynamic light scattering

Due to the motion of the scatterers the DOPPLER effect causes wavelength shifts in the emitted light. This effect is small; therefore, dynamic light scattering is also called quasielastic light scattering with $\vec{k}_e \cong \vec{k}_s$. The fluctuations are interpreted as time-dependent variability of the susceptibility. With respect to all particle motions within the scattering volume equation 68 is written

$$\vec{n}_s \vec{E}_s(t) \propto \sum_{i=1}^{N_{mol}} \vec{n}_s e^{-i\vec{q}\vec{R}_i(t)} \int_{V_i} \mathrm{d}V \chi(\vec{r}(t)) e^{-i\vec{q}\vec{r}(t)} \vec{n}_e . \tag{89}$$

Translations within the sample determine the phase factor $e^{-i\vec{q}\vec{R}_i(t)}$, whereas intramolecular vibrations influence $e^{-i\vec{q}\vec{r}(t)}$. Hence, different phenomena lead to the time-dependent fluctuations of the scattered field and, thereby, intensity fluctuations observed at the detector. On the other hand, the characteristic times for translations, rotations and vibrations are distinguishably different.

To interpret the interference pattern observed at the detector, the correlator calculates a normed intensity autocorrelation function $g_2(\tau)$.

$$g_2(\tau) \equiv \frac{\langle I_s(t) I_s(t+\tau) \rangle_t}{\langle I_s(t) \rangle_t^2} \tag{90}$$

In dynamic light scattering τ is named correlation time. I_s equals the squared magnitude of E_s: $I_s = |E_s|^2$. The average over t is defined as

$$\langle A(t) \rangle_t = \lim_{T \to \infty} \frac{1}{T} \int_0^T A(t)\mathrm{d}t . \tag{91}$$

For non-pathological scattering processes high and low correlation times result in a limiting value.

$$\lim_{\tau \to 0} g_2(\tau) = \frac{\langle I_s(t)^2 \rangle_t}{\langle I_s(t) \rangle_t^2} \qquad \lim_{\tau \to \infty} g_2(\tau) = 1 \tag{92}$$

Furthermore, a normed field autocorrelation function $g_1(\tau)$ is introduced.

$$g_2(\tau) \equiv \frac{\langle E_s(t) E_s(t+\tau) \rangle_t}{\langle |E_s(t)|^2 \rangle_t} = \frac{\langle E_s(t) E_s(t+\tau) \rangle_t}{\langle I_s(t) \rangle_t} \tag{93}$$

The limiting values are

$$\lim_{\tau \to 0} g_1(\tau) = 1 \qquad \lim_{\tau \to \infty} g_1(\tau) = \frac{\langle E_s(t) \rangle_t^2}{\langle |E_s(t)|^2 \rangle_t} \tag{94}$$

Intensity autocorrelation function $g_2(\tau)$ and the field autocorrelation function $g_1(\tau)$ are related by the SIEGERT function[247].

$$g_2(\tau) = 1 + \beta\, g_1^2(\tau) \tag{95}$$

This applies only under GAUSSIAN scattering[248].

$g_1(\tau)$ can be written as superposition of relaxant exponential functions $e^{\frac{-\tau}{\tau_R}}$ with the characteristic relaxation times τ_R.

$$g_1(\tau) = \int\limits_0^\infty A(\tau_R)\, e^{\frac{-\tau}{\tau_R}}\, d\tau_R \tag{96}$$

$g_1(\tau)$ is a LAPLACE transformation of $A(\tau_R)$. Data are given only on a discrete time scale, therefore, it should be written:

$$g_1(\tau_i) = \sum_j A(\tau_j)\, e^{\frac{-\tau_i}{\tau_j}} \tag{97}$$

τ_R is related to the translational diffusion coefficient D.

$$\frac{1}{\tau_R} = Dq^2 \tag{98}$$

In case of spherical particles the STOKES-EINSTEIN relation applies, giving a connection between the translational diffusion coefficient D the hydrodynamic radius R_{hy}.

$$D = \frac{kT}{6\pi\eta R_{hy}} \tag{99}$$

Using the definition for the scattering vector q, it follows that

$$R_{hy} = \frac{8}{3} \frac{k_B T \pi n_s^2}{\eta \lambda^2} \sin^2\left(\frac{1}{2}\Theta\right)\tau \ . \tag{100}$$

Acknowledgments

Wissenschaftlicher Werdegang

Diplom-Biochemiker Thomas Siegemund

01/2009 – 11/2009   Wissenschaftlicher Mitarbeiter

Gerinnungslabor, Labor Dr. Reising-Ackermann und Partner, Leipzig

01/2008 – 12/2008 Wissenschaftlicher Mitarbeiter

Klinische Hämostaseologie und Hämophiliezentrum, Zentrum für Innere
Medizin, Universität Leipzig

04/2007 – 12/2007 Wissenschaftlicher Mitarbeiter

Gerinnungslabor, Labor Dr. Reising-Ackermann und Partner, Leipzig

01/2006 – 01/2007 Wissenschaftlicher Mitarbeiter

Klinische Hämostaseologie und Hämophiliezentrum, Zentrum für Innere
Medizin, Universität Leipzig

01/2004 – 04/2007 Wissenschaftlicher Mitarbeiter

Physik der Weichen Materie, Institut für Experimentelle Physik I,
Fakultät für Physik und Geowissenschaften, Universität Leipzig und
Abteilung für Neurochemie, Paul-Flechsig-Institut für Hirnforschung,
Medizinische Fakultät, Universität Leipzig

05/2003 – 11/2003 Diplomarbeit

Abnorme Phosphorylierung des Tau-Proteins bei experimentell induzierten
Alterungsprozessen in kleinen Primaten (Mausmaki, Microcebus murinus)
Abteilung für Neurochemie, Paul-Flechsig-Institut für Hirnforschung,
Medizinische Fakultät, Universität Leipzig

11/2001 – 09/2003 Studentische Hilfskraft

Speziallabor Gerinnungsdiagnostik, Institut für Klinische Chemie und
Pathobiochemie, Universitätsklinikum Leipzig

10/1998 – 05/2003 Diplomstudiengang Biochemie

Institut für Biochemie, Fakultät für Biowissenschaften, Pharmazie und
Psychologie, Universität Leipzig

1996 Abitur

Wilhelm-Ostwald-Gymnasium, Leipzig

Bibliographische Beschreibung

Siegemund, Thomas

Structure and properties of drug-loaded polymeric nanoparticles targeting β-amyloid

Universität Leipzig, Dissertation

139 Seiten, 248 Literaturangaben, 64 Abbildungen, 11 Tabellen

Referat:

Polymere Nanopartikel sind ein vielversprechender Ansatz für die Diagnose und Therapie von Krankheiten. Sie ermöglichen den Einsatz von schwerlöslichen oder instabilen Wirkstoffen. Ein weiterer Vorteil ist die Möglichkeit das Targetings, durch gezielte Modifikationen des Nanopartikels wird der Wirkstoff zum Zielort transportiert und kann dort in der gewünschten Form freigesetzt werden; dadurch könnten bei erhöhter Wirksamkeit die Nebenwirkungen von Medikamenten reduziert werden.

Ziel dieser Arbeit war die Untersuchung von physikalischen und biochemischen Eigenschaften von Nanopartikeln bestehend aus einem abbaustabilen Polystyren-Kern und einer biologisch abbaubaren Schale aus Polybutylcyanoacrylat. Es werden Methoden beschrieben, um die Größe, Struktur und den Abbau dieser Wirkstoffträger zu untersuchen. Die untersuchten Nanopartikel zeigen RAYLEIGH-Streuung, sowohl Größe als auch Abbau können durch Messung des Absorptionsspektrums bestimmt werden. Weiterhin konnten diese Eigenschaften mit Hilfe von dynamischer und statischer Lichtstreuung sowie Neutronenkleinwinkelstreuung untersucht werden. Bei letzterer Methode konnte gezeigt werden, dass die Schale größtenteils abgebaut werden kann, während der Kern intakt bleibt.

In einem weiteren Teil der Arbeit wurde die Überwindung der Blut-Hirn-Schranke durch polymere Nanopartikel untersucht. Dabei wurde der fluoreszierende Thioflavine als Modellwirkstoffe eingesetzt. Das Durchdringen der Blut-Hirn-Schranke konnte nur mit Nanopartikeln erreicht werden, an deren Oberfläche ein Apolipo-protein E-Peptid gekoppelt war. Es konnte gezeigt werden, das die Nanopartikel-schale im Gehirn abgebaut wird, der Wirkstoff freigesetzt wird und an Amyloid β, einem Marker der Alzheimer-Krankheit, bindet.